



OTTO VON GUERICKE
UNIVERSITÄT
MAGDEBURG

EIT

FAKULTÄT FÜR
ELEKTROTECHNIK UND
INFORMATIONSTECHNIK

Fusion of Interventional Ultrasound & X-ray

Dissertation

zur Erlangung des akademischen Grades

Doktoringenieur
(Dr.-Ing.)

von Dipl.-Inf. Markus Kaiser

geb. am 12.12.1984 in Gera

genehmigt durch die Fakultät für Elektrotechnik und Informationstechnik
der Otto-von-Guericke-Universität Magdeburg

Gutachter: Prof. Dr. rer. nat. Georg Rose
(Otto-von-Guericke-Universität Magdeburg)
Prof. Dr.-Ing. habil. Andreas Maier
(Friedrich-Alexander-Universität Erlangen-Nürnberg)

Promotionskolloquium am 29.09.2016

Res Electricae Magdeburgenses

Magdeburger Forum zur Elektrotechnik, Jg. 2016, Band 71, 2016

<http://www.mafo.ovgu.de/>

IMPRESSUM

Herausgeber:

- Prof. Dr.-Ing. Andreas Lindemann, Lehrstuhl für Leistungselektronik, Institut für Elektrische Energiesysteme
- Prof. Dr.-Ing. habil. Martin Wolter, Lehrstuhl für Elektrische Netze und Erneuerbare Energie, Institut für Elektrische Energiesysteme
- Prof. Dr. rer. nat. Georg Rose, Lehrstuhl für Medizinische Telematik/Medizintechnik, Institut für Medizintechnik
- Prof. Dr.-Ing. Ralf Vick, Lehrstuhl für Elektromagnetische Verträglichkeit, Institut für Medizintechnik

Gründungsherausgeber:

- Prof. Dr. rer. nat. habil. Jürgen Nitsch
- Prof. Dr.-Ing. habil. Zbigniew Antoni Styczynski

alle: Otto-von-Guericke-Universität Magdeburg
Postfach 4120, 39016 Magdeburg

V. i. S. d. P.:

Markus Kaiser

Otto-von-Guericke-Universität Magdeburg, Postfach 4120, 39016 Magdeburg

1. Auflage, Magdeburg, Otto-von-Guericke-Universität, 2016

Zugl.: Magdeburg, Univ., Diss., 2016

Auflage: 100

Redaktionsschluss: November 2016

ISSN: 1612-2526

ISBN: 978-3-944722-51-1

© Copyright 2016 Markus Kaiser

Bezug über die Herausgeber

Druck: docupoint GmbH

Otto-von-Guericke-Allee 14, 39179 Barleben

Abstract

Today, in an elderly community, the treatment of structural heart disease will become more and more important. Constant improvements of medical imaging technologies and the introduction of new catheter devices caused the trend to replace conventional open heart surgery by minimal invasive interventions.

These advanced interventions need to be guided by different medical imaging modalities. The two main imaging systems here are X-ray fluoroscopy and Transesophageal Echocardiography (TEE). While X-ray provides a good visualization of inserted catheters, which is essential for catheter navigation, TEE can display soft tissues, especially anatomical structures like heart valves. Both modalities provide real-time imaging and are necessary to lead minimal invasive heart surgery to success.

Usually, the two systems are detached and not connected. It is conceivable that a fusion of both worlds can create a strong benefit for the physicians. It can lead to a better communication within the clinical team and can probably enable new surgical workflows.

Because of the completely different characteristics of the image data, a direct fusion seems to be impossible. Therefore, an indirect registration of Ultrasound and X-ray images is used. The TEE probe is usually visible in the X-ray image during the described minimal-invasive interventions. Thereby, it becomes possible to register the TEE probe in the fluoroscopic images and to establish its 3D position. The relationship of the Ultrasound image to the Ultrasound probe is known by calibration.

To register the TEE probe on 2D X-ray images, a 2D-3D registration approach is chosen in this thesis. Several contributions are presented, which are improving the common 2D-3D registration algorithm for the task of Ultrasound and X-ray fusion, but also for general 2D-3D registration problems.

One presented approach is the introduction of planar parameters that increase robustness and speed during the registration of an object on two non-orthogonal views. Another approach is to replace the conventional generation of digital reconstructed radiographs, which is an integral part of 2D-3D registration but also a performance bottleneck, with fast triangular mesh rendering. This will result in a significant performance speed-up. It is also shown that a combination of fast learning-based detection algorithms with 2D-3D registration will increase the accuracy and the capture range, instead of employing them solely to the registration/detection of a TEE probe.

Finally, a first clinical prototype is presented which employs the presented approaches and first clinical results are shown.

Kurzfassung

In einer immer älter werdenden Bevölkerung wird die Behandlung von strukturellen Herzkrankheiten zunehmend wichtiger. Verbesserte medizinische Bildgebung und die Einführung neuer Kathetertechnologien führten dazu, dass immer mehr herkömmliche chirurgische Eingriffe am offenen Herzen durch minimal invasive Methoden abgelöst werden.

Diese modernen Interventionen müssen durch verschiedenste Bildgebungsverfahren navigiert werden. Hierzu werden hauptsächlich Röntgenfluoroskopie und transösophageale Echokardiografie (TEE) eingesetzt. Röntgen bietet eine gute Visualisierung der eingeführten Katheter, was essentiell für eine gute Navigation ist. TEE hingegen bietet die Möglichkeit der Weichteilgewebedarstellung und kann damit vor allem zur Darstellung von anatomischen Strukturen, wie z.B. Herzklappen, genutzt werden. Beide Modalitäten erzeugen Bilder in Echtzeit und werden für die erfolgreiche Durchführung minimal invasiver Herzchirurgie zwingend benötigt.

Üblicherweise sind beide Systeme eigenständig und nicht miteinander verbunden. Es ist anzunehmen, dass eine Bildfusion beider Welten einen großen Vorteil für die behandelnden Operateure erzeugen kann, vor allem eine verbesserte Kommunikation im Behandlungsteam. Ebenso können sich aus der Anwendung heraus neue chirurgische Workflows ergeben.

Eine direkte Fusion beider Systeme scheint nicht möglich, da die Bilddaten eine zu unterschiedliche Charakteristik aufweisen. Daher kommt in dieser Arbeit eine indirekte Registriermethode zum Einsatz. Die TEE-Sonde ist während der Intervention ständig im Fluoroskopiebild sichtbar. Dadurch wird es möglich, die Sonde im Röntgenbild zu registrieren und daraus die 3D Position abzuleiten. Der Zusammenhang zwischen Ultraschallbild und Ultraschallsonde wird durch eine Kalibrierung bestimmt.

In dieser Arbeit wurde die Methode der 2D-3D Registrierung gewählt, um die TEE Sonde auf 2D Röntgenbildern zu erkennen. Es werden verschiedene Beiträge präsentiert, welche einen herkömmlichen 2D-3D Registrieralgorithmus verbessern. Nicht nur im Bereich der Ultraschall-Röntgen-Fusion, sondern auch im Hinblick auf allgemeine Registrierprobleme.

Eine eingeführte Methode ist die der planaren Parameter. Diese verbessert die Robustheit und die Registriergeschwindigkeit, vor allem während der Registrierung eines Objekts aus zwei nicht-orthogonalen Richtungen. Ein weiterer Ansatz ist der Austausch der herkömmlichen Erzeugung von sogenannten digital reconstructed radiographs. Diese sind zwar ein integraler Bestandteil einer 2D-3D Registrierung aber gleichzeitig sehr zeitaufwendig zu berechnen. Es führt zu einem erheblichen Geschwindigkeitsgewinn die herkömmliche Methode durch schnelles Rendering von Dreiecksnetzen zu ersetzen. Ebenso wird gezeigt, dass eine Kombination von schnellen lernbasierten Detektionsalgorithmen und 2D-3D Registrierung die Genauigkeit und die Registrierreichweite verbessert.

Zum Abschluss werden die ersten Ergebnisse eines klinischen Prototypen präsentiert, welcher die zuvor genannten Methoden verwendet.

Acknowledgements

The moment became a longer moment, and suddenly it was a very long moment, so long one could hardly tell where all the time was coming from. - Douglas Adams

Medical image processing is an exciting field of research and I am very glad that I had the chance to work and to contribute in it. Many people supported me during the last years and I want to express my gratitude to all of them.

First of all, Dr. Matthias John from Siemens Healthcare GmbH, who has been my mentor during the whole time and was always my first contact person for everything. Thank you that your ideas never ran out and your patience in discussing, explaining and proof-reading.

I want to thank Prof. Georg Rose from the Otto-von-Guericke University Magdeburg for giving me the opportunity to become a PhD student at his lab and supporting me through the whole PhD process.

Dr. Tobias Heimann for his extensive support and sharing his great experiences, especially during writing and submitting of all the publications.

Prof. Thomas Neumuth from the ICCAS in Leipzig, who has been my first academic advisor and for the chance to become a member of his institute.

Prof. Andreas Maier from the University Erlangen-Nürnberg for reviewing this thesis and our discussion during all the conferences.

The physicians from the Heart Center Leipzig, especially Dr. Philipp Kiefer for affording me the clinical experiences and to have always an open ear during our experiments.

Peter Mountney, PhD, who was my advisor during my stay at Siemens Corporate Research in Princeton, USA. He stands for all the members of the lab who made this a great visit. From a scientific and from a personal point of view.

I also want to thank all the students and employees who have been with Siemens Healthcare AX IN department for all the fruitful discussions. Especially Chris Schwemmer, who made this brilliant thesis template and for all the C++ advises, and Dr. Kerstin Mueller who has just always been there.

Last but not least, I want to thank my wife and my kids for all the patience and understanding and for all the support they gave me in their own way.

Contents

Chapter 1 Introduction	1
1.1 Motivation	1
1.2 Structure of the Thesis	2
Chapter 2 Medical Background	5
2.1 X-ray Angiography	5
2.2 Transesophageal Echocardiography	7
2.3 Minimal Invasive Interventions in Structural Heart Disease	10
2.3.1 Aortic Valve Implantation	10
2.3.2 Mitral Valve Repair	10
2.3.3 Mitral Valve Replacement	11
2.3.4 Atrial Septal Defect / Patent Foramen Ovale Closure	12
2.3.5 Left Atrial Appendage Closure	13
2.3.6 Paravalvular Leak Closure	13
2.4 Fusion of Ultrasound and X-ray	13
Chapter 3 State of the Art in Fusion of Ultrasound & X-ray	17
3.1 2D-3D Registration	18
3.2 Detection	22
3.3 EM Tracking	22
3.4 X-ray Fusion with other Ultrasound Devices	23
3.4.1 Trans-thoracic Echo	23
3.4.2 Intra-cardiac Echo	23
3.4.3 Intravascular Ultrasound	24
Chapter 4 2D-3D Registration Framework	27
4.1 C-arm Projection Geometry	28
4.2 3D TEE Probe Model	31
4.3 DRR Generator	32
4.4 Similarity Measure	35
4.4.1 Types of Similarity Measures	35
4.4.2 Employed Similarity Measures	37
4.4.3 Image Mask	38
4.5 Optimization Methods	38
4.5.1 Powell-Brent	40
4.5.2 Subplex	41

4.6	Optimization Strategy	41
4.7	Quality and Performance Criteria	43
4.7.1	Target Registration Error	43
4.7.2	Projection Distance	44
4.7.3	Reprojection Distance	45
4.7.4	Error Markers	45
4.8	Ground Truth Generation.	46
Chapter 5 2D-3D Registration with Planar Parameters		49
5.1	Motivation.	49
5.2	Methods	53
5.2.1	Planar Parameters for Monoplane Projection	54
5.2.2	Planar Parameters for Biplane Registration.	56
5.3	Objection Motion and Calibration Errors	58
5.4	Experiments & Results	58
5.4.1	Evaluation of Automatic Registration.	58
5.4.2	Evaluation of Manuel Registrations	62
5.5	Discussion & Conclusion	63
Chapter 6 Mesh-based Registration		65
6.1	Motivation.	65
6.2	Methods	66
6.2.1	3D Mesh Model Generation	67
6.2.2	Mesh-based DRR Rendering	68
6.2.3	Rendering and Similarity Measure Pipeline	70
6.3	Experiments & Results	70
6.4	Conclusion.	75
Chapter 7 Detection-Registration-Pipeline for Probe Pose Estimation		77
7.1	Motivation.	77
7.2	Description of Complete Pipeline	78
7.3	Experiments & Results	78
7.3.1	Capture Range Estimation	78
7.3.2	Marker Target Registration Error.	80
7.4	Discussion & Conclusion	88
7.4.1	Discussion of Capture Range Estimation	88
7.4.2	Discussion of Marker Target Registration Error	89
Chapter 8 Prototype for Fusion of Interventional Ultrasound and X-ray		91
8.1	Features of the Clinical Prototype.	92
8.2	Workflow.	93
8.3	Clinical Setup.	95
8.4	Clinical Application.	95
8.5	Conclusion.	97

Chapter 9 Summary and Outlook	99
9.1 Summary	99
9.2 Outlook	101
List of Symbols	103
List of Figures	109
List of Tables	113
List of Algorithms	115
Bibliography	117

Introduction

1.1 Motivation.	1
1.2 Structure of the Thesis	2

1.1 Motivation

Since the last 50 years, different important medical imaging devices were introduced that fundamentally changed the possibilities of medical examinations and interventions. Examples are Computer Tomography (CT), Magnetic Resonance Imaging (MRI) or Ultrasound. Nowadays, the fusion of different medical imaging modalities becomes more and more important to combine the advantages of the different modalities and to expand the field of view for physicians. Not only for pre-operative diagnostics, but also to provide important additional information during interventions.

Another big impact in the medical world during the last 15 years was made in the area of minimal invasive surgery. The combination of new medical instruments and imaging devices allows the physicians to avoid conventional open surgery, especially in the field of heart diseases. More and more catheter-based interventions with newly developed devices are carried out and are slowly replacing open heart surgery. Currently, surgical guidelines [Nish 14] still favoring conventional interventions, but the trends are apparent.

The topic of this thesis is the fusion of the two most important imaging modalities that are used during catheter-based minimal invasive heart surgery: Transesophageal Echocardiography (TEE) and X-ray fluoroscopy. Both systems provide two completely different kind of images with completely different patient information. The information from these two systems are necessary for interventionalists to successfully treat a patient. TEE and X-ray are usually independent systems with no connection. Therefore, the operators have to excerpt the needed information from two detached imaging systems. The fusion of the two systems, which will be introduced in this thesis, aims to support the interventionalists for better navigation and image understanding.

The chosen method to achieve an indirect registration of Ultrasound to X-ray is 2D-3D registration, which is a well known technique in the field of medical image processing. Therefore, the approaches and contributions presented in this thesis are

not for the solely use for the fusion of Ultrasound and X-ray, but can also be used for other applications of image-based 2D-3D registration.

1.2 Structure of the Thesis

This section provides an overview over all chapters in the thesis and will give a short outline.

Chapter 2 - Medical Background

This chapter introduces the medical field in which a fusion of Ultrasound and X-ray can be useful for physicians. Several structural heart diseases are mentioned and it is briefly discussed how they can be treated in a minimal invasive way. The technical imaging equipment, namely Transesophageal Echocardiography and X-ray fluoroscopy, is introduced and described in detail. The pros and cons of both system are discussed as well and it is pointed out how they can be fused and how the medical staff could benefit of such a fusion.

Chapter 3 - State of the Art in Fusion of Ultrasound & X-ray

The state of the art is presented here in a literature overview. Firstly, the general approach for establishing a fusion between TEE and X-ray images is described, like it is mentioned in different publications. Different published approaches from different research groups are mentioned and explained. Additional information is provided on other technologies for fusion of X-ray images with different Ultrasound devices.

Chapter 4 - 2D-3D Registration Framework

The algorithmic pipeline, which is used in the whole thesis, is described in this chapter. All single parts of the method of 2D-3D registration are explained in detail and it is shown how they are used and implemented for the work presented in this thesis. The mathematical background is presented, as well as the evaluation method for the experiments that are carried out in this thesis. Additionally, it is shown how the ground-truth data can be established and recognizable pitfalls are mentioned.

Chapter 5 - 2D-3D Registration with Planar Parameters

The technique of planar parameters is introduced. This method improves the registration of out-of-plane parameters during a 2D-3D registration process from two non-orthogonal angulations. The main contribution here is a novel registration approach which handles translation and rotation of a volume in a double-oblique setting. New transformation parameters are chosen in a way that inplane parameters are kept invariant and independent of the angle offset between both projections. It was successfully tested for manual and automatic registration on clinical data for fusion of transesophageal ultrasound and X-ray.

Chapter 6 - Mesh-based Registration

One drawback of 2D-3D registration is the registration speed which usually lacks real-time performance. One contribution to speed-up such a system is shown in this chapter. The bottleneck of common volume ray-casting generation of digital reconstructed radiographs (DRR) is eliminated with fast rendering of triangular meshes. This becomes possible, because the 3D geometry of the ultrasound probe is known in advance in the setting for TEE and X-ray fusion. The probe's main components can be described by triangular meshes. The results show a significant speed-up of the process while the registration accuracy is not degraded.

Chapter 7 - Detection-Registration-Pipeline for Probe Pose Estimation

This chapter describes a pipeline that combines 2D-3D registration and detection algorithms for the task of TEE probe pose estimation. The advantage of detection algorithms is that they are faster and have a greater capture range compared to 2D-3D registration. Therefore, they are employed to estimate a first estimation of the probe's position which is then used as an initialization for the registration algorithm. The advantage of the 2D-3D registration method is the higher accuracy. The combination of both approaches will produce more accurate and more stable results with better runtime performance.

Chapter 8 - Prototype for Fusion of Interventional Ultrasound and X-ray

Finally, the developed prototype for the fusion application is outlined. Multiple features are described that support physicians and sonographers in their work. The prototype's set up in a clinical environment is described and the first clinical experiences with an interventional team are presented.

Medical Background

2.1 X-ray Angiography	5
2.2 Transesophageal Echocardiography	7
2.3 Minimal Invasive Interventions in Structural Heart Disease.	10
2.4 Fusion of Ultrasound and X-ray	13

Today, in an aging population, cardiovascular diseases (CVD) are one of the biggest burden. Studies show that CVD affect up to 85% of people over 80 years in the USA [Go 13] which is comparable to other developed countries [Kell 10]. 30% of global deaths are related to cardiovascular diseases, which makes it the leading cause of death. One type of CVD are structural heart diseases (SHD). SHD are cardiac diseases that are non-coronary, for example valvular heart disease [Flec 15], paravalvular leaks or patent foramen ovale [Stei 10]. In the future, SHD will become more and more important in daily clinical work. At least 4.2 - 5.6 million adults are affected by valvular heart disease only in the USA [Nkom 06].

Modern minimal invasive therapy methods have been developed in the past 15 years, aiming to support interventions for structural heart disease. Driven by the development of new catheter techniques, a new field of catheter-based medical intervention was established. The two most important imaging modalities for treating structural heart disease are X-ray angiography and Ultrasound. Both modalities have different advantages and disadvantages. X-ray fluoroscopy is used to clearly display catheters inside a patient, which is a precondition for catheter navigation. Ultrasound is particularly used to evaluate the patients anatomy and physiology in real time. The properties of the two modalities are complementing each other. Therefore, minimal invasive heart surgery could benefit of the fusion of Ultrasound and X-ray. A short introduction to those modalities is given in the following chapter as well as to some examples of minimal invasive procedures. An overview about different properties of both modalities is given in Section 2.1.

Some parts of this Chapter have already been published in [Kais 11] and [Kais 13a].

2.1 X-ray Angiography

Catheter-based interventions based on X-ray fluoroscopy and angiography have become a common method in cardiology for years. Over the last decade, major improvements were made to use X-ray for cardiac surgery as well. Upcoming new catheter

	Fluoroscopy (2D X-ray) from today's C-arms	Ultrasound (TEE) from today's TEE probes
Real-time	✓	✓
Image characteristic	Projective	Sectional view, 3D
Soft tissue contrast	Minor	Excellent
Physiological evaluation	Limited, only with contrast agent	Possible, e.g. with Doppler, soft tissue visible
Artifacts	Removed by automatic post-processing	Multiple (see Section 2.2), user knowledge is necessary
Field-of-view	projection area of up to 40 cm × 40 cm	up to 90°×90° with 16 cm depth from the transducer
Health risk	Ionizing radiation, contrast agent can be harmful	Esophageal perforation
Sedation needed	-	✓

Table 2.1: Comparison of different properties of the two imaging modalities.

technologies enabled physicians to carry out minimal invasive interventions and led to the introduction of Hybrid-ORs: operation rooms which are equipped with a fluoroscopic X-ray machine, called C-arm, which can be also used for open heart surgery if necessary.

C-arms are usually equipped with an X-ray tube and a detector which are assembled on a C-shaped arm that can be rotated along two rotational axis around the patient. This allows the physician to view the patient and the inserted devices from different directions. Various angulations are necessary for different interventions, depending on the examined organ or used instrument. Figure 2.1¹ shows an Artis Zeego (Siemens Healthcare GmbH, Forchheim, Germany) as an example of a modern C-arm system.

Today's C-arm systems are available in different configurations. Monoplane C-arm systems consist of one X-ray tube and one X-ray detector. Biplane C-arm systems are equipped with two C-arms and two X-ray tubes and detectors. Mono-plane systems are commonly used in heart surgery settings and during angiographic procedures in the heart. Biplane systems are required during minimal invasive neurological interventions [Raja08] but also for catheter ablations procedures, in particular for pediatric cardiology and electrophysiology [Bros10].

The rotation of a C-arm system is defined by two angles, one for left-anterior-oblique (LAO) and right-anterior-oblique (RAO), which means the left and right side of the patient, given as α , and the second one for cranial-caudal (CRAN/CAUD),

¹Image courtesy of Siemens Healthcare GmbH, Forchheim, Germany.



Figure 2.1: C-arm of type Artis zeego (Siemens Healthcare GmbH, Germany).

which means the head and feet direction of the patient, given as γ . If only one angle is changed between two images, this refers to a mono-oblique, otherwise to a double-oblique setting. See Figure 2.2² for a visualization of the C-arm angles.

2.2 Transesophageal Echocardiography

Ultrasound is used in medical imaging since the 1950's. Since then, a multiplicity of different applications and devices have been developed. For interventions and diagnosis of structural heart diseases, the transesophageal echocardiogram (TEE) is the most important imaging device [Dani 95]. A TEE system consists of a small endoscope with a built-in ultrasound transducer at its tip which is connected to a special Ultrasound machine (Figure 2.3³). During a TEE examination, a probe is inserted into the esophagus and usually images the heart from the posterior to anterior direction. This is visualized in Figure 2.4. Usually, the patient is under general anesthesia for more complex interventions like minimal invasive heart surgery [Seck 99]. The TEE probe is a hand-held probe which is freely steerable by a physician with external controls as well as with the probe itself.

The main advantage of the use of Ultrasound and especially of TEE, is the excellent soft tissue contrast. Anatomical structures like valves, heart walls and even smaller details, like papillary muscles with connecting chordae, are visible. Because of the near distance to the heart, the image quality of TEE is usually superior to other Ultrasound modalities, like Transthoracic Echocardiography (TTE). This results in a

²Image courtesy of Siemens Healthcare GmbH, Forchheim, Germany.

³Image courtesy of Siemens Healthcare Ultrasound, Mountain View, CA, USA.

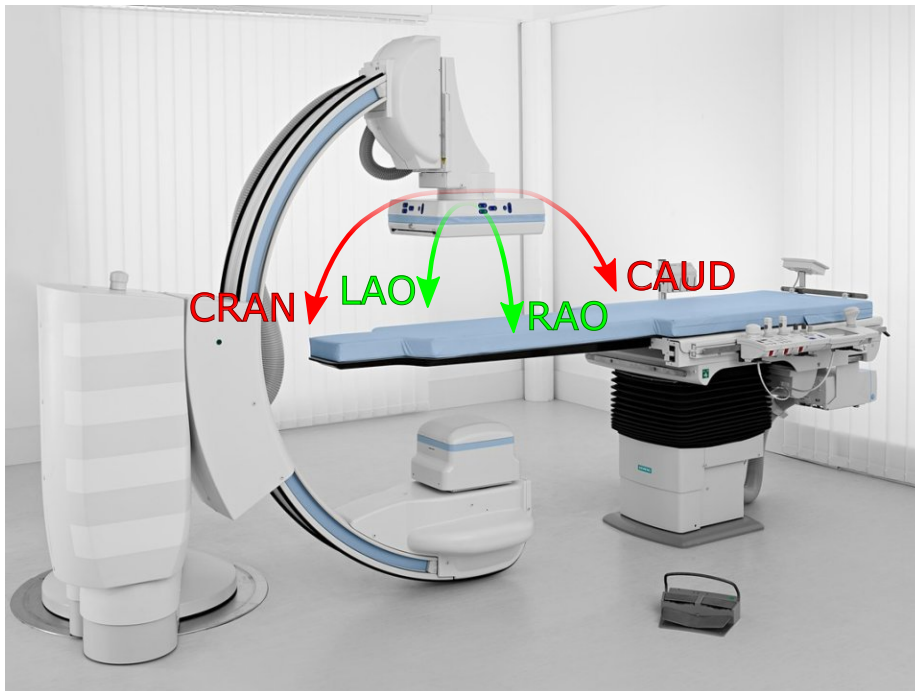


Figure 2.2: Angles of a C-arm system with anatomical terms.



Figure 2.3: A TEE probe like it is used in a clinical environment (Siemens Healthcare Ultrasound, Mountain View, CA, USA).

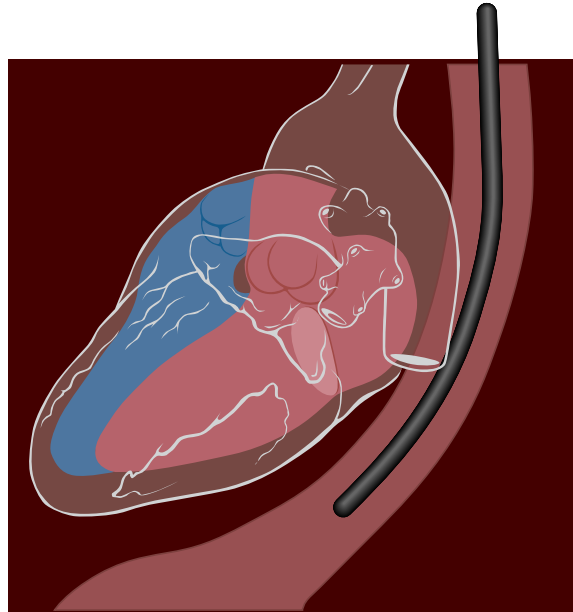


Figure 2.4: Schematic visualization of the performance of a transesophageal echocardiography [Lync 06].

better view of different structures like the aortic valve, the atrial septum or the atrial appendage. Additionally, artifacts from ribs, lung or fat, which are common in TTE, are avoided in TEE. TTE has the ability to show a four chamber view, where all heart chambers are shown in one Ultrasound image. However, it is usually easier to achieve certain views for anatomical and physiological examinations with TEE than with TTE.

Additional tools for further investigation are available, for example Doppler sonography, which can visualize the direction and speed of the blood flow. Modern TEE probes have the ability to display a live 3D Ultrasound image of the viewed tissue which is heavily used to visualize complex structures or to plan procedures.

In contrast to X-ray images, Ultrasound images need a more experienced user to interpret the displayed information. Ultrasound has the tendency to produce image artifacts like acoustic shadowing, mirror images, beam width or speckle artifacts. This can influence the images in the kind of missing structures or degraded images which can lead to falsely perceived objects [Otto04]. Another drawback is that any gas between the viewed object and Ultrasound transducer will totally disturb the images. These artifacts are one reason why Ultrasound is called highly operator-dependent. Artificial structures like catheters, especially if they contain some metal, can cause huge artifacts. Together with the limited field of view, this makes minimal invasive surgery almost impossible with the exclusive use of TEE.

Commonly, it is not easy to find and to identify the single heart structures. Sonographers need a lot of experience and need to learn the specific workflows for finding the single anatomical landmarks [Dani 95].

2.3 Minimal Invasive Interventions in Structural Heart Disease

Many conventional interventions were adapted to minimal invasive surgery in the field of structural heart disease during the last years. The drivers for this trend from open-heart surgery to trans-catheter procedures are the availability of new catheter devices and the intra-procedural imaging. Many interventions that required an open heart surgery are now possible in a minimal invasive way. These procedures are becoming increasingly popular, because they mean a better patient satisfaction, faster recovery and less requirement for post-rehabilitation [McCl13]. Even the costs for surgeries can be reduced by 20% [Cohn97]. They also offer possibilities to treat patients who are inoperable with conventional methods [Walt07]. The most common examples of minimal invasive heart surgery and how they are executed under use of X-ray and Ultrasound imaging are described in the following. Some of the named interventions are already widely accepted, others are still object of research.

2.3.1 Aortic Valve Implantation

The transcatheter aortic valve implementation (TAVI) was one of the first minimal invasive heart interventions for structural heart disease and is widely accepted today. This type of intervention shows at least the same results as conventional open heart surgery but with less complications [Leon10, Zahn11]. During a TAVI, a catheter, which transports a crimped valve, is inserted via the femoral artery or via the heart's apex (transapical). This new valve is placed within the old natural aortic valve which is commonly calcified. The crimped valve is either inflated with a balloon or self expanding and replaces the old valve. A visualization of this method is shown in Figure 2.5⁴. This procedure is mostly X-ray driven. The catheter and the position is controlled and navigated with fluoroscopy and the help of contrast agent. Ultrasound is then used to control the functionality of the newly placed valve. This procedure is well supported by modern software tools like syngo Aortic Valve Guidance (Siemens Healthcare, Germany) [John10a, Zhen10, Kemp11].

2.3.2 Mitral Valve Repair

Mitral valves that do not close properly can cause a mitral valve regurgitation. Blood can flow back to the left atrium during the systolic phase and can cause long-term damages like an enlargement of the left atrium. Dyspnea, atrial fibrillation and cardiac insufficiency can be the consequences.

There are different approaches known to repair a mitral valve. The system used most is the MitraClip by Abbott (Abbott Park, North Chicago, Illinois, USA), which is displayed in Figure 2.7. Physicians that are using this system, are navigating a catheter from the femoral vein into the right atrium. Here a puncture of the septum has to be done and the catheter is moved into the left atrium, tilted and forwarded to the mitral valve. A schematic drawing of this route is shown in Figure

⁴Reproduced with permission from [Smit11], Copyright Massachusetts Medical Society.

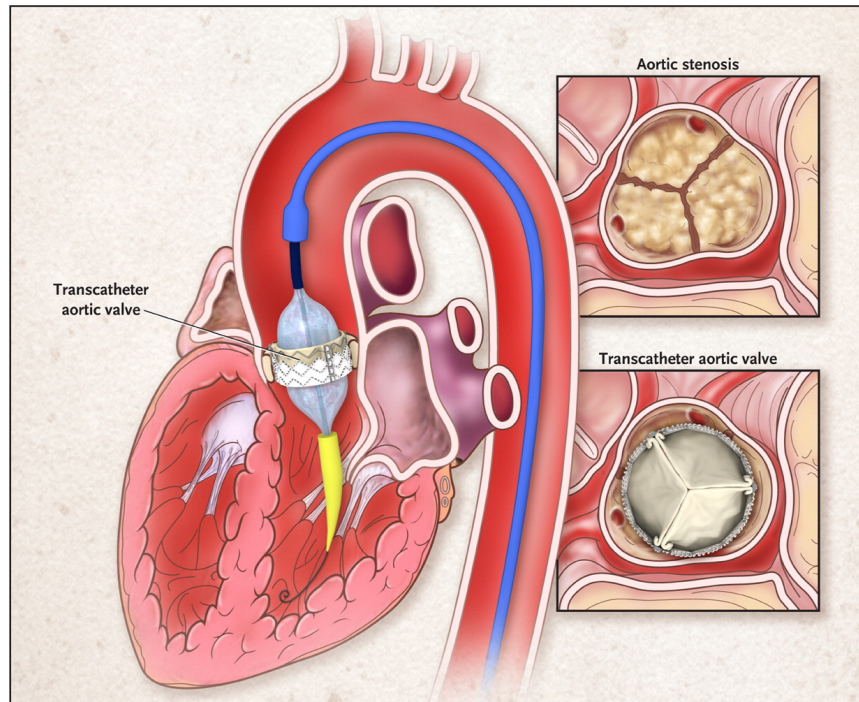


Figure 2.5: Schematic drawing of a TAVI procedure [Smit 11].

2.6. Then the two mitral valve leaflets are caught with a clip at the tip of the catheter and fasten together. The clip is locked and resides in the heart permanently. The results are similar to conventional surgery [Feld 05, Feld 09, Mais 13]. During this intervention, X-ray and TEE are heavily used together. Fluoroscopy is used to navigate the catheter into the right atrium and to the septum and to check the functionality and the general position of the catheter. Ultrasound is then necessary for the transeptal puncture and to check if both leaflets are properly caught with the clip. Another important part for Ultrasound is to evaluate the functionality of the treated valve with Doppler sonography to check if the back-flow of blood from the left heart chamber to the left atrium was reduced significantly. Lots of communication is necessary between the members of the surgical team, especially between the operators of Ultrasound, X-ray and the MitraClip device, to lead this intervention to success.

2.3.3 Mitral Valve Replacement

A relatively new field of research is the minimal invasive mitral valve replacement. In contrast to mitral valve repair, a new valve prosthesis is implemented. Several companies are working on artificial valves and workflows how to deliver and to anchor the prosthesis to the patient's heart [Pres 15]. Besides transapical or atriatomic approaches, which means making surgical access through the heart apex, respectively directly to a heart atrium, there are also transeptal variants in development, for example the CardiAQ system [Sond 15] or the NaviGate Cardiac Structures system [Navi 12]. For the transeptal access it is very likely that TEE Ultrasound and X-ray fluoroscopy are required for those techniques.

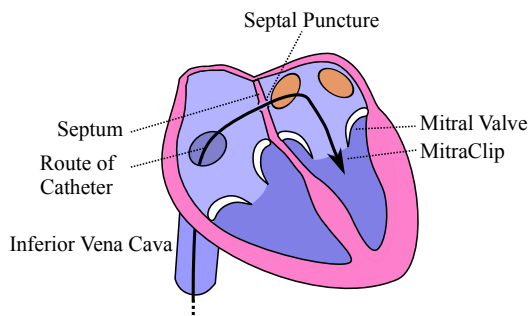


Figure 2.6: Ideal way of the catheter during a MitraClip procedure. Image originally from [Yadd 06].

Figure 2.7: The MitraClip device by Abbott Vascular, Abbott Park, Illinois, USA [Abbo 15].

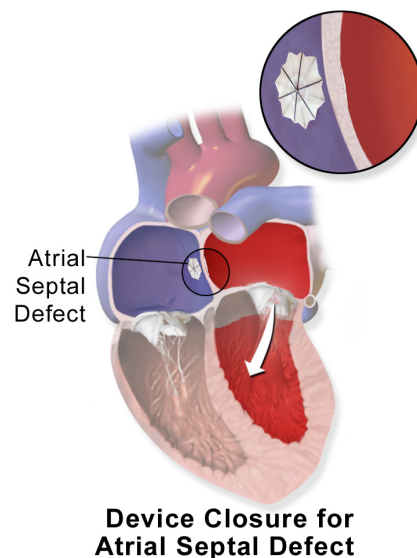


Figure 2.8: Device closure for Atrial Septal Defect [Blau 13].

2.3.4 Atrial Septal Defect / Patent Foramen Ovale Closure

An atrial septal defect (ASD) means the existence of a hole in the septum (shunt) between the right and the left atrium of the heart. That means that the oxygen-rich blood from the left atrium can flow directly to the right atrium to mix with the oxygen-poor blood, or vice versa. If the foramen ovale is not closing properly after birth, it is called patent foramen ovale (PFO). To prevent this behavior, which can lead to a lack of oxygen in different organs, tissue or brain, it can become necessary to close the shunt. Suitable minimal invasive methods are developed since the 1990s [Du 02]. Usually, the physician inserts a catheter with an double-umbrella-like structure into the heart and deploys it in a way, that the umbrella closes the hole in the septum completely. The procedure is again carried out under the use of X-ray fluoroscopy, to guide the catheter, and Ultrasound, to evaluate the position of the umbrella and the physiological parameters.

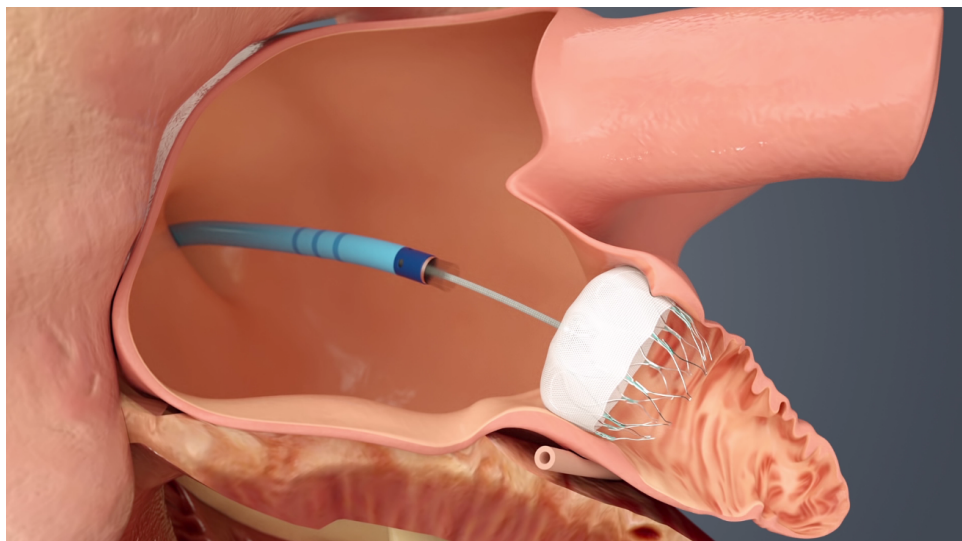


Figure 2.9: Drawing of the Watchman implant residing in the left atrial appendage [Bost 15].

2.3.5 Left Atrial Appendage Closure

The heart appendage is a small structure within the left atrium. Blood clots can accumulate in this pocket-like structure which can cause stroke, especially in patients suffering on atrial fibrillation. To lower this risk, closing the left atrial heart appendage is one possibility. There are several devices available to perform the left atrial appendage closure (LAAC) in a minimal invasive way. Here, the Watchman implant (see Figure 2.9), the Amplatzer Cardiac Plug [Park 11] or the LARIAT Suture Delivery Device [Bart 13] are widely accepted and are showing promising results compared to medical treatment [Holm 09]. Again, X-ray fluoroscopy and TEE Ultrasound are needed in combination to successfully implant the devices.

2.3.6 Paravalvular Leak Closure

Paravalvular Leak (PVL) closure summarizes the interventions that try to repair leaks of already replaced aortic and mitral valves [Smol 10]. Very similar to ASD closure, the physician inserts a double-umbrella device to close leaks that can occur after the implantation of new valves [Hour 92, Hein 06].

2.4 Fusion of Ultrasound and X-ray

All described minimal invasive interventions have in common that they are usually executed with the combination of X-ray fluoroscopy and TEE Ultrasound. By now, both modalities are detached systems with no connection and are used independently. X-ray imaging is performed by the cardiologist or surgeon at the left or right side of the patient whereas Ultrasound imaging is performed by the echographer or anesthesiologist at the head side of the patient. This is one reason why lots of communication between the whole surgical team is necessary. The sonographer has

to verbally navigate the surgeon or cardiologist, who is operating the catheter and is usually not particularly familiar with Ultrasound images. A fusion of the both systems can therefore lead to a better mutual understanding of the image contents and better and easier navigation and communication between the members of the interventional team. Potentially, such a fusion system can even allow new kinds of procedures and can help on saving X-ray dose and contrast agent.

Many research was done on the fusion topic in the past several years. That led to many different approaches that are described in Chapter 3. From a clinical point of view, the EchoNavigator system by Philips (Eindhoven, The Netherlands) is available and provides functionality of image fusion between TEE Ultrasound and X-ray fluoroscopy. It is already used by physicians, for example in [Kim 14], [Gafu 15] or [Cleg 15]. The key feature of this system is the registration of TEE Ultrasound and X-ray [Phil 14]. The user has the possibility to set markers in Ultrasound images, for example to mark soft tissue structures, which are displayed directly on the X-ray image. Another feature is that the 3D Ultrasound image can be aligned with the C-arm direction. The 3D TEE image can be manipulated in several ways directly by the interventionalists from the table side. Figure 2.10 shows a screenshot of the EchoNavigator. Physicians report that the system can help in understanding the relationship between Ultrasound images and the device for treating structural heart disease [Phil 14]. They also see the potential to reduce the amount of contrast agent injections to lower the risks for the patient [Kim 14].

In general, a system for fusion of Ultrasound and X-ray can enable many more medical applications. An example is presented in [Hous 13, Aruj 14], where the authors established a system to extend the field of view of the TEE ultrasound 3D volume with compounding. Multiple sequentially recorded Ultrasound volumes are compounded to generate an even bigger volume. This is possible because the TEE probe registration is providing the position of the probe in a global coordinate system. A combined catheter tracking in both images during electrophysiologic (EP) procedures is shown in [Wu 13] and [Wu 14]. The authors use the known image relationship to rise the detection and tracking accuracy of EP catheters inside the human heart.

This new technology is becoming a trending topic in the medical world. Several medical publications are describing the TEE-X-ray-fusion as a promising approach to reduce X-ray dose, the amount of necessary contrast agent and procedure times [Hahn 15, Kron 15, Biag 15] or for improving the understanding of the relationship between the catheter device and the anatomy [Faga 14].

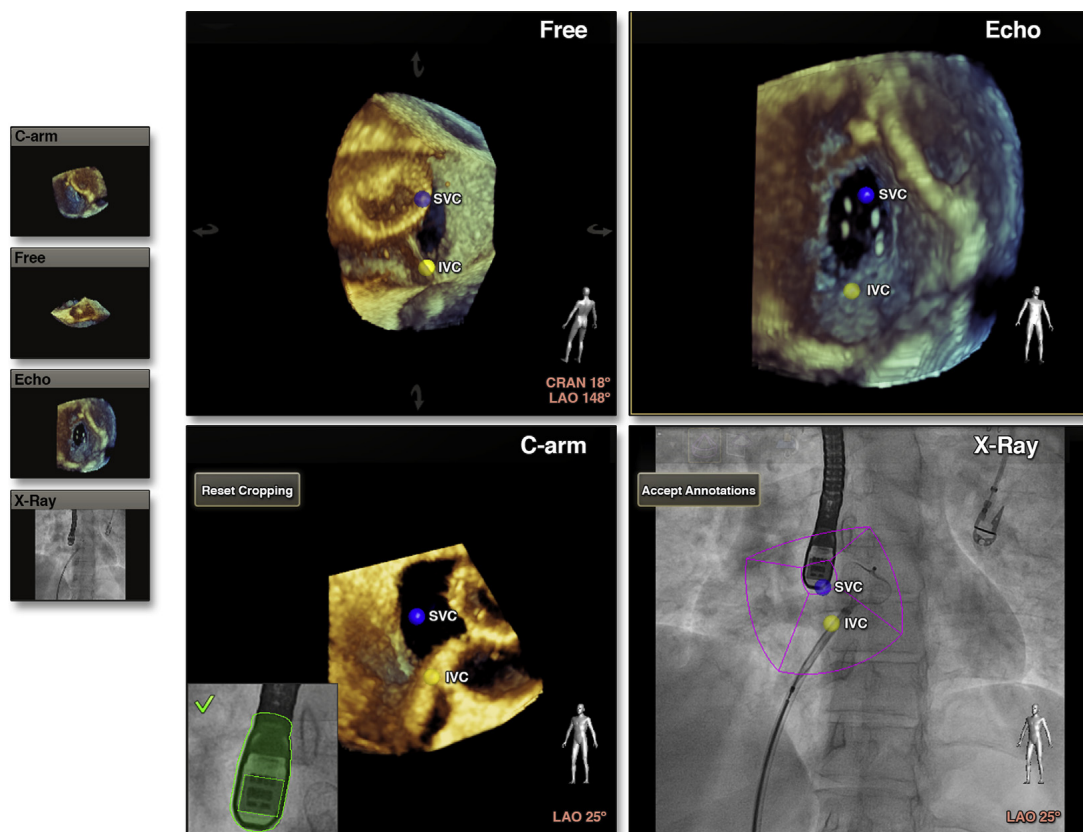


Figure 2.10: Screenshot of the EchoNavigator software by Philips (Eindhoven, The Netherlands). Image taken from [Cleg 15].

State of the Art in Fusion of Ultrasound & X-ray

3.1 2D-3D Registration.	18
3.2 Detection	22
3.3 EM Tracking	22
3.4 X-ray Fusion with other Ultrasound Devices.	23

In the past years, lots of research has been done on the topic of fusion of Ultrasound and fluoroscopic X-ray. An early system for TEE fusion was shown by [Gao 10]. Afterwards, multiple research groups joined on working on this topic with various techniques. Figure 3.2 provides an overview of published work in TEE-X-ray-fusion.

All of these methods have in common that they do not try to register Ultrasound images directly to X-ray images. Because of the completely different image characteristics, this would be rather challenging. Due to this reason, researchers have chosen an indirect registration. The TEE probe is usually visible in the X-ray image during the procedure. This allows to constantly register the TEE probe on the 2D image (see Figure 3.1) which is equivalent to estimating the pose of the probe in a 3D space. Previously, the Ultrasound image was calibrated to the now registered model to determine where it emerges from TEE probe in 3D space.

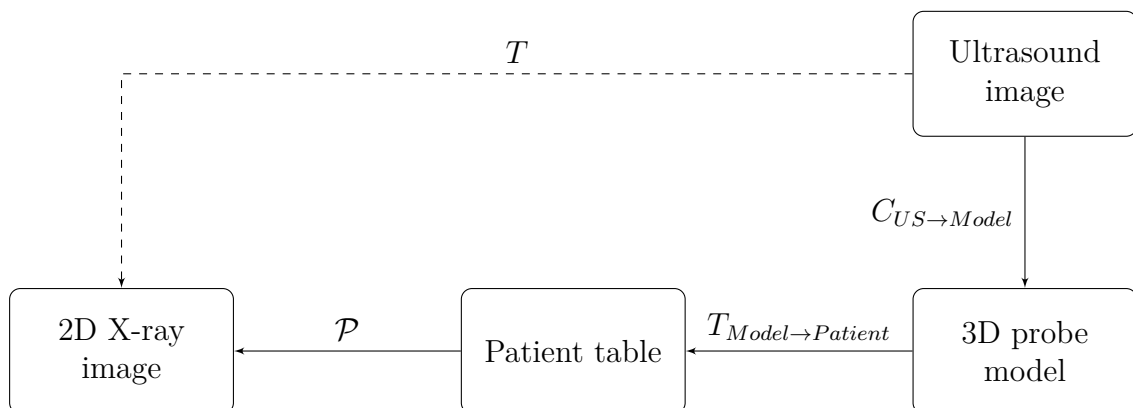


Figure 3.1: General workflow of Ultrasound to X-ray registration

Generally speaking, one is searching for a rigid-body transformation $T_{Model \rightarrow Patient}$ with a set of the six parameters S covering the six degrees of freedom (DOF) of a 3D model (visualized in Figure 4.1). This transformation contains the three translations (t_x, t_y, t_z) and the three rotations yaw, pitch and roll $(\theta_{yaw}, \theta_{pitch}, \theta_{roll})$ and aligns the 3D data correctly to the current X-ray image. If S is found correctly, it is then known where the probe lies relatively to the 3D patient coordinate system. A calibration matrix $C_{US \rightarrow Model}$ of the Ultrasound image to the ultrasound probe model gives the correct transformation from the Ultrasound image to the 3D patient coordinate system which can be projected onto the 2D X-ray image with the projection matrix \mathcal{P} . An abstract overall transformation T can then be described as:

$$T = \mathcal{P} \cdot T_{Model \rightarrow Patient} \cdot C_{US \rightarrow Model}. \quad (3.1)$$

In the following, several approaches from different research groups to find the transformation T are mentioned and described in a short form. The accuracy and runtime results that were presented by the different authors are summarized in Table 3.1.

3.1 2D-3D Registration

2D-3D registration is a key technology in medical imaging [Mark 12]. It is widely used to register pre-operative 3D data, for example a 3D CT volume, with live data, typically 2D X-ray fluoroscopy. A 2D-3D registration algorithm is an iterative process that consists of three basic parts. A DRR generator generates simulated X-ray images, so called digitally reconstructed radiographs (DRR) from a given 3D object. This simulated image is compared to the actual X-ray image. The comparison is performed with a similarity measure which results in a high similarity when the X-ray image and a DRR are correctly aligned. An optimizer is employed to determine a new set of rigid transformation parameters which are used to generate new DRR images from different views. After the optimization is stopped by a specific criterion, the optimization process will result in a good estimation of the 3D position of the 3D object. A detailed overview of the 2D-3D registration technique is presented in Chapter 4.

The commonly used technique to fuse Ultrasound with X-ray is based on 2D-3D registration. It was introduced by [Gao 10] and [Gao 12]. To estimate the 3D position, a model of the TEE probe is registered to the X-ray image via a 2D-3D registration algorithm [Penn 98]. Here, a 3D position of the probe is iteratively adapted using Powell's optimization method until the gradient differences measure of the projected probe model image and the X-ray image shows a high similarity. The method does not need additional modifications of the TEE probe and no specific set-up of the system for each procedure. The registration algorithm works well if the initial position for the 2D-3D registration is quite close to the correct position.

Other research groups followed this approach. In [Lang 10, Lang 11, Lang 12], the authors attached a custom rigid-body attachment including several ball markers to the tip of the probe. This extension was used to do point-based registration which

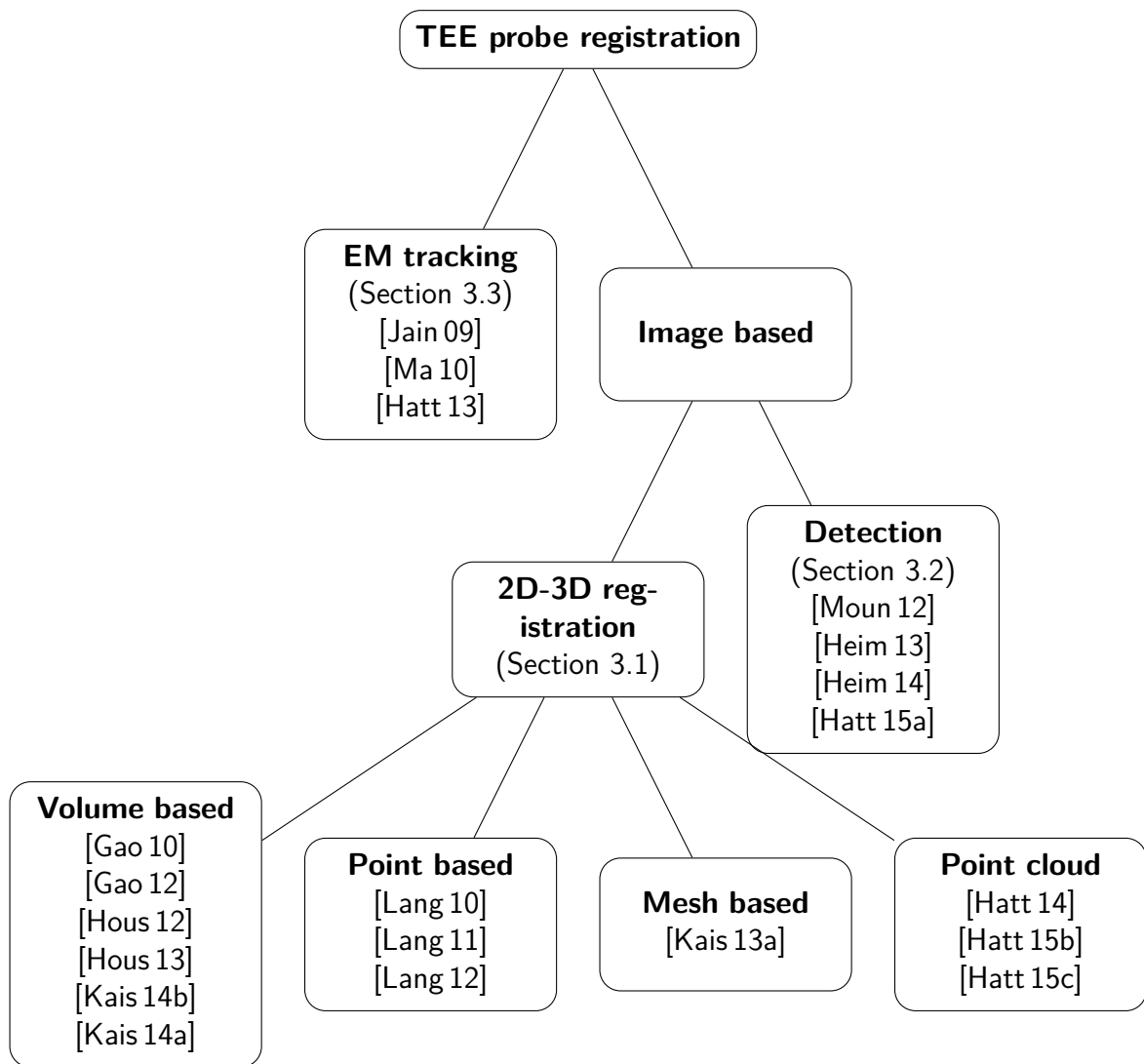


Figure 3.2: Literature overview for Ultrasound and X-ray fusion.

	Approach	Views	X [mm]	Y [mm]	Depth [mm]	Yaw [°]	Pitch [°]	Roll [°]	Success rate	2D error	3D error	Time (s)
[Moun 12] ^a	Det.	1	1.1	0.7	19.04	3.0	11.8	11.5	95	-	-	0.53 ^b
[Heim 13]	Det.	1	0.8	0.8	15	1.6	-	-	98.6	-	-	0.025
[Gao 12]	2D-3D reg.	2	0.06	0.04	0.16	0.17	1.16	1.05	-	1.8	6.8	8.0
[Lang 10] ^c	P.-b. reg.	1	0.006	0.001	0.5	0.03	0.03	0.03	-	2.9	3.5	- ^d
[Hatt 14] ^e	C.-b. reg.	1	0.52	0.52	0.74	0.69	2.44	2.44	82.2	1.27	-	0.72
[Hatt 15b]	C.-b. reg.	1	<i>f</i>	-	-	-	-	-	~98	2.1	-	0.014
[Hatt 15c]	C.-b. reg.	1 ^g	-	-	0.87	-	-	-	-	1.41	3.39	-
[Hatt 15a]	Det.	1	1.42	1.42	-	2.59	-	-	95.8	95.8	-	0.38
Chap. 5 [Kais 14a]	2D-3D reg.	2	0.08	0.07	0.12	0.11	0.41	0.84	95.4	-	1.53	1.76
Chap. 6 [Kais 13a]	2D-3D reg.	1	0.12	0.14	2.8	0.24	1.52	0.94	97.9	1.15	3.36	0.48
Chap. 6 [Kais 13a]	2D-3D reg.	2	0.08	0.12	0.17	0.15	0.35	1.25	98.2	3.72	3.88	1.14

Table 3.1: Overview over results for the different approaches presented in the literature. The presented results are the mean values for successful registrations/detections only. If not explicitly mentioned, the used data is from in vivo cases. The different authors evaluated the approaches in different ways. Therefore, not all data for comparison could be collected. The different approaches are abbreviated as 2D-3D reg. (image based 2D-3D registration), p.-b. reg. (point-based registration), c.-b. reg. (cloud-based registration) and det. (detection). Views means the number of images that are used for registration. 1 means monoplane images, 2 means biplane, respectively multiplane, data from two different views. The success rate shows the registrations/detections with errors below a reasonable border, which was seen as sufficient for clinical use by the authors. 2D error in mm usually means the mRPD (see Section 4.7.3) and 3D error the mTRF in mm (see Section 4.7.1). The registration/detection runtimes are always per frame per second.

^aDetection was done on phantom data only.

^bThe authors stated that the algorithms were not explicitly optimized for runtime performance.

^cThe only approach where the TEE probe was modified for point-based registration and tracking.

^dOnly tracking times of 0.05s per frame are reported, but no times for the first initial registration.

^eRegistration was done on phantom images with almost no noise or other structures.

^fDetailed errors for single parameters were not provided.

^gThis approach uses tomosynthesis.

yielded better results than pure image based registration in their experiments. The drawback here is that the probe has to be modified significantly, which has influences on the diameter of the probe as well. This will make the real clinical use of the method unlikely.

Another 2D-3D technique [Hatt 14] is to register point clouds representing the TEE probe which were generated by strong edges in the 2D X-ray image and the projected 3D gradient feature points of the TEE probe model. The results of this research are still preliminary, because the authors tested it on lab-images only.

Another similar approach was presented in [Hatt 15b]. To enhance the registration performance, the authors proposed an implicit evaluation of the similarity measure. They adapted the splatting technique [Birk 03], which transforms a 3D point-cloud representing the TEE probe, which was generated by a CT as well, to project the points on the detector plane. The points were not splatted directly, but were multiplied and summed up with the associated pixel of the X-ray image. This algorithm could be implemented very efficiently on a GPU. Therefore, the authors could achieve very high frames rates of 23.6 - 92.3 fps. The accuracy of the approach is a little bit below comparable approaches but still in a valid range. Unfortunately, the authors tested their approach only on 5 DOF, while they ignored the depth parameter. This approach is only reasonable when the C-arm is not rotated during the intervention.

Another recently published approach [Spei 14, Hatt 15c] showed the registration of a TEE probe with tomosynthetic X-ray images. Tomosynthesis is a technique to generate tomographic images from a limited angle projection geometry [Dobb 03]. In contrast to CT, scan images for tomosynthesis are acquired from a very limited range of angles. Therefore, it is only possible to reconstruct image slices at a certain depth and with limited thickness. One can see tomosynthesis as an incomplete CT reconstruction. The authors of [Spei 14, Hatt 15c] used a special X-ray prototype system. Their scanning-beam digital X-ray (SBDX) technology is able to record and reconstruct tomosynthetic images with 15 fps. In the first step of TEE probe pose estimation on these images, they try to find key points of the probe with the help of the vesselness filter [Fran 98] and connected component analysis. Then they make use of the given 3D information of the tomosynthetic image, which is indeed a stack of 32 image planes, to estimate the 3D location of the previously detected key points. The basic principle of these images is that an object appears sharper if it is near to the center of the tomosynthesis stack and appears blurred if it is further away. This can be used to better estimate an objects depth than in normal conventional X-ray images. The principal component analysis (PCA) is then used to detect the probe orientation. This initial probe pose is then refined by a 2D-3D registration which employs the same method as already described in [Hatt 14]. The advantage of this approach is the more accurate depth estimation of the probe from a single C-arm position. Further results are similar to other presented approaches. The authors did not provide any information about the runtime of the algorithm but stated that this is an initial study.

The 2D-3D registration based approach, which is used in this thesis, is presented in Chapter 4.

3.2 Detection

Another technique to identify the probe position is via feature detection, which was introduced in [Moun12]. Here, features of the ultrasound probe are detected in the 2D X-ray image. The inplane parameters are found with discriminative learning methods. The authors trained three different classifiers (2D position, yaw and size of the probe, which is related to the depth) with Probabilistic Boosting Trees and Haar-like features on annotated fluoroscopic X-ray scenes [Wu11]. The fluoro image is resized to 128×128 pixels which makes the detection very fast. The out-of-plane parameters are found with fast binary template matching. Different binary projections of the TEE probe model were generated from many different values of roll and pitch and were compiled into a template library, which can be searched very effectively. The reported accuracy is not as good as for the 2D-3D registration approaches, but the detection is outperforming them in runtime.

An update of this discriminative learning approach was given in [Heim13]. The accuracy of this technique is heavily dependent on the availability, quantity and quality of training data, which is usually difficult to acquire for medical images. The authors improve this technique by generating synthetical training data from a TEE probe model in combination with real clinical X-ray images. The advantage here is, that one can generate any number of images with the correct ground truth position of the probe. They then use the technique of unsupervised domain adaption [Marg11] to adapt the classifier, which was trained on synthetic data, to in vivo data. The authors have been able to significantly improve the detection accuracy with this new technique.

Another detection technique was presented in [Hatt15a] where the authors used Hough forests from [Gall13] to simultaneously detect different medical devices in real-time, including a TEE probe. A Hough forest [Gall11] is a random forest which is collection of decision trees. It can solve the questions of classification of image patches, here patches of a TEE probe image, and the location of that image patch, here which part of the TEE probe is represented by the patch. Multiple training phases, where image patches from different preprocessing steps are classified and splitting rules are elaborated, were used to establish different decision trees. After the training, each new patch will be put into each decision tree which will then vote for a object part and a position. The resulting Hough image will then show peaks for the specific objects. The presented results are promising but are currently behind the results of the detection approach of [Heim14].

3.3 EM Tracking

Another possible method to obtain the position of a TEE probe is by electromagnetic (EM) tracking which was shown in [Jain09]. The authors wrapped the probe tip in an additional plastic cover that contains the EM sensors and attached a tracking sensor to the patient table. The Ultrasound image was calibrated to the probe EM sensors and the sensors on the table to an X-ray reference frame. The drawbacks of this method are the additional effort to setup the EM sensors and the calibration of

the reference frame, which can be a possible showstopper in a clinical environment. The approach was tested in phantom studies. This method was recently extended [Hatt 13] to be able to track the wrapped TEE probe in MR and X-ray.

A similar approach was used in [Lint 10] and [Moor 10]. This research resulted in an augmented reality system [Moor 13] which was used to support interventions with the NeoChord device [Seeb 10], a device to implant new chordae to prolapsing mitral valve leaflets. Usually, these interventions are done without X-ray guidance. Additional sensors were attached to the NeoChord tool and the TEE probe, thus they could be tracked by EM technology. The authors could significantly improve the success rate and the procedure time of mitral valve repair interventions performed with the NeoChord device.

3.4 X-ray Fusion with other Ultrasound Devices

More research was done on fusion of X-ray fluoroscopy with different Ultrasound catheters which is described in the following section.

3.4.1 Trans-thoracic Echo

[Ma 10] published an approach to track a hand-held Ultrasound probe for Transthoracic echocardiogram (TTE). TTE is applied from a hand-held probe from the patient's chest. The probe was fixed on a robotic arm that could be navigated by the sonographer. The robotic arm, the X-ray table and the C-arm were tracked by an optical tracking system. The transformation matrix from TTE probe to the robotic arm was given by the robot kinematics. Due to the yet known relationship of the different devices, the authors were able to establish a registration from Ultrasound to X-ray. They have been able to overlay data from segmented Ultrasound and Ultrasound volumes. They also used it for establishing extended field of view 3D Ultrasound images by volume compounding. There is no further work known on this topic. Nowadays, TEE is preferred over TTE by examiners because of better image quality and unrestricted access to particular sonographic views of the heart.

3.4.2 Intra-cardiac Echo

Intra-cardiac Echocardiography (ICE) is a sonographic technique where an ultrasound catheter is inserted via the arteria femoralis into the right atrium of the heart. This relatively small catheter - the diameter ranges from 8 to 11 French (2.7 to 3.7 mm) - views heart structures directly from inside the heart. Its image quality is not as good as for TEE images but still sufficient. Modern ICE systems have also the possibility of creating a 3D volumetric representation, but with much more limited field of view due to Ultrasound beam opening angles of 90 to 22 degrees. In [Ralo 14], the authors implemented fiducial markers into the ICE catheter by design, which is shown in Figure 3.3. This gave them the ability to detect the markers and to determine the position and rotation of the probe. A probe without markers is not completely detectable, because of the small size and missing unambiguity under projection.

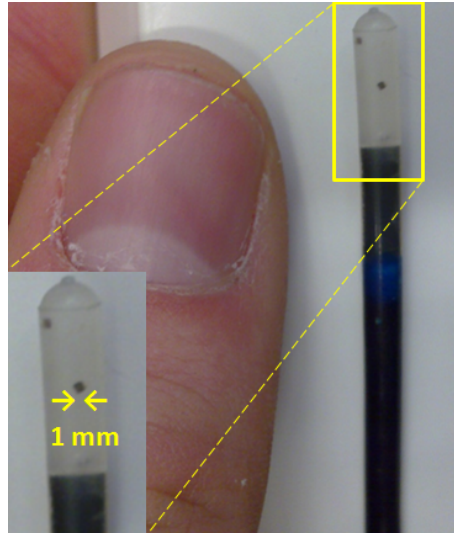


Figure 3.3: Example of an ICE catheter with implemented ball markers at the catheter tip. [Ralo 14]

The results of this first research on X-ray-ICE-fusion are still preliminary, which can be seen in the relatively high detection errors of the six rigid parameters.

3.4.3 Intravascular Ultrasound

Intravascular Ultrasound (IVUS) is an imaging technique where a catheter with an Ultrasound transducer at its tip is inserted into blood vessels, most commonly the coronary arteries. IVUS is then providing a 360-degree-cut-plane view of the current vessel from inside to outside to provide information about the vessel wall. An example is shown in Figure 3.4¹, in the lower left image. A physician can then generate vessel maps (right image) by pulling back the Ultrasound tip inside the vessel, commonly with motorized support. This map will especially show important information about plaques, lesions or tissue characterization.

[Wang 11, Pras 15] showed a technique to co-register X-ray fluoroscopy with IVUS images. The position of the catheter is detected and tracked in the X-ray image while pulling back the Ultrasound tip to generate a mapping of a vessel. This will produce automatic correspondence between the IVUS and the X-ray images. For example, a physician can then mark plaques in the Ultrasound image which is directly showed in X-ray (upper left image in Figure 3.4). That helps to save time in the clinical daily work and also enables users with lower expertise to perform this interventions.

¹Image courtesy of Siemens Healthcare GmbH, Forchheim, Germany.

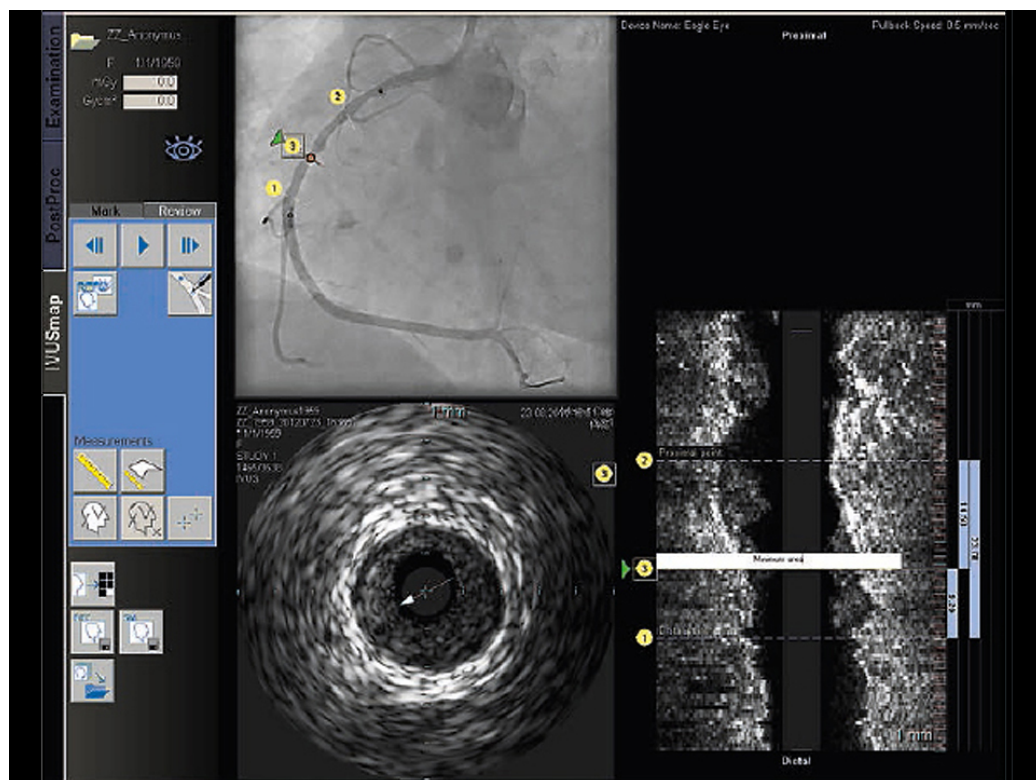


Figure 3.4: Screenshot of the application IVUSmap by Siemens Healthcare GmbH, Germany.

2D-3D Registration Framework

4.1 C-arm Projection Geometry	28
4.2 3D TEE Probe Model	31
4.3 DRR Generator	32
4.4 Similarity Measure	35
4.5 Optimization Methods.	38
4.6 Optimization Strategy.	41
4.7 Quality and Performance Criteria	43
4.8 Ground Truth Generation.	46

The goal of a 2D-3D registration algorithm is to estimate the position of a 3D object in a 3D space by only using a 2D projection image which contains the projection of this 3D object. 2D-3D registration has become an universal tool in medical imaging to align preoperative 3D volume data, for example from CT, MR or PET, to 2D fluoroscopic X-ray images. This helps to provide additional information to the physician before and during an intervention and enables new procedures and workflows [Liao 13]. Some examples for successfully employed 2D-3D registration techniques can be found in [Fu 08, Livy 03, Jomi 06, Otak 12].

Typically, an image-based 2D-3D registration algorithm [Lemi 94, Penn 00, Hipw 03] is an iterative process and consists of three main parts which are shown in Figure 4.2. Starting with an initial position of a 3D object, a digitally reconstructed radiograph (DRR) is generated by a DRR generator. In fact, a DRR is a simulated X-ray image of the 3D object. This DRR will be compared to the current X-ray image with the help of a similarity measure. A good matching position between X-ray image and DRR will result in a high similarity, a high deviation in low similarity. The algorithm will generate a number of different DRRs and will compare these to the current X-ray image. This iterative process is driven by the optimizer which calculates new position parameters for each DRR. These rigid parameters are translation in three directions (t_x, t_y, t_z) and the three rotations around the three object axes ($\theta_{pitch}, \theta_{yaw}, \theta_{roll}$), which are indeed the Euler angles. See Figure 4.1 for an illustration of all parameters according to the TEE probe. The optimization process will terminate if a certain criterion is reached. This should result in a good matching position.

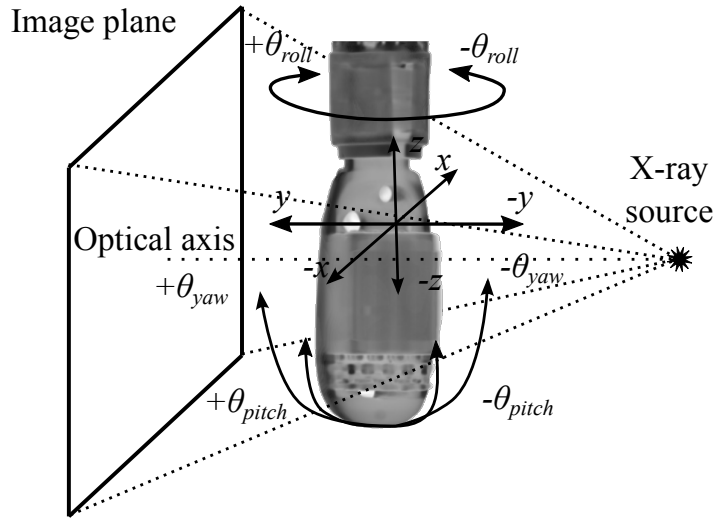


Figure 4.1: TEE probe with six degrees of freedom and the C-arm's projection geometry.

The optimization can be expressed as follows. Let S be a set of the six rigid parameters of an object, that transforms the object in 3D space. \mathcal{P} is the C-arm projection matrix, which is explained in detail in Section 4.1. The task of the optimizer is now to minimize a similarity measure function sim , which results in the final registration matrix \mathcal{R} :

$$\mathcal{R} = \min(sim(I_{DRR}(\mathcal{P}, S), I_{Xray})). \quad (4.1)$$

The similarity measure compares a generated DRR image I_{DRR} , which is parameterized with \mathcal{P} and S , and the original X-ray image I_{Xray} . The parameters S are about to change in each iteration, while \mathcal{P} is constant for one specific X-ray image.

This chapter describes the 2D-3D registration framework that is used in this thesis to register the TEE probe model to X-ray images. Parts of this chapter have already been published in [Kais 11, Kais 13a, Kais 14a, Kais 14d].

4.1 C-arm Projection Geometry

The whole method of 2D-3D registration is based on the perspective projection geometry of the C-arm. It is necessary to understand this geometry to understand the basics of 2D-3D registration. A schematic drawing of the projection geometry is shown in Figure 4.3. SID stands for source to image distance and is the orthogonal distance from the X-ray source to the detector, SOD is the distance from the source to the isocenter of the C-arm. The whole C-arm projection matrix is defined as:

$$\mathcal{P} = \mathcal{P}' \cdot T_z \cdot T_x \cdot T_d \cdot \mathcal{C}. \quad (4.2)$$

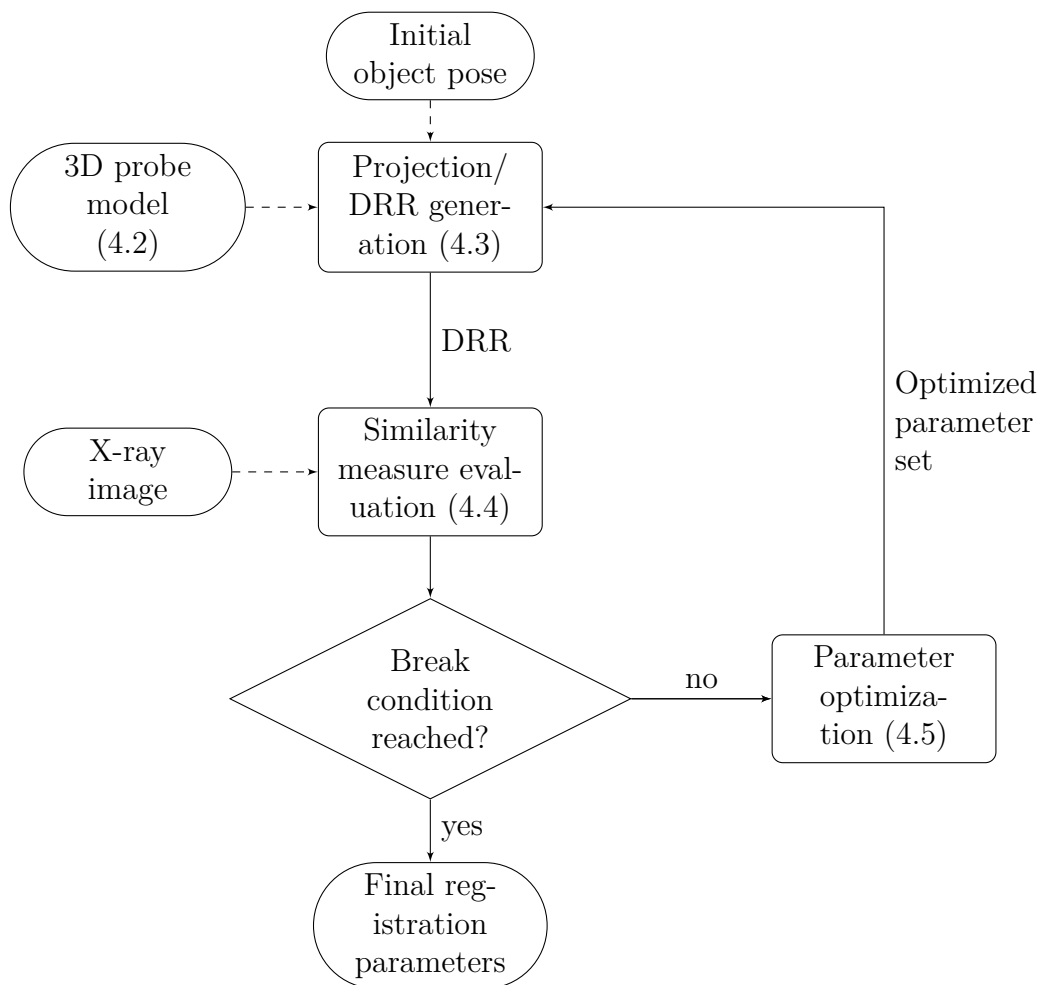


Figure 4.2: General workflow of a 2D-3D registration algorithm.

\mathcal{C} covers the rotation around the both C-arm angles α and γ (see Section 2.1 for details) with:

$$\mathcal{C} = T_\gamma \cdot T_\alpha \quad (4.3)$$

$$\mathcal{C} = \begin{pmatrix} 1 & 0 & 0 & 0 \\ 0 & \cos(\gamma) & \sin(\gamma) & 0 \\ 0 & -\sin(\gamma) & \cos(\gamma) & 0 \\ 0 & 0 & 0 & 1 \end{pmatrix} \cdot \begin{pmatrix} \cos(\alpha) & \sin(\alpha) & 0 & 0 \\ -\sin(\alpha) & \cos(\alpha) & 0 & 0 \\ 0 & 0 & 1 & 0 \\ 0 & 0 & 0 & 1 \end{pmatrix}. \quad (4.4)$$

The matrix T_d is a shift of the origin of the coordinate system to the isocenter. T_x is a rotation about 90 degrees around the x-axis, T_z about 180 degrees around the z-axis. This is a reorientation of the X-ray tube centered coordinate system to a patient coordinate system. All further transformations in this thesis will be performed in the patient coordinate system. The initial position is the patient who is lying on the operation table. The origin of this coordinate system is defined in the isocenter of the C-arm. The directions of the single axes are:

- X: from left hand side, or left anterior oblique (LAO), to right hand side, or right anterior oblique (RAO)
- Y: from patient's front side, or anterior, to the patients back side, or posterior,
- Z: from feet, or caudal (CAUD), to head, or cranial (CRAN).

P' is the actual projection matrix which is defined as:

$$P' = \begin{pmatrix} \frac{SID}{p} & 0 & \frac{sz_x}{2} & 0 \\ 0 & \frac{SID}{p} & \frac{sz_y}{2} & 0 \\ 0 & 0 & 1 & 0 \end{pmatrix}. \quad (4.5)$$

The physical pixel spacing of the detector is given as p , the size of the detector in image pixels in image x- and y-directions is given by (sz_x, sz_y) .

While speaking of obtaining a 3D position from a single 2D image, one should distinguish between inplane and out-of-plane parameters (see Figure 4.1). Inplane parameters are the three parameters (t_x, t_y, θ_{yaw}) that are parallel to the image plane. Therefore, they are easy to determine because a change of these parameters will result in a relatively large change of the position on the image plane. Out-of-plane parameters $(t_z, \theta_{pitch}, \theta_{roll})$ are more difficult to determine because they only cause a small change of the projected 3D object which can be hardly visible on the projection image. Out-of-plane parameters are parallel to the optical axis. An example of the different characteristic of in- and out-of-plane parameters can be seen in Figure 4.4. The images show the starting position and then the position after translation as an overlay. One can clearly see the huge change that is caused by the relative small translation in inplane direction and the small change for a large translation in out-of-plane direction.

This effect can be explained with the following example. Assuming a ball with a diameter of 1 mm located directly in the isocenter and a common pixel spacing of 0.154 mm per pixel, SID of 1200 mm and SOD of 750 mm. The observable magnification m on the detector is than given by the relationship $\frac{SID}{SOD} = 1.6$. Therefore,

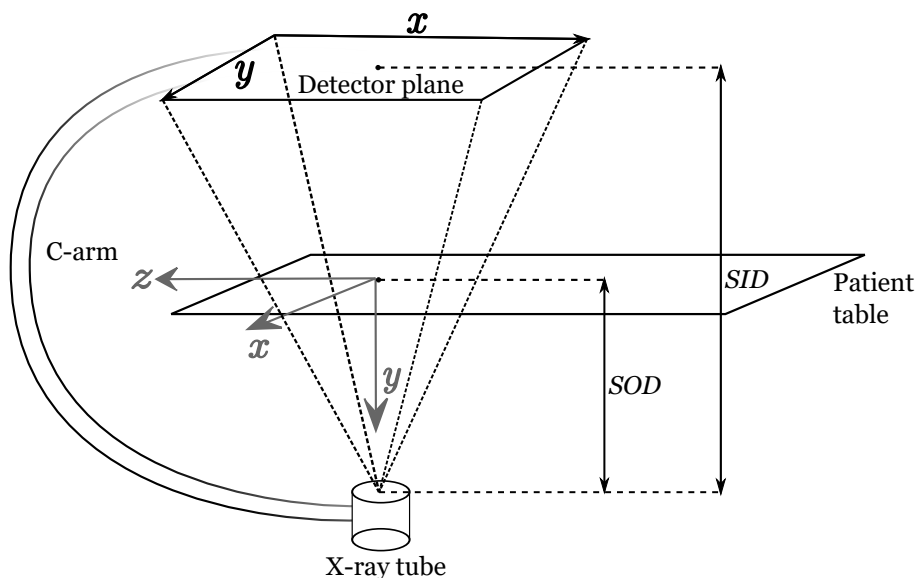


Figure 4.3: Schematic drawing of the projection geometry of a C-arm.

the ball has a projection image of a diameter of 1.6 mm on the image plane, which is around 10.4 pixels. To cause a pixel shift of 1 pixel (px), one has to shift the ball by:

$$\frac{1px \cdot p}{m} = \frac{0.154}{1.6} = 0.096 \text{ mm} \quad (4.6)$$

parallel to the detector plane.

To cause the same pixel shift by only adjusting the depth parameter, or with other words, to let the ball grow about 0.096 mm in diameter in the projection image, one has to shift it in depth direction by:

$$SOD - \frac{SID}{1.696} = 42.5 \text{ mm.} \quad (4.7)$$

For potential detection/registration algorithms this means that it is challenging to determine the out-of-plane parameters with high accuracy.

4.2 3D TEE Probe Model

The Ultrasound device which was used in this thesis is a new 3D TEE transducer by Siemens Healthcare (Mountain View, CA, USA).

The TEE probe was designed directly for better registration/detection under X-ray imaging. By design, three metal ball markers are implemented in the hull of the probe and three holes are drilled into the back side. Figure 4.5 shows a volume rendering of the 3D TEE probe model. One can see the two ball markers in the upper part as well as the two holes in the back. The third marker is at the tip of the probe and the third hole is not visible from this view. These positive (balls) and negative (holes) markers were integrated to establish additional landmarks and, even more important, to break up projection symmetry between certain X-ray angles.

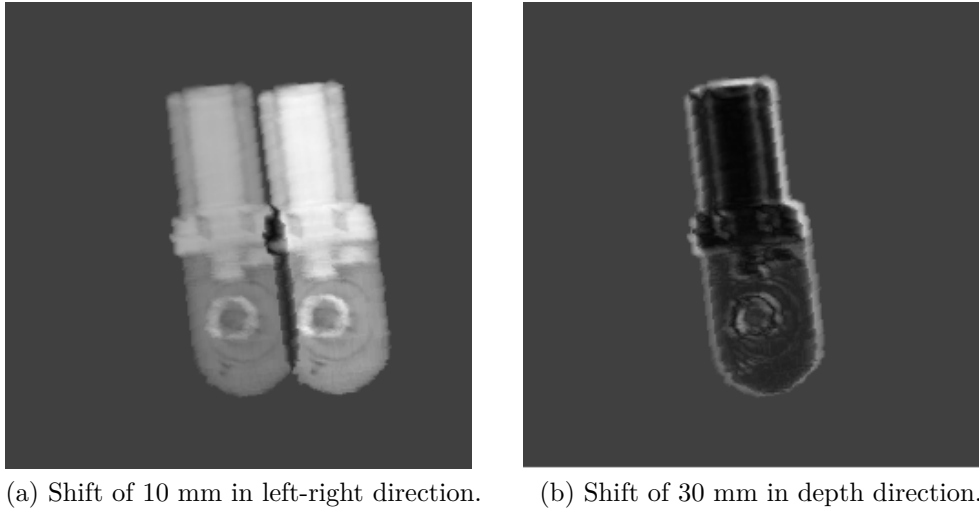


Figure 4.4: Example of different characteristics of (a) inplane and (b) out-of-plane parameters.

Figure 4.6 illustrates the symmetry problem by showing X-ray images from a TEE probe with different rotations and without additional markers. Although the X-ray projections are visually very unequal for different rotations, it can happen that two X-ray projection images for two different rotations are very similar. This is due to the left/right symmetry of the TEE probe under X-ray projection. One can not distinguish if the probe is shown from the front- or the backside. In general, an ambiguous projection image for two specific angles of $(\theta_{roll}, \theta_{pitch})$ can be obtained by a second set of angles:

$$\begin{cases} (2\pi - \theta_{roll}, -\theta_{pitch}) & \text{if } 0 \leq \theta_{roll} \leq 2\pi \\ (-2\pi - \theta_{roll}, -\theta_{pitch}) & \text{if } 0 > \theta_{roll} > -2\pi \end{cases}. \quad (4.8)$$

The 3D dataset of the transducer which was used for the 3D model was acquired with a high-resolution industrial CT scanner at Fraunhofer-Institut für Integrierte Schaltungen (Entwicklungszentrum Röntgentechnik, Fürth, Germany) with a resolution of 0.1 mm per voxel with a high X-ray dose to minimize metal artifacts in the 3D reconstruction as best as possible [Barr04]. Still remaining artifacts, for example streak artifacts from very high X-ray attenuation structures, were eliminated by manual post-processing on each reconstructed slice of the 3D volume with an image mask (see Figure 4.7). The TEE transducer consists of different materials with different attenuation. In the final DRR, structures with lower X-ray attenuation would be interfered and overlaid by those high attenuation artifacts if they would not be removed by manual post-processing. This would lead to higher inaccuracies in the final registration result.

4.3 DRR Generator

The DRR Generator is an algorithm which takes a 3D volume as input and generates simulated X-ray images (digitally reconstructed radiograph, DRR) from an arbitrary



Figure 4.5: Volume rendering of the Mirco-CT of the TEE probe.

view. The creation of DRRs relies on the basic theory of X-ray image generation. An X-ray image is created by measuring the incoming X-ray intensity on a detector. Different materials have a varying property of radiopacity which results in different X-ray absorption. The remaining X-ray energy, which is measure by the detector, is mapped to different gray values. The loss of intensity for X-rays traveling trough tissue can be modeled by the Beer-Lambert's law of the attenuation of light:

$$\mathcal{I} = \mathcal{I}_T e^{-\mu t}. \quad (4.9)$$

\mathcal{I} is the resulting intensity on the detector and \mathcal{I}_T the emitted intensity of the X-ray tube. The attenuation coefficient μ characterizes how well X-ray radiation can penetrate this material. The material's thickness is given by t . The human body consists of many different substances and tissues with different attenuation coefficients. Therefore, μ is a function of space and the integral of x parameterizes the X-ray beam. The Equation 4.9 can than be written as:

$$\mathcal{I} = \mathcal{I}_T \exp\left(-\int \mu(x) dx\right). \quad (4.10)$$

A 3D CT volume is composed of equidistant voxels that are discretely approximating a real object. The employed DRR generator is a ray-casting, or forward-projection, algorithm like in [Wein08]. That means, it literally shoots rays from the X-ray source in direction of the detector following the given projection geometry. A ray's direction is calculated from the X-ray source to the specific pixel on the detector. The gray

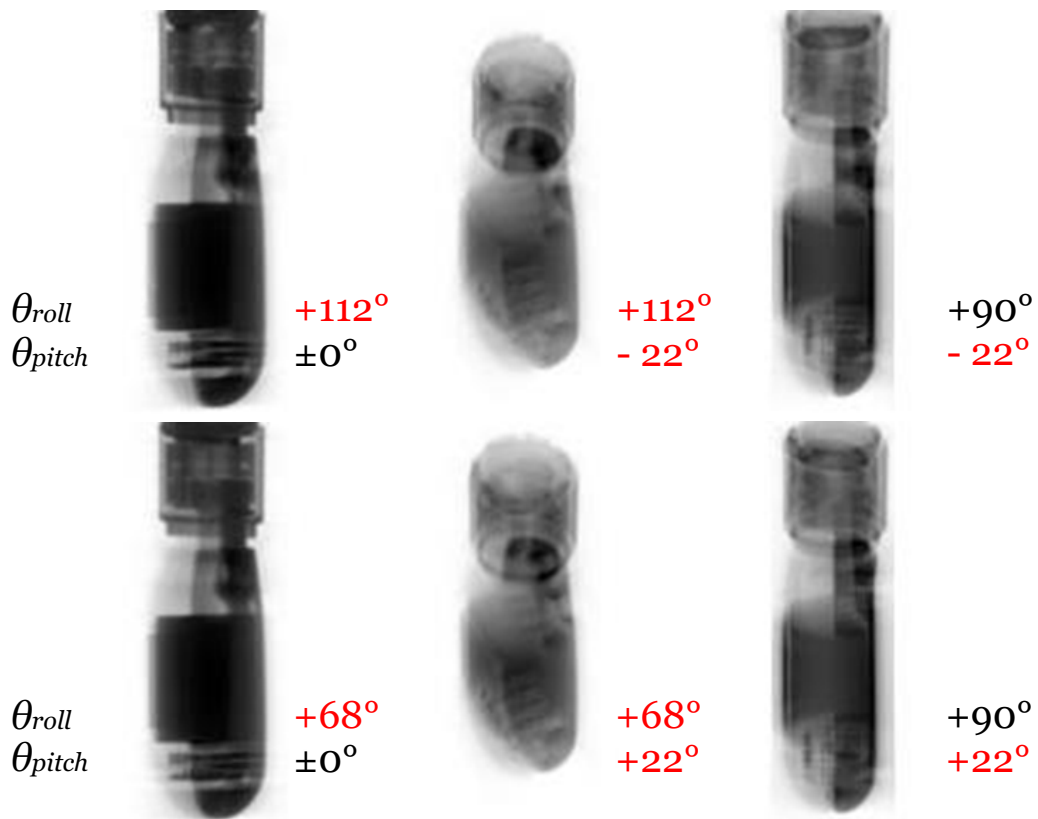


Figure 4.6: Examples for symmetric probe projection images under completely different probe rotations. Without markers this can be only solved by a second image from another projection. Upper angles are for ϕ_{roll} and lower are for ϕ_{pitch} .

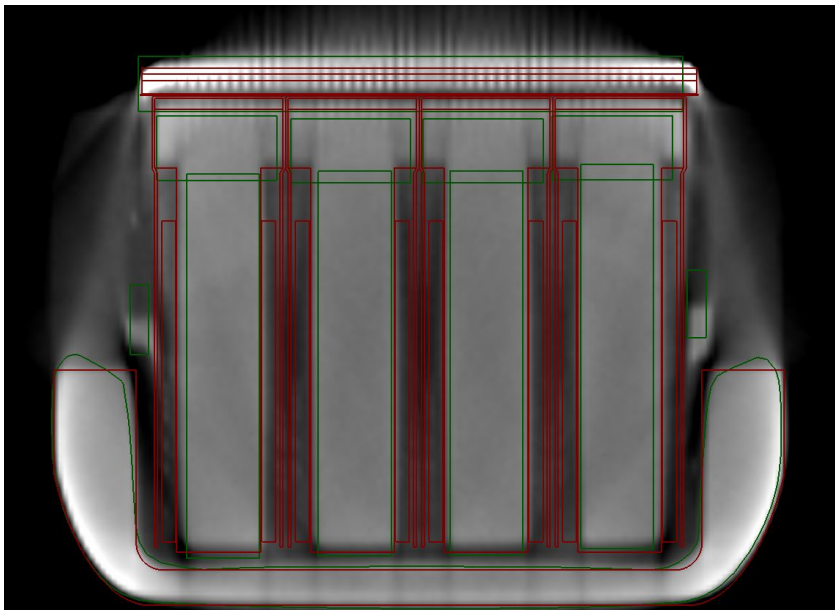


Figure 4.7: One slice of the reconstructed 3D volume with the applied mask (red contour) for removing metal artifacts.

value of a pixel is calculated by summing up all gray values of the penetrated voxels along the ray with:

$$\mathcal{I} = \mathcal{I}_T \exp\left(-\sum_0^i \mu_i \Delta t\right), \quad (4.11)$$

which is an approximation of Equation 4.10. Here, Δt is the size of one voxel along an X-ray beam and μ_i is the intensity value assigned to this voxel. This is done for every pixel on the detector plane.

To achieve a image impression similar to a real X-ray image, it is necessary to normalize the forward-projected DRR image. There are many parameters that can change the image impression significantly during the X-ray image generation process. Examples are tube voltage, applied X-ray dose per frame, framerate, the size of the patient or medical instruments in the X-ray image. The image impression can also be changed during post-processing, for example via image-windowing, edge enhancement or noise suppression. This should be considered in the DRR normalization process but also in the selection of an appropriate X-ray image acquisition protocol. In this thesis, the post-processing is handled by employing different transfer functions like described in [Heim 14]. The function for mapping the single intensities \mathcal{I}_n , resulting from the ray-casting, to normalized gray values within the interval $[0, 1]$ is:

$$\mathcal{I} = 1 - \min([\mathcal{I}_T e^{\mathcal{I}_n/\kappa} - \lambda], 1) \quad (4.12)$$

while κ and λ are normalization coefficients. Examples for different transfer functions can be seen in Figure 4.8. A linear mapping, like it is shown in Figure 4.8c, turned out to be not sufficient because it overemphasizes different low contrast structures of the TEE probe. Figure 4.8d shows a linear mapping function which result in too many visible probe details. However, the curved matching function, like shown in Figure 4.8a, is too steep which results in a less detailed image for high contrast probe structures. The result of a good mapping function is shown in Figure 4.8b.

4.4 Similarity Measure

A similarity measure is a function that is used by the optimization algorithm to calculate the similarity of two input images. For 2D-3D registration, one compares the original X-ray image with the different DRR images. The result is a similarity score for each comparison. Ideally, comparing the same image will result in the highest possible value.

4.4.1 Types of Similarity Measures

Lots of research was done in the past on a wide range of different similarity measures [Penn 98]. Generally, one can group them into three categories that are described in the following.

Intensity-based Similarity Measures

These measures perform evaluation on the pixel intensity values only. Usually, they are lacking in robustness when working with image data from different modalities

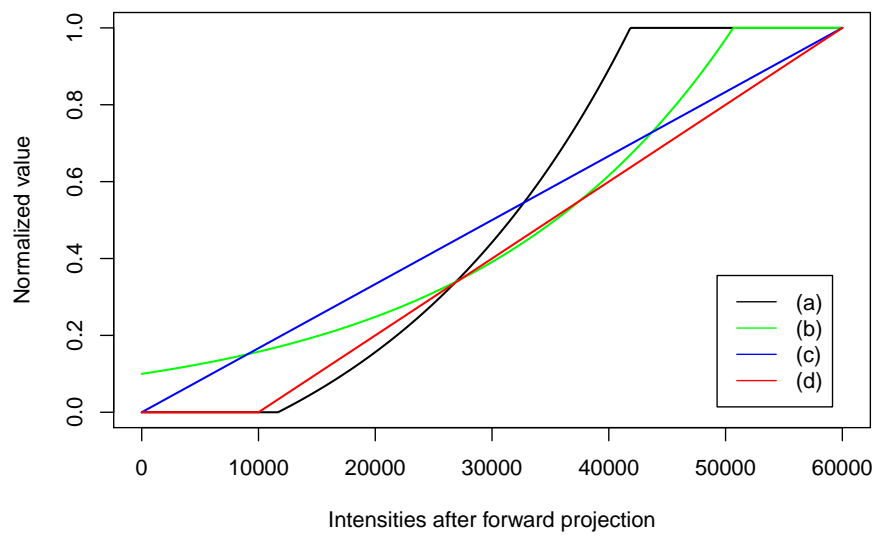
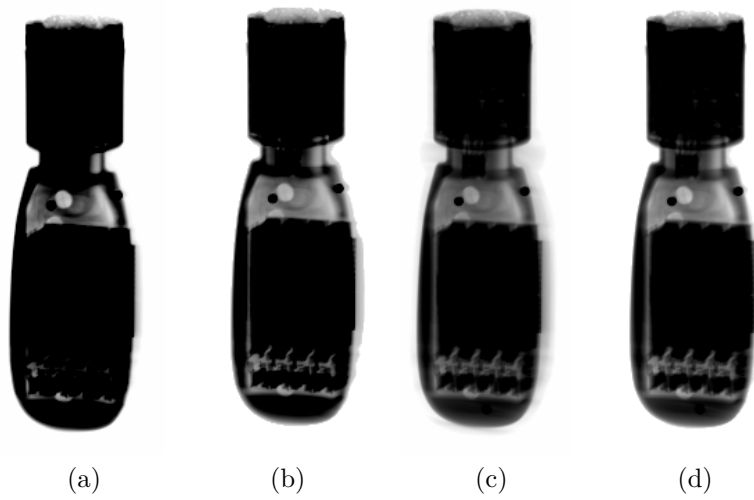


Figure 4.8: Different transfer curves and corresponding DRRs.

or changing contrast. Popular examples are sum of squared differences (SSD), sum of absolute differences (SAD) [Sebe00], variance of differences (VD) [Cox94] and normalized cross correlation (NCC) [Oppe75].

Spatial-information-based Measures

These measures evaluate spatial information of images like edges or corners. A pre-processing step is necessary, for example applying an edge detection filter on both images. Examples are pattern intensity (PI) [Bose90], gradient correlation (GC) [Lemi94, Gott96], gradient differences (GD) [Penn98] or normalized gradient fields (NGF)[Habe06].

Histogram-based Measures

Normalized mutual information (NMI) [Viol97][Maes97], entropy of differences (ED) [Buzu97], sum of conditional variances (SCV) [Pick09], conditional variances of differences (CVD) [Maki12] and weighted histogram of gradient directions (WHGD) [Ghaf15] are similarity measures which are only working on histograms of images. The histograms can be established by using the gray values only but also on pre-processed image data like gradient information.

Combinations

Combinations of different similarity measures exist as well, for example maximization of combined mutual information and gradient information [Plui00]. Systems that employ multiple measures at the same time are known as well [Wack09].

4.4.2 Employed Similarity Measures

Two similarity measures turned out to be useful for the task of 2D-3D TEE probe registration in this thesis: gradient correlation, which was used in [Kais13a], and normalized gradient fields which was employed in [Kais14a]. An evaluation of different similarity measures for this task can be found in [Kais11].

Gradient Correlation

As the first step for calculating the similarity with the gradient correlation (GC) similarity measure, the horizontal and vertical gradient images of X-ray and DRR images are computed. Afterwards, the normalized cross correlation (NCC) between the resulting vertical and horizontal gradient images is calculated. The horizontal and vertical gradient images G_x and G_y for the X-ray (I_1) images, respectively DRR (I_2) images, are generated by a common 3×3 Sobel edge operator [Sobe68]. GC is then defined as:

$$GC(I_1, I_2) = NCC(G_x(I_1), G_x(I_2))/2 + NCC(G_y(I_1), G_y(I_2))/2. \quad (4.13)$$

Where NCC is defined as:

$$NCC(I_1, I_2) = \frac{\sum_{x \in I} (I_1(x) - \bar{I}_1)(I_2(x) - \bar{I}_2)}{\sigma(I_1)\sigma(I_2)} \quad (4.14)$$

$$= \frac{\sum_{x \in I} (I_1(x))(I_2(x))}{\sqrt{\sum_{x \in I} I_1(x)^2} \cdot \sqrt{\sum_{x \in I} I_2(x)^2}}. \quad (4.15)$$

Here, σ is the standard deviation and \bar{I} the mean pixel intensity value of an image I . A pixel of the image I is given by x . The expected value of a gradient image is always 0, which speeds up the computation of NCC and helps to increase the performance of the similarity measure evaluation.

Normalized Gradient Fields

The regularized normalized gradient fields (NGF) similarity measure [Mode 03, Habe 06], which is based on image gradient directions and magnitudes, was also found very suitable for the TEE probe registration. The following definition of the measure is used here:

$$NGF(I_1, I_2) = \frac{1}{2} \sum_{x \in I} \langle n_\epsilon(I_1, x), n_\epsilon(I_2, x) \rangle^2, \quad (4.16)$$

which evaluates the dot product between all gradients in the X-ray image (I_1) and the DRR image (I_2). The gradient n_ϵ of a pixel x from an image I is calculated as:

$$n_\epsilon(I, x) = \frac{\nabla I(x)}{\sqrt{\|\nabla I(x)\| + \epsilon^2}}, \quad (4.17)$$

where ϵ is the regularization condition to suppress gradients that are resulting from image noise. For the X-ray image, ϵ was set to the mean value over all image gradients and $\epsilon = 0$ for the DRR because there is no noise in the DRR.

4.4.3 Image Mask

The similarity measures described above were additionally amplified at specific structures of the probe with the use of a special mask image. This is possible due to the known position of the additional added ball markers and holes in the TEE probe model, which are described in Section 4.2. The lighter parts in Figure 4.9 show the amplified marker structures in the DRR. It is applied to the original X-ray image as well. The masks help to focus on the additional markers and to achieve a higher accuracy during the registration.

4.5 Optimization Methods

In general, the goal of an optimizer is to find a minimum, respectively maximum, of a given cost function. In case of 2D-3D registration, its goal is to find the best matching



Figure 4.9: Example of an image mask. The lighter parts show amplified structures. Some markers can only be seen partly or are hidden completely.

parameter set which is represented by the minimum of the used similarity measure. Another important task of an optimizer is to reduce the number of evaluations that are needed for finding a minimum. A lower number of similarity measure evaluations will result in a faster runtime. This is even more important for 2D-3D registration, because each evaluation step requires the generation of a new DRR.

Many optimizers are known in literature [Flan 92] for different stated optimization problems. The parameter space can be linear or non-linear, bounded or not bounded and one can introduce different constraints which are limiting the search space. The specific task of 2D-3D registration can be stated as a non-linear optimization problem. Due to the projective geometry, there is no linear relationship between the six degrees of freedom. It can also be seen as a bounded and constrained problem, because of the known range of valid parameters.

Non-linear optimizers can be grouped to local or global methods. Local optimization methods are showing a good performance on well-posed (quasi-convex) functions [Main 98]. However, they are prone to local maxima or minima. They can miss the global optimum while getting stuck in local optima. This can happen easily on noisy cost functions with many local extrema. On the other hand, global optimization methods are more robust to such rough functions. The main disadvantage here is that they are usually slower than local optimizers. However, there is no global method known which certainly finds the exact maximum.

An additional important characteristic for local search methods is whether they are using gradient information or not. Usually, gradient-based optimizers are faster than optimizers which are not taking gradients into account. The use of gradients (1st derivative) or Hessian matrices (2nd derivative) can increase the performance of an algorithm because they are reducing the amount of expensive cost function evaluations and improving the convergence. This won't be applicable anymore if the complexity of the gradient calculation is excessively high. Usually, the derivation of a similarity measure used for 2D-3D registration can not be determined analytically. Therefore, the gradient must be approximated with additional function evaluations, which is expensive because of additional DRR generations. However, gradient-based

Algorithm 4.1 Powell-Brent optimizer.

Data: Initial starting params S , initial search directions D , similarity measure sm

while *break condition not reached* **do**

Find minimum for all D ($linmin(D)$)

if $sm(S) \leq break\ condition$ **then**

| Break

end

$S =$ linear combination of locally found minima (min_i)

$d \in D$ with the best minimum is replaced with the newly calculated d

Rearrange all other $d \in D$ to search from S to particular min_i

end

methods can find the optimum with a relatively small number of iterations when they are initialized with appropriate starting parameters [Flet 13], for example the starting position could be chosen close to a global optimum.

In this work, the Powell-Brent [Bren 73] and the Subplex [Rowa 90] algorithms were found to be most promising based on initial investigations. A comparable survey with different optimization algorithms for the task of TEE probe registration was carried out in [Kais 14b]. The best registration results were achieved by the global optimizer CMA-ES [Hans 06], which was used in 2D-3D registration based applications before [Gong 08]. Nevertheless, the runtime of this optimizer is too slow to employ it for a real time environment.

4.5.1 Powell-Brent

Powell's Direction Set method [Flan 92] is a local optimizer without the use of gradient information. It was successfully used before for the task of TEE probe registration in [Gao 12]. The original Powell's method tries to determine the best search direction in an n -dimensional space by reducing the n -dimensional optimization problem into multiple one-dimensional problems. These linear line searches are performed with Brent's method [Bren 73]. In case of 2D-3D registration one has to evaluate six 1D searches in each iteration.

In principal, Powell's method is working like presented in Algorithm 4.1. Figure 4.10 shows an exemplary iteration. In accordance to Powell, the starting search directions D are the normal vectors of the parameter space. While identifying the new search directions, it must be ensured that they do not interfere with maxima found earlier. Therefore, the old search vector is replaced by the new displacement vector and the other vectors are shifted to the new position. An advantage of this algorithm is that it is derivative-free, which makes it faster in terms of 2D-3D registration and more robust to complex cost functions.

For the experiments in this thesis the algorithm implementation of [VXL] was used.

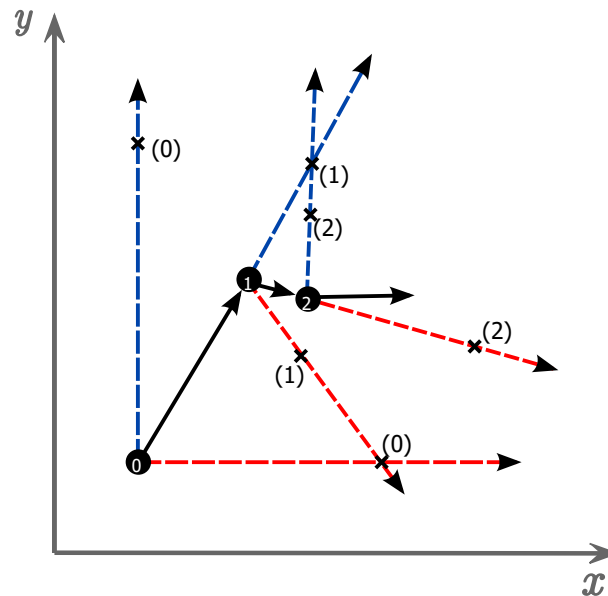


Figure 4.10: Basic principle of Powell's method. Red and blue lines are independent search directions, x denotes a local optimum. Black lines are the new search directions which replaces the best last one. The numbers indicate the iteration step of the algorithm.

4.5.2 Subplex

The subplex algorithm by [Rowa 90] is an improvement of the popular Nelder-Mead or Downhill-Simplex optimization algorithm [Neld 65]. The Nelder-Mead method is a non-linear and gradient-free optimization approach. It is based on an $N + 1$ simplex that is spanned in an N -dimensional search space where N is the number of parameters. The idea behind the method is that the points of the simplex are moving closer to the optimum of the cost function and the simplex is collapsing around the searched minimum after multiple iterations. Each point of the simplex is a set of N parameters for that a similarity measure function value is calculated. In each iteration, the point with the worst result is exchanged with another set of parameters which is chosen by reflection around the center of all other points in the simplex. Based on the function values, the simplex is expanding, contracting or shrinking after each iteration until a stop criterion is reached. The types of possible simplex moves are shown in Figure 4.11.

It is reported that the algorithm is robust but not the best in convergence performance. However, it can be shown that it fails for some functions completely. A more robust and more efficient version of the Simplex method introduced by the Subplex algorithm. This method is working on sequence of subspaces. The algorithm was used in the implementation of [John 10b].

4.6 Optimization Strategy

A good optimization strategy is useful to improve the performance and the quality of a registration. The most commonly employed techniques are multi-resolution and

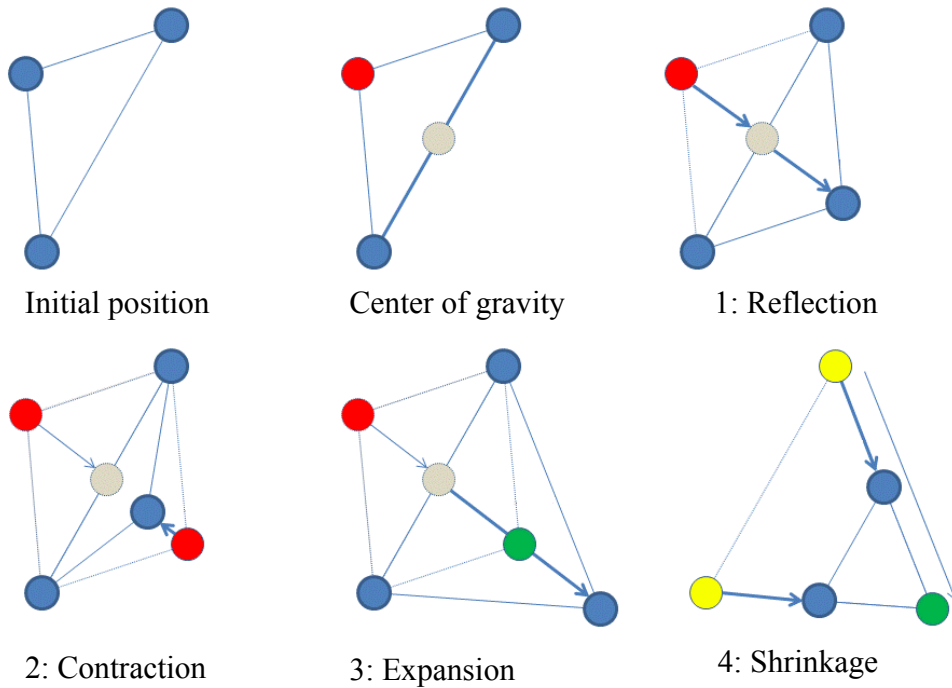


Figure 4.11: All types of possible simplex movements (exemplary for a parameter space of $N = 2$). Original image from [Caps].

multi-scale approaches [Thev95]. These techniques are used in this work as well. Multi-resolution algorithms rescale the provided reference images to a (usually) lower resolution. Because the performance of the generation of DRRs and the similarity measure evaluation is directly related with the number of pixels, the multi-scale technique will have a direct impact on the runtime performance. Multi-scale methods preprocess the given images, usually with a smoothing Gaussian filter of varying size. This has the advantage that noise is reduced and other disturbing structures are filtered. In general, both methods are used simultaneously. Another approach is to utilize different similarity measures or to change the optimized parameters or parameter constraints, depending on the current resolution or registration step.

The strategy which is used here is based on an image pyramid [Adel84] and is shown in Figure 4.12. Assuming an image with the resolution of 1024×1024 pixels, the first step is to rescale it to a size of $\frac{1}{8}$ (128×128) with simultaneous Gaussian smoothing. A fast intensity-based similarity measure (SSD) is employed in this first step. Only inplane parameters are optimized to find a suitable starting position for more accurate registrations. In consequence to the faster computation of DRRs and the faster similarity measure evaluation on lower resolutions, the search space can be extended without huge loss of performance.

An advantage of this method is, that the boundary constraints for the search space can be adapted to a more and more smaller range over the next steps. A more complex similarity measure is used and more parameters are accounted for optimization. The search range is going to be decreased in each step and the number of optimized parameters is increased. This is similarly to [Kais13b].

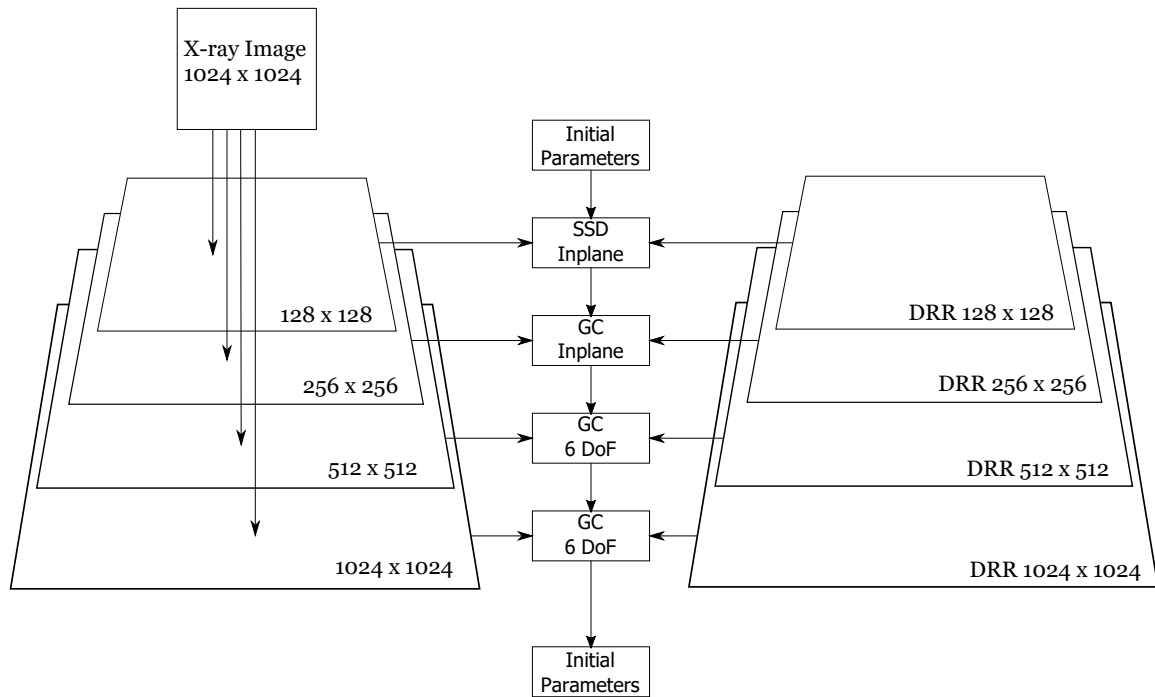


Figure 4.12: Optimization strategy for TEE probe registration.

4.7 Quality and Performance Criteria

There are several parameters of a registration/detection algorithm which can be used as a benchmark for the algorithm performance. In this thesis, the accuracy of registration, the performance of the overall registration per frame and the robustness against outliers or initial starting parameters are used.

Algorithm robustness describes how well an algorithm behaves if noise or different structures are disturbing the image. Image noise or artifacts (originating from insufficient gray value contrast) can force an algorithm to fail. Different structures, for example other catheters, could be accidentally recognized as the TEE probe. This is called false-positive detection.

The performance of an image registration algorithm basically rates the runtime of the registration for a single frame or, in case of tracking, the possibly tracked frames per second.

The accuracy indicates how close the algorithm registers the 3D model to a ground truth position. [Kraa 05] describes the error measures that are usually used to express and to measure the accuracy of a given registration (see Figure 4.13). These measures are used in this thesis as well.

4.7.1 Target Registration Error

The target registration error (TRE) is widely used for evaluating the 3D error of an image registration. It calculates the Euclidean distance between predefined 3D target points from a ground truth position and their associated 3D points after registration.

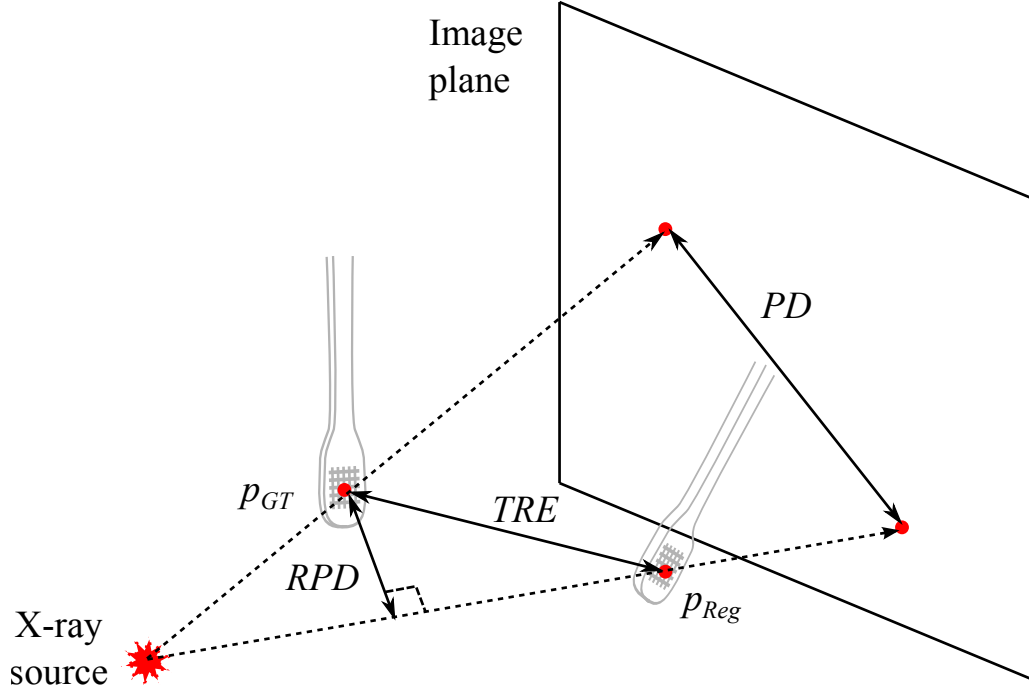


Figure 4.13: Visualization of used error measures. Figure similar to [Kraa05].

Usually, the distance of more than one point is determined. Therefore, the mean of all target registration errors (mTRE) is calculated as:

$$mTRE(P_{GT}, P_{Reg}) = \frac{1}{k} \sum_{i=1}^k \|p_{Reg_i} - p_{GT_i}\| \quad (4.18)$$

P_{GT} is a set of points at ground truth position, and P_{Reg} are the associated points after registration. The size of the set is given by k . This measure represents the real registration error in the 3D space.

4.7.2 Projection Distance

The projection distance (PD) is the projected 2D error between points on the image plane. The mean projection distance is given by:

$$mPD(P_{GT}, P_{Reg}) = \frac{1}{k} \sum_{i=1}^k \|\mathcal{P} \cdot p_{Reg_i} - \mathcal{P} \cdot p_{GT_i}\| \quad (4.19)$$

The distance between two projected points is measured on the 2D image plane. For mPD, the ground truth points and the registered points are projected to the image plane. mPD is better suited for 2D-3D registration than mTRE if the registered object is only viewed from one perspective. It respects the circumstance that the registration error in out-of-plane directions has less visual influence to the user than the error in inplane direction. It measures the real recognizable error on the image. Due to the projective geometry, mPD is dependent on the distance of the object from the X-ray source to the detector and the screen resolution.

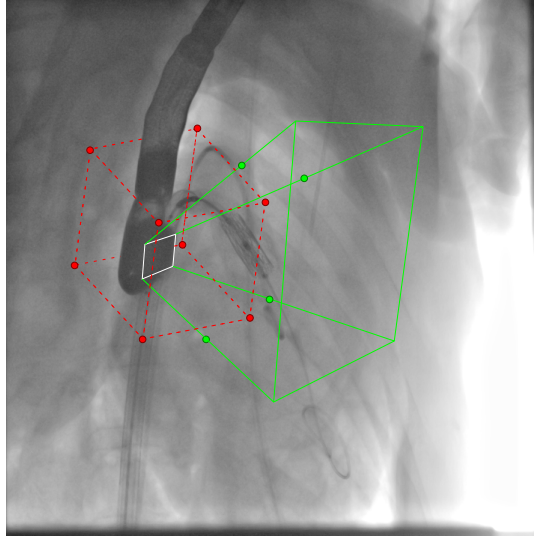


Figure 4.14: Positions where the errors are measured. Red dots indicate error points for the TEE probe, green dots for the Ultrasound cone and image.

4.7.3 Reprojection Distance

The RPD error measure overcomes the shortcomings of PD that the error is depended on the distance to the projection plane. It is defined as:

$$mRPD(P_{GT}, P_{Reg}) = \frac{1}{k} \sum_{i=1}^k D(L_i(source, p_{Reg_i}), p_{GTt_i}) \quad (4.20)$$

The reprojection distance of a registered point p_{Reg} is the shortest distance between a line L_i and its 3D ground truth position p_{GT} . The line is drawn from the 3D position of the X-ray source through the 3D position of the registered point p_{Reg} in direction of the image plane. This line can be seen as the ray which projects p_{Reg} onto the image plane. This gives the shortest way between the registered and the ground truth point, perpendicular to the image plane. mRPD is independent of the distance to the projection plane and can be seen as a normalized mPD.

4.7.4 Error Markers

In this thesis, the error is measured at 8 virtual corner points of a bounding box around the TEE probe volume which are 50 mm away from the volume center. This shows the registration error of the TEE probe. To examine a more user relevant error, 4 error markers at the Ultrasound cone are additionally evaluated. These 4 markers span a virtual plane which is 50 mm away from Ultrasound array. This gives are more user related error, because the user is only interested in the accuracy of the registration of the Ultrasound image to the X-ray image. Due to the projection geometry of the X-ray image, this error is very dependent on the view direction of the TEE probe. Parallel views on the Ultrasound cone will cause larger errors than perpendicular views.

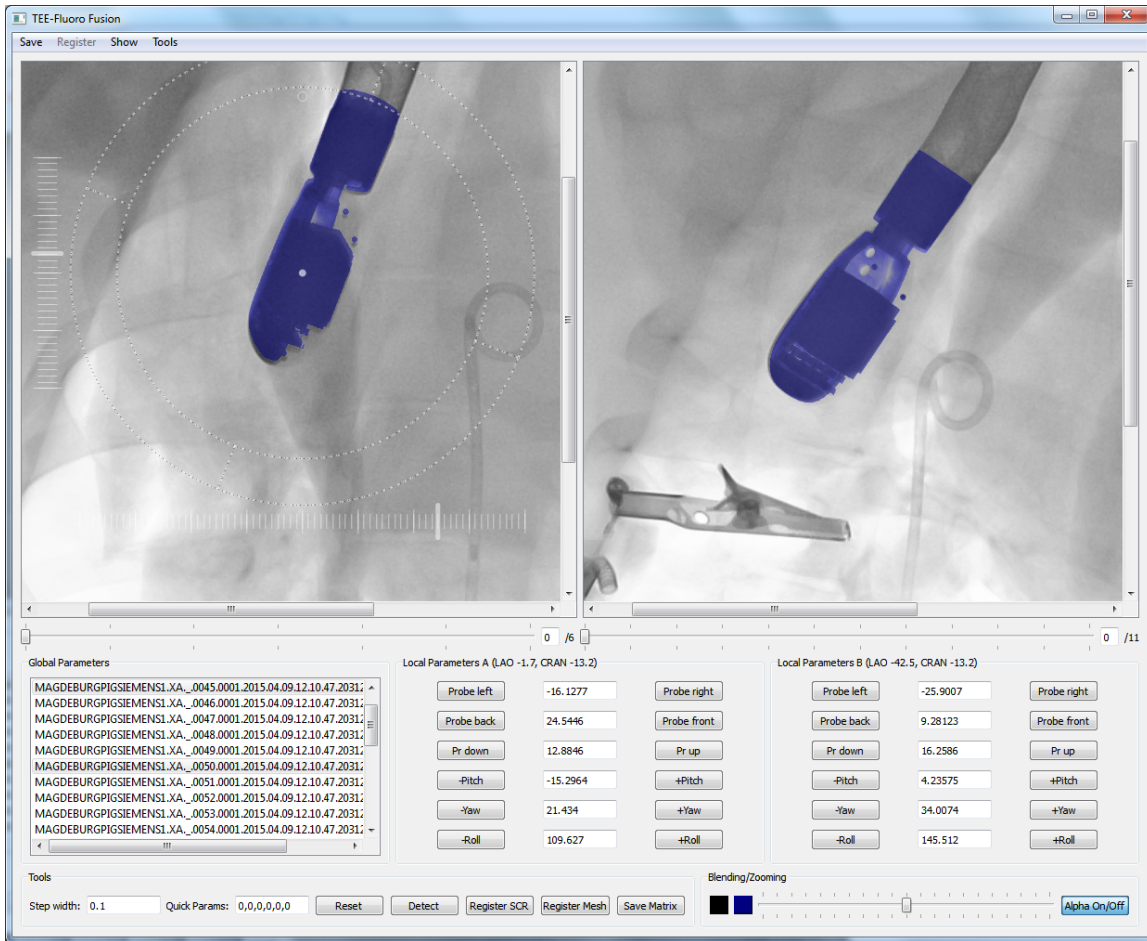


Figure 4.15: Screenshot of the annotation tool for generating a ground truth registration of TEE probe poses. Here, a probe can be manually registered on two X-ray images from two different views at the same time.

4.8 Ground Truth Generation

Although a lot of research has been done in the area of TEE probe registration, there are still open issues. One enduring problem is to find a reliable ground truth position of the TEE probe to evaluate whether the registration and detection algorithms are working correct and accurate. Basically, two methods of establishing a valid ground truth for the used data have been utilized.

One approach is to carry out a manual 2D-3D registration of the TEE probe. This method, which is often the only possibility, is biased by the user and requires a huge amount of time and experience. The topic was addressed in [Kais14c] and is described in detail in Section 5. Here, two images from different view angles were used to eliminate the uncertainty of the out-of-plane parameters. A separate tool was developed for this thesis to establish ground truth data based on that method. Figure 4.15 shows a screenshot of it.

Another approach is to acquire a 3D C-arm CT of the whole experimental setup and to perform a 3D-3D registration of the TEE probe model to the recorded 3D volume afterwards. This method was evaluated in [Kais14d].

Both approaches are error-prone if there is patient or object motion between the recording of the two images or between the 3D scan and the following X-ray acquisitions. The only way to generate data without motion is during a phantom or cadaver study. Motion can not be avoided in clinical data from animal experiments or human cases. Therefore, such a ground truth is inaccurate.

Another source of error is the miscalibration of the used C-arms. Assuming that one can establish a perfect registration of the object for one X-ray image. If the C-arm is rotating to another angulation, it is not sure that the registration still matches the position perfectly. The reason for this effect is that a projection geometry of a C-arm depends on many parameters which can not be perfectly measured. A 2D-3D registration algorithm needs to know the actual projection geometry of the X-ray system consisting of tube and detector position. The straightforward approach is to assume an ideal C-arm geometry and to compute the projection matrix analytically. This does not take into account hardware deformations and out-of-circle rotations. Alternatively, one can perform offline geometry calibrations on various C-arm positions and compute interpolated projection matrices at any other position.

An experiment was carried out in [Kais 14d] to show the importance of calibrated projection matrices. A TEE probe was fixed in a box with 24 attached metal balls at the outside, like in [Hatt 14]. Additionally, the box has been put into a thorax phantom to generate in-vivo-like images. Figure 4.16 shows the described setup under X-ray from two different angulations. Multiple X-ray images were acquired from several angulations within a range of LAO/RAO $[90, -90]$ and CRAN/CAUD $[30, -30]$. Then a registration of the volume was manually established with the use of analytical matrices on two X-ray images from almost orthogonal angulations. The overlay error of all metal balls was measured under this registration for all other angulations using analytical projection matrices. The same process was repeated while using calibrated projection matrices for registration and overlay projections.

The results are shown in Figure 4.17. The uncalibrated matrices showed an average error of 4.09 mm. However, the experiments with calibrated matrices showed only an average error of 0.73 mm. While 2D/3D registration finds a suitable 3D position for the given 2D images, the question is whether ultrasound structures are still correctly overlaid on X-ray if the user rotates the C-arm to another angulation, which was not used for registration, particularly when using the simpler analytical projection matrices. This source of error varies from system to system and must not be ignored. It is described in Section 5.3 how it can be handled if calibrated projection matrices are not available.

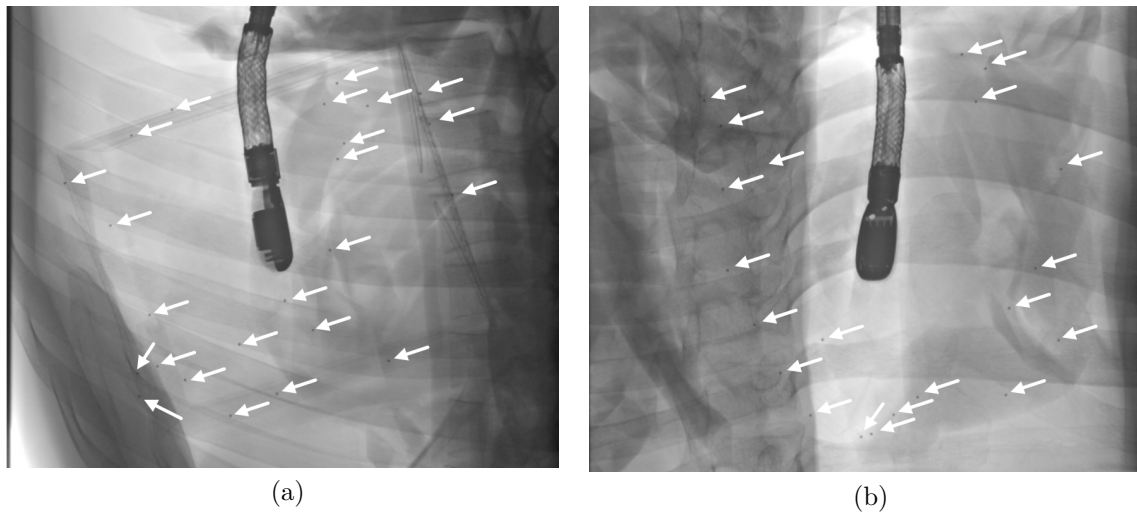


Figure 4.16: Exemplary X-ray images with the TEE probe fixed in a box with 1mm diameter metal ball markers, indicated by the white arrows.

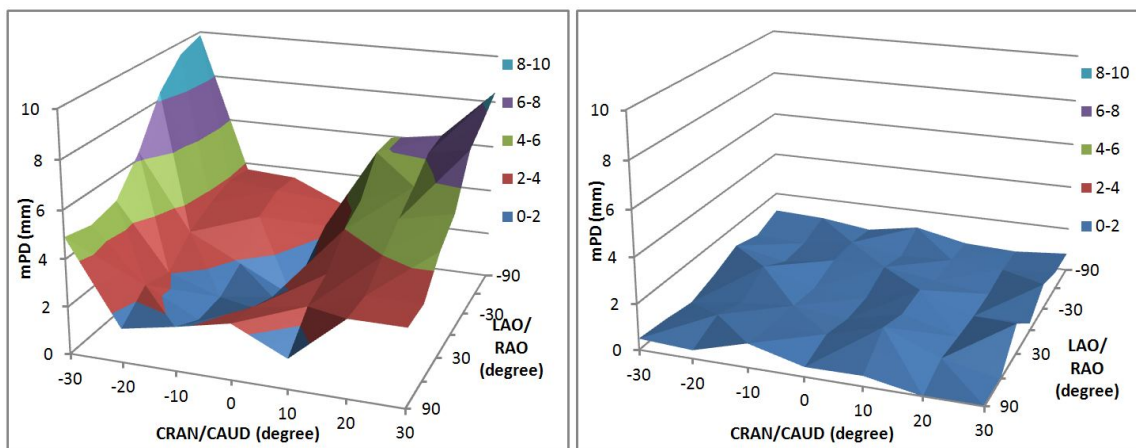


Figure 4.17: Comparison of the accuracy of overlaid marker points. Left with analytical projection matrices, right with calibrated matrices. The error is measure in terms of mPD.

2D-3D Registration with Planar Parameters

5.1 Motivation	49
5.2 Methods	53
5.3 Objection Motion and Calibration Errors	58
5.4 Experiments & Results	58
5.5 Discussion & Conclusion	63

2D-3D registration in medical imaging can be applied in many different cases. Monoplane registration is the most straightforward use case which means registering the object on only one reference image. A common issue of this type of algorithms is that out-of-plane parameters are hard to determine, which is described in Section 4.1. One solution to overcome this issue is the use of X-ray images from two angulations. However, performing inplane transformations in one image destroys the registration in the other image, particularly if the angulations are smaller than 90 degrees apart. Besides automatic 2D-3D registration, the manual registration is commonly needed. Practically, most 2D-3D registrations for organ-to-organ applications during interventions are done manually. Other examples are manual correction, in case the automatic solution fails, as well as to establish a ground truth transformation for testing data sets. Manual 2D-3D registration is often the best possible way of acquiring a suitable ground truth transformation.

The technique of planar parameters is introduced in this chapter. It helps to improve the registration performance of mono- and biplane as well as during manual or automatic registration. It handles translation and rotation of a volume in a way that inplane parameters are kept invariant and independent of the angle offset between both projections in a double-oblique setting. Parts of this chapter have been published in [Kais 14c] and [Kais 14a].

5.1 Motivation

This chapter splits into two parts. One part are the observations of side effects made during monoplane registration and how to fix those issues with planar parameters. The second part shows how these technique can help during multiplane registration. This technique is independent of manual or automatic 2D-3D registration.

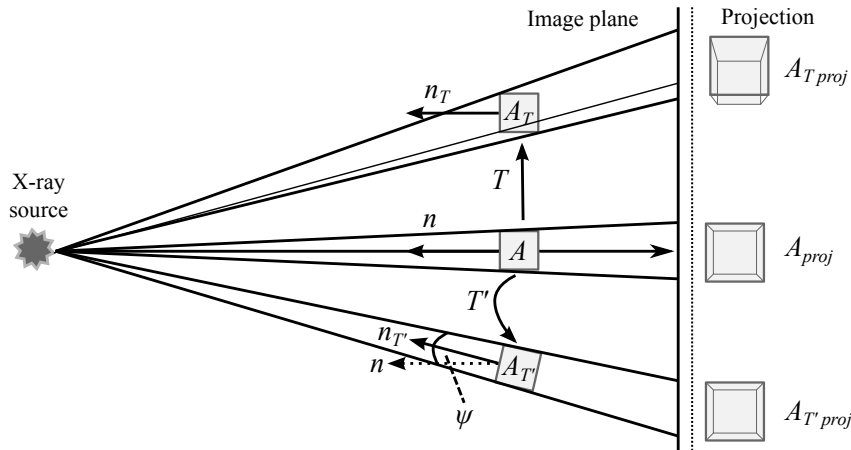


Figure 5.1: Illustration of the rotation angles observer problem while translating an object under projective geometry.

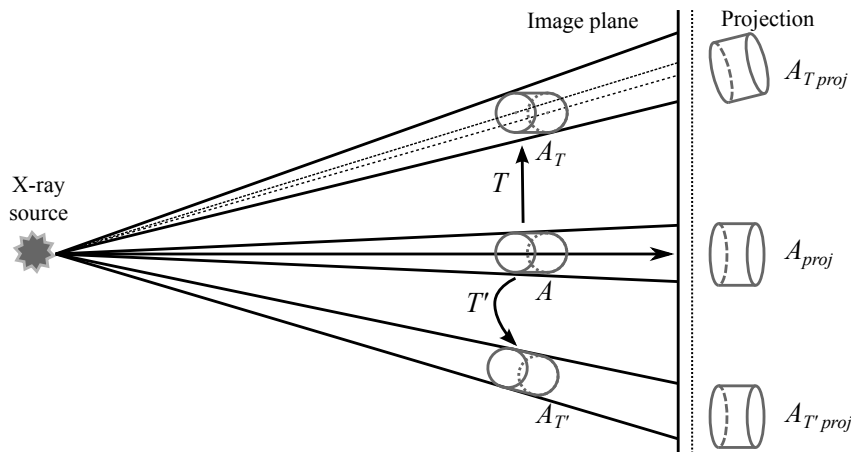


Figure 5.2: Illustration of the problem of the observed yaw rotation while translating a cylindrical object which is rotated around the pitch.

Due to the projective geometry of a C-arm system, several issues occur during monoplane and biplane 2D-3D registrations. If an object is shifted parallel to the image plane (without changing the common 3D rotational parameters), the user can observe a rotation of the projected object in the 2D image. This change depends on the distance from the object to the central beam. In Figure 5.1, object A is translated with the transformation T in 3D space parallel to the image plane which results in a new object position A_T . Although the model was not rotated, the observer of the projections of the objects A_{proj} and $A_{T_{proj}}$ has the impression of a changed set of rotational angles (θ_{pitch} , θ_{roll}). This results in errors ψ of up to 9 degrees, depending on the projection geometry of the C-arm. Similar errors occur to θ_{yaw} in the image while translating the object in case θ_{pitch} is not exactly 0. The impression is that θ_{yaw} is changing and the probe is performing an inplane rotation the more the probe is moved away from the image center. This is illustrated in Figure 5.2.

Such effects can have a huge influence on the registration quality and the usability of a 2D-3D registration system, especially during biplane registration. It is also im-

portant while combining a 2D-3D registration with a detection algorithm that works independent of a concrete projection geometry. Such a combination is presented in Chapter 7. Position-independent parameters are necessary for the correct conversion of the estimated parameters, which are detected in the 2D image.

Due to the projective characteristic of a C-arm system, the six spatial parameters of the TEE probe model S can be separated into inplane and out-of-plane parameters, like described in Chapter 4.

Inplane parameters (t_x, t_z, θ_{yaw}) can cause a significant image change and are easier to estimate. Changes in out-of-plane parameters like depth (t_y) or pitch (θ_{pitch}) and roll (θ_{roll}) cause an object shift perpendicular to the image plane, which is more difficult to identify. This is explained in detail in Section 4.1. Therefore, it can be helpful to register an object from multiple view directions. In a common biplane setup, the detector planes have a rotational offset of 90 degrees. Therefore, inplane parameters of the first image become out-of-plane parameters in the second image and vice versa. Only one rotational parameter will always remain out-of-plane. Typically, there are two ways of registering multiplane images.

1. Full 3D: all six spatial parameters are registered simultaneously along the object axes like in [Gao 12]. It will not be distinguished between inplane and out-of-plane parameters.
2. Subdivided inplane: The decoupling of in- and out-of-plane parameters can be of major importance, particularly when registering with image data from multiplane systems. The objects' inplane parameters are registered alternately between both imaging planes. One can dramatically increase accuracy and capture range while registering only the inplane parameters for each plane [Bros 12, Miao 13b].

No biplane C-arm system was used in this work, but the images from a monoplane system were acquired consecutively from two angulations. The TEE probe is usually in a fixed position for longer periods during the interventions. Therefore, performing imaging from a second angulation is a reasonable workflow, in particular for small angle offsets. Due to space constraints in hybrid operating rooms and catheter labs, orthogonal multiplane imaging can be difficult to achieve. This leads to projection angle differences smaller than 90 degrees. Referring to the C-arm angle definition of Section 2.1, the used double-oblique C-arm setup is specified as

$$\forall \alpha, \gamma : |\alpha_A - \alpha_B| \leq 90^\circ \wedge |\gamma_A - \gamma_B| \leq 90^\circ. \quad (5.1)$$

A possible intuitive biplane registration process is shown in Algorithm 5.1.

The drawback of a non-orthogonal setting, where both views are displaced less or more than 90 degrees, is that changes of translation and rotation in plane B destroy the recent registration of plane A and vice versa. This ends up in an iterative process until both positions are converging (see Figure 5.3a). In general, that behavior belongs to all parameters, not only to the depth, which is exemplary shown in the figure.

Both issues stated above are resolved with an improved approach which is introduced in the next section. All parameters are immutable during registration of monoplane images except the one that is explicitly changed.

Algorithm 5.1 General biplane registration approach.

while *similarity measure stop criterion is not reached* **do**

 Register on image A

 Transfer registration matrix to plane B

 Register on image B

 Transfer registration matrix to plane A

end

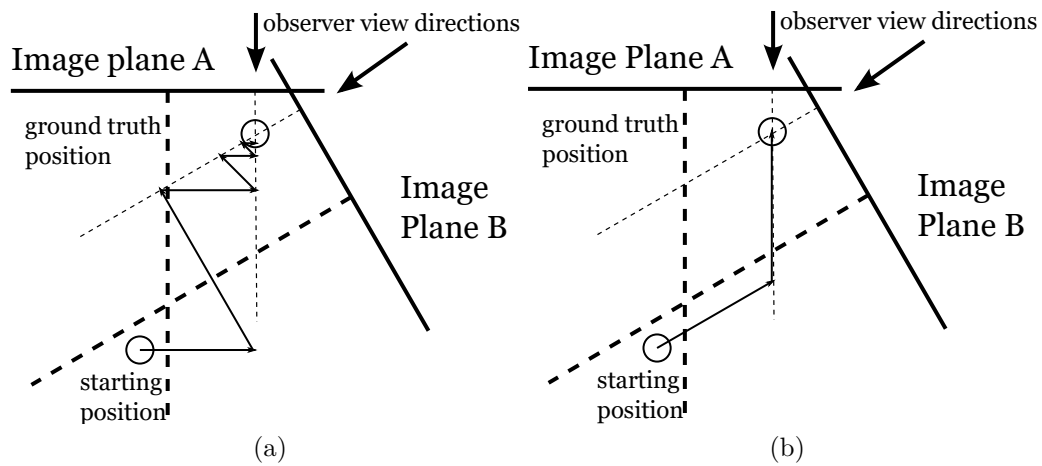


Figure 5.3: (a) illustrates the inplane approach and (b) the planar approach of registering an object on two reference images.

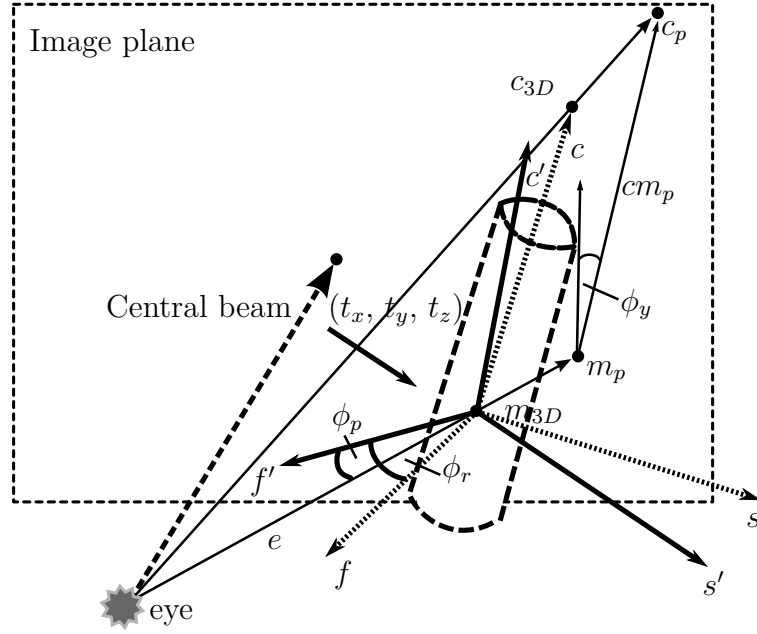


Figure 5.4: Definition of planar parameters.

This approach keeps inplane parameters invariant to the registration on the other image plane and establishes a one-step movement like illustrated in Figure 5.3b. The main idea is to transform the 3D object without disrupting previous inplane registration results. For each view, only inplane parameters t_x , t_z , θ_{yaw} are changed, while out-of-plane information is used from the other plane.

5.2 Methods

It is defined that an object's rotational parameters are relative to the projection image plane. The initial position is achieved if all angles are set to zero and the object is positioned in the central projection ray. The coordinate axes and transformation angles are defined as follows:

- The x -axis t_x is defined as the left and right direction in the image.
- The z -axis t_z is defined as the up and down direction in the image.
- The y -axis t_y is perpendicular to the image plane, which is indeed the depth direction.
- The *roll* angle θ_{roll} is the rotation around the centerline of the object. The center line must be defined, but usually it exists a natural one for each object.
- The *pitch* θ_{pitch} is the tilting of the object relative to the image plane.
- The *yaw* θ_{yaw} is the rotation parallel to the image plane.

An illustration is shown in Figure 4.1. The corresponding registration matrix \mathcal{R} of an object is compounded by the three different rotation matrices $R_{\theta_{yaw}}$, $R_{\theta_{pitch}}$, $R_{\theta_{roll}}$ and the translation matrix $T_{translation}$ by

$$\mathcal{R} = T_{translation} \cdot R_{\theta_{yaw}} \cdot R_{\theta_{pitch}} \cdot R_{\theta_{roll}}. \quad (5.2)$$

As mentioned before, the C-arm is able to rotate along the two different angulations, like it is defined in Equation 4.4. Therefore, one can show an object from different views. A local registration matrix \mathcal{R}_1 is defined as the matrix which fulfills the previously described transformation axes under a specific C-arm rotation \mathcal{C}_1 . Such a local matrix can be converted to a global registration matrix by:

$$\mathcal{R} = \mathcal{C}_1^{-1} \cdot \mathcal{R}_1. \quad (5.3)$$

R is a representation of the registration relative to the patient table. Therefore, it is independent of the C-arm angulation. The corresponding local transformation matrix \mathcal{R}_2 for another C-arm rotation \mathcal{C}_2 can be computed by:

$$\mathcal{R}_2 = \mathcal{C}_2 \cdot \mathcal{R}. \quad (5.4)$$

The terms planar and spatial parameters are introduced in the following. Spatial rotations $\{\theta_{yaw}, \theta_{pitch}, \theta_{roll}\}$ rotate around the axes aligned with the projection image plane and are independent of the translational position of the object. In contrast to spatial parameters, planar parameters $\{\phi_{yaw}, \phi_{pitch}, \phi_{roll}\}$ are defined as the rotational angles observed by the user in the projected image. By definition, planar parameters remain unchanged if the object is translated or rotated – except for the modified parameter. This is represented by $A_{T'}$ and its transformation T' in Figure 5.1 and Figure 5.2.

5.2.1 Planar Parameters for Monoplane Projection

Planar parameters are defined first in the monoplane case which is required for understanding the parameters in a biplane setup. The planar parameters for the monoplane case are visualized in Figure 5.4.

Converting Spatial to Planar Parameters

Giving a set of all six 3D spatial parameters $S = \{t_x, t_y, t_z, \theta_{yaw}, \theta_{pitch}, \theta_{roll}\}$ and a projection matrix \mathcal{P} , one can compute their planar parameters $\{\phi_{yaw}, \phi_{pitch}, \phi_{roll}\}$. Planar angles are dependent on the vector e , pointing from *eye*, the focal point of the projection geometry, to the rotation center m_{3D} of the object. The object's base vectors c , s , f , which build the objects rotation matrix, must be adapted to the view direction e . By knowing the object's centerline vector c , an orthogonal system is established which is related to e with:

$$s' = c \times e \quad (5.5)$$

$$f' = s' \times c \quad (5.6)$$

$$c' = s' \times e. \quad (5.7)$$

According to the view direction e , the planar rotation angle ϕ_{pitch} is computed with the dot product of f' and e , respectively c' depending on the quadrant:

$$\phi_{pitch} = \begin{cases} +\cos^{-1}(f' \circ e) & : \cos^{-1}(f' \circ c') - \frac{\pi}{2} < 0 \\ -\cos^{-1}(f' \circ e) & : \cos^{-1}(f' \circ c') - \frac{\pi}{2} \geq 0 \end{cases}. \quad (5.8)$$

The calculation of ϕ_{roll} can done equivalently:

$$\phi_{roll} = \begin{cases} +\cos^{-1}(f' \circ f) & : \cos^{-1}(f' \circ s) - \frac{\pi}{2} < 0 \\ -\cos^{-1}(f' \circ f) & : \cos^{-1}(f' \circ s) - \frac{\pi}{2} \geq 0 \end{cases}. \quad (5.9)$$

The inplane yaw angle is directly computed on the 2D image plane with the use of the projection $cm_{\mathcal{P}}$ of the center line vector c . This vector is given by the direction between two projected points on the image plane with

$$cm_{\mathcal{P}} = \mathcal{P} \cdot c_{3D} - \mathcal{P} \cdot m_{3D}. \quad (5.10)$$

The first point m_{3D} is the center of the object, the second point c_{3D} is a point along the object's center line in up direction. The yaw angle is than calculated as

$$\phi_{yaw} = \begin{cases} +\cos^{-1}(cm_{\mathcal{P}}^y) & : \cos^{-1}(cm_{\mathcal{P}}^x) - \frac{\pi}{2} < 0 \\ -\cos^{-1}(cm_{\mathcal{P}}^y) & : \cos^{-1}(cm_{\mathcal{P}}^x) - \frac{\pi}{2} \geq 0 \end{cases}. \quad (5.11)$$

Here, $cm_{\mathcal{P}}^x$ means the x component and $cm_{\mathcal{P}}^y$ the y component of the 2D vector $cm_{\mathcal{P}}$ which is equivalent to the \circ product of $cm_{\mathcal{P}}$ with and the unit vector $[1, 0]$, respectively $[0, 1]$.

Converting Planar to Spatial Parameters

Giving a set of three translation parameters and the three planar rotational parameters $S = \{t_x, t_y, t_z, \phi_{yaw}, \phi_{pitch}, \phi_{roll}\}$ and a projection matrix \mathcal{P} , one can compute the object's 3D transformation matrix T_{3D} as:

$$T_{3D} = T_{translation} \cdot R_{\phi_{yaw}} \cdot R_{\phi_{pitch}} \cdot R_{\phi_{roll}} \quad (5.12)$$

where $R_{\phi_{pitch}}$ and $R_{\phi_{roll}}$ are rotation matrices built from their appropriate Euler angles. $R_{\phi_{yaw}}$ is more difficult to compute because it depends on both preceding matrices. To ensure that the planar yaw is used, this is determined based on the 2D image plane which is the direction vector $cm_{\mathcal{P}}$ pointing from $m_{\mathcal{P}}$ to $c_{\mathcal{P}}$. The 2D point $c_{\mathcal{P}}$ can be calculated by a 2D yaw rotation:

$$c_{\mathcal{P}} = m_{\mathcal{P}} + [\sin(\phi_{yaw}), 0, \cos(\phi_{yaw})], \quad (5.13)$$

while $m_{\mathcal{P}}$ is the projected object center point and $c_{\mathcal{P}}$ the projected object point in center line direction with applied planar yaw rotation ϕ_{yaw} . The matrix $R_{\phi_{yaw}}$ can be composed with the base vectors s, f, c :

$$R_{\phi_{yaw}} = \begin{pmatrix} s_x & f_x & c_x & 0 \\ s_y & f_y & c_y & 0 \\ s_z & f_z & c_z & 0 \\ 0 & 0 & 0 & 1 \end{pmatrix} \quad (5.14)$$

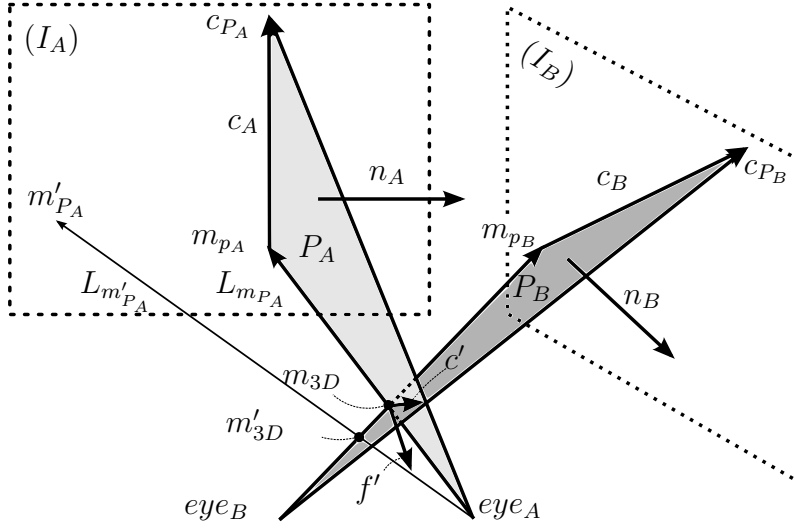


Figure 5.5: Schema for multiplane transformation.

while the base vectors are computed as:

$$f = m_{\mathcal{P}} - eye \quad (5.15)$$

$$s = (c_{\mathcal{P}} - eye) \times f \quad (5.16)$$

$$c = s \times f. \quad (5.17)$$

One has to note that *eye* is a 3D point and means the focal point of the projection geometry. To enable the calculation of the base vectors, one has to extend the dimension of the two 2D points $m_{\mathcal{P}}$ and $c_{\mathcal{P}}$ by their depth component. This component is implicitly known, because it is the distance to the detector plane.

5.2.2 Planar Parameters for Biplane Registration

It is now described how one can achieve a behavior like described in Figure 5.3b and to avoid the case of Figure 5.3a. The approach is object-centerline-driven, which initially lies in the cranial-caudal direction, and uses the concepts defined in Section 5.2.1. Therefore, the rotation ϕ_{roll} around the centerline c remains out-of-plane from both views. Aligning the other parameters correctly along the centerline will reduce the search space for ϕ_{roll} .

The biplane setup consists of two image planes I_A and I_B which are the detector planes of the C-arm in two different views. This is illustrated in Figure 5.5. The rotation center of the TEE probe is represented by m_{3D} and the centerline by the vector c' . As mentioned in Section 5.1, the biplane strategy is to change only inplane parameters and not disturbing out-of-plane parameters. The translation of the TEE probe are implicitly given by the projected points m_{P_A} in plane A and m_{P_B} in plane B. The TEE probe's rotation angles ϕ_{pitch} and ϕ_{yaw} are implicitly given by the projections c_A and c_B of the centerline vector c' . The 2D points c_{P_A} and c_{P_B} are projections of a 3D point along the centerline. All object translations and rotations in one image are bound to the spanning plane of the other image, to ensure that no previously achieved results are destroyed. Considering I_A for example, every transformation is

restricted by the plane P_B spanned by the focus point eye_B and the centerline c . A transformation of the object is only possible within in this plane. P_B is defined by its normal vector n_B as

$$n_B = (eye_B - m_{p_B}) \times (eye_B - c_{p_B}). \quad (5.18)$$

If the object is moved on I_A from image coordinate m_{p_A} to a new one m'_{p_A} , the new 3D position m'_{3D} of the object is determined by plane-line-intersection of plane P_B and line $L_{m'_{p_A}}$. This line runs from the focal point eye_A to new position m'_{p_A} of the object on I_A . This ensures that the position of the object is changed for I_A , but is not influencing the independent translational inplane parameters in I_B .

For simplification, it is now assumed that the object is rotated for plane A. The calculation for plane B is equivalent. The vectors c_A and c_B are determining the inplane yaw. They are obtained directly in the 2D image plane while projecting the centerline vector c of the object onto the image plane. Every yaw rotation ϕ_{yaw} is carried out in 2D on the image plane. The point c_{p_A} can therefore be seen as the new observable yaw rotation. The yaw calculation is done by calculating the vector between the projected object center point m_{p_A} and the projected object point in center line direction c_{p_A} as

$$c_{p_A} = m_{p_A} + [\sin(\phi_{yaw}), 0, \cos(\phi_{yaw})]. \quad (5.19)$$

The center line vector c' is thus defined by the intersection of planes P_A and P_B , which ensures that the yaw in I_B stays fixed even when the yaw in I_A is changed. The angle ϕ_{pitch} can not be changed during the biplane registration, but is determined via n_B from I_B . The plane normal n_A determines the object's 3D yaw rotation.

These plane intersections establish an orthonormal system with the base vectors n_A , f' , c' which are given as

$$c' = n_B \times n_A \quad (5.20)$$

$$f' = c' \times n_A. \quad (5.21)$$

With this system, it is now possible to calculate the matrix $R_{\phi_{yaw}\phi_{pitch}}$ which covers the rotations ϕ_{yaw} and ϕ_{pitch} . Similarly to Equation 5.14, the matrix can be built as follows:

$$R_{\phi_{yaw}\phi_{pitch}} = \begin{pmatrix} n_{Ax} & f'_x & c'_x & 0 \\ n_{Ay} & f'_y & c'_y & 0 \\ n_{Az} & f'_z & c'_z & 0 \\ 0 & 0 & 0 & 1 \end{pmatrix}. \quad (5.22)$$

Finally, the rotation ϕ_{roll} around the centerline c' is given by the rotation matrix $R_{\phi_{roll}}$ which is build with the common Euler angle representation. The overall rotation matrix is then given by

$$R = R_{\phi_{yaw}\phi_{pitch}} \cdot R_{\phi_{roll}}. \quad (5.23)$$

It is possible to append the roll because it is independent on the other two rotations. The roll is rotated along the centerline c' which is the intersection between P_A and P_B . Therefore, it is equal in both images.

Algorithm 5.2 General registration approach for decoupled biplane registration.

Data: Global registration matrices \mathcal{R}_A , \mathcal{R}_B for images A and B, while at start of the algorithm $\mathcal{R}_A = \mathcal{R}_B$

while *stop criterion is not reached* **do**

\mathcal{R}_A =Registration result from registration on image A

$$\mathcal{R}_B = \begin{pmatrix} \mathcal{R}_A[1:3, 1:3] & t_{x_B} \\ & m'_{3D_y} \\ & t_{z_B} \\ 0 & 0 & 0 & 1 \end{pmatrix}$$

\mathcal{R}_B =Registration result from registration on image B

$$\mathcal{R}_A = \begin{pmatrix} \mathcal{R}_B[1:3, 1:3] & t_{x_A} \\ & m'_{3D_y} \\ & t_{z_A} \\ 0 & 0 & 0 & 1 \end{pmatrix}$$

end

5.3 Objection Motion and Calibration Errors

The presented approach can also be used to overcome the influences of slight object movement caused by breathing or heart motion. Usually, this motion results in wrong offsets between objects in the consecutively acquired X-ray images. Also uncalibrated C-arm projection matrices can cause differences between two views. This is described in detail in Section 4.8. It follows that one could not achieve a 3D position that correctly matches both 2D positions in the projection images.

To solve this issue, the translation of both views can be decoupled. This means that inplane translation parameters t_x and t_z of images A and B are registered independently. The depth t_y is still obtained from the intersection point m'_{3D} . The rotational parameters are still calculated as shown in Section 5.2.2, which means that ϕ_{yaw} , ϕ_{pitch} and ϕ_{roll} are equal in both images and are not handled independently. A general algorithm for the decoupled approach is shown in Algorithm 5.2.

This method is possible, because the data which was used for evaluation showed that the object motion mostly causes a translational error. The difference for the object's rotational parameters between two images A and B are not significant and have no big influence on a matching registration position.

5.4 Experiments & Results

The presented approach was evaluated during automatic registration as well as for manual registration.

5.4.1 Evaluation of Automatic Registration

The planar approach was evaluated on various multiplane X-ray sequences acquired within a porcine study and compared to the two conventional strategies, Inplane and Full-3D, which were presented in Section 5.1. The 2D-3D registration process

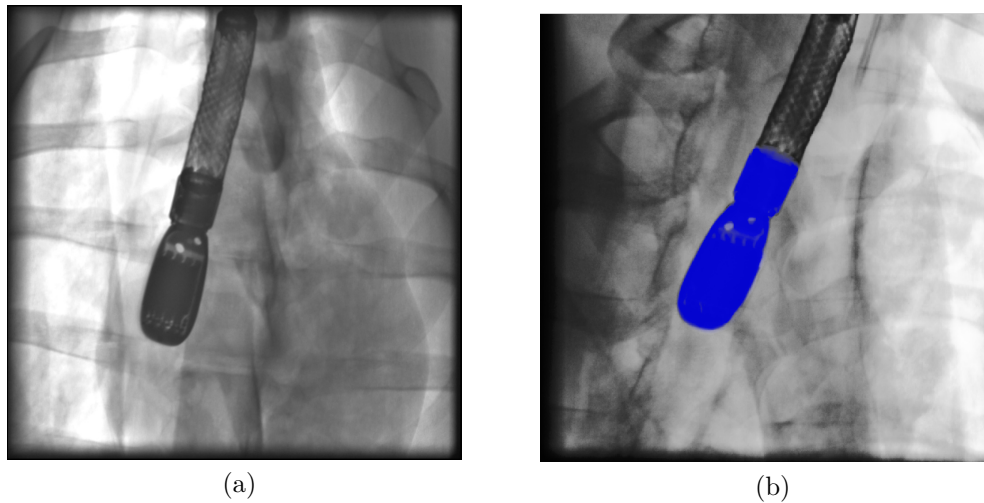


Figure 5.6: Examples of a multiplane scene. Image (b) shows a already registered TEE probe.

basically followed the method which was described in Chapter 4. The three different registration strategies were initialized with the same starting parameters. The NGF similarity measure (see Section 4.4.2 for details) was employed for all strategies and the Powell optimizer (see Section 4.5.1 for details) was used with the identical stop criterion and initial step sizes. The three methods were implemented with the iterative behavior like it is shown in Algorithm 5.1.

X-ray images were acquired within a wide range of projection angles to achieve different views to the TEE probe. The C-arm angles were in the range of $\alpha \in [-75, 90]$ and $\gamma \in [15, -30]$ degree. This range was limited by environmental constraints of the angiography lab. The probe was fixed to collect data without movement to enable a ground truth pose estimation from different directions. A ground truth registration was generated manually by careful visual inspection and automatic registration on different views like it is described in Section 4.8.

The registration accuracy was evaluated while registering the TEE probe to different multiplane X-ray image pairs. The registration was tested for a mono- and double-oblique setup, for data with and without probe movement. In total, a various selection of image pairs was taken from a set of 41 different X-ray scenes, similar to Figure 5.6.

Over 300 uniformly distributed random start positions of the TEE probe within an interval of $[-10, +10]$ mm and $[-10, +10]$ degrees were initialized for each image pair. A registration has been performed for each parameter and image pair. If the final mTRE was below 2.5 mm, the registration was assumed to be successful. the calculation of the mTRE is explained in Section 4.7 in detail. The boundary for a successful registration is in line with other 2D-3D registration methods in the literature, for example [Gao 10, Gao 12, Uner 14].

The registration results for mono-oblique data is shown in Figure 5.7 and 5.8. The evaluated scenes are merged over the difference between the projection angles of the two X-ray images, which is indeed the x-axis of the diagram. One can see

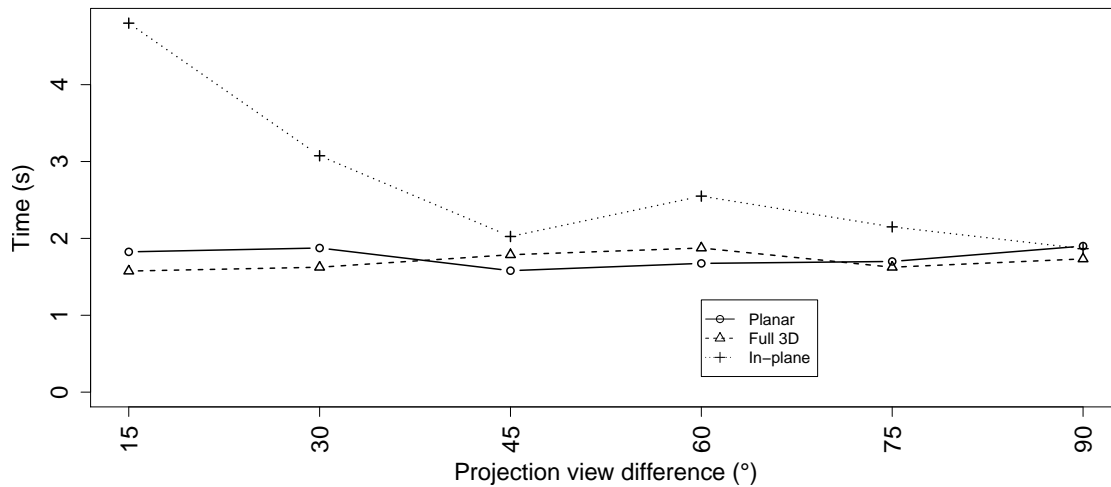


Figure 5.7: Detailed registration runtime performances on a mono-oblique system.

	Planar	Inplane	Full 3D
Success [%]	95.43	75.83	73.57
Time [s]	1.76	2.74	1.70

Table 5.1: Mean success ($mTRE \leq 2.5$ mm) and runtime results for the mono-oblique setup.

in Figure 5.7 that the presented approach is close to constant runtime, independent of the projection angle difference. This is in contrast to the conventional inplane approach, particularly for small differences. The runtimes of the planar and the full 3D approach are similar, but full 3D has a lower success rate. The conventional inplane method mostly fails on very low angle differences, while it adapts the planar results with increasing angle differences. The results are summarized in Table 5.1. As it can be seen here, the double-oblique views have a negative influence on the overall registration accuracy while the planar approach is still more robust than the others. However, an increasing runtime can be observed.

In addition, the new approach was also tested on data, where a slight movement of the probe was encountered. Usually, the conventional registration algorithms fail

	Planar	Inplane	Full 3D
Success [%]	85.92	75.45	59.22
Time [s]	2.29	1.67	1.70

Table 5.2: Mean success ($mTRE \leq 2.5$ mm) and runtime results for the double-oblique setup.

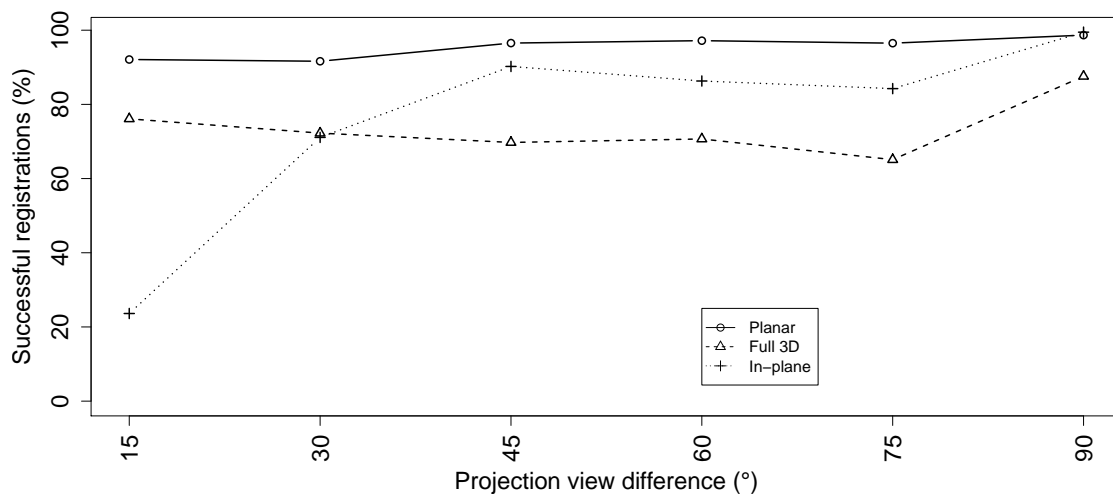


Figure 5.8: Detailed registration accuracy performances on a mono-oblique system.

	Planar independent	Inplane	Full 3D
Success [%]	81.4	38.3	30.1
Time [s]	3.44	14.22	1.59

Table 5.3: Mean success ($\text{mTRE} \leq 2.5$ mm) and runtime results for data with probe movement.

because of the varying 2D information. The new biplane approach with decoupled translation parameters can resolve that issue to a certain degree. The inconsistent image pair was handled in a way, that two ground truth parameter sets were established. The decoupled registration results in two different parameter sets. One for image A and another for image B. Therefore, the evaluation had to be done separately for each single image and not for the image pair. The registration itself was still performed as described in Algorithm 5.2. The offset between the two ground truth positions was up to 10 mm for the used data.

An exemplary comparison between the normal inplane and the decoupled planar approach for one image pair with movement is given in Figure 5.9. Both graphs show the combined registration results from image A and B compared to the initial start position in terms of mTRE.

Compared to the independent approach (shown on the right), the conventional inplane method (shown on the left) has a low accuracy and a high variance in the final results. The summarized results are shown in Table 5.3. In contrast to the independent approach, both conventional methods show poor results in accuracy. With 14.22 seconds, the runtime for inplane is very high.

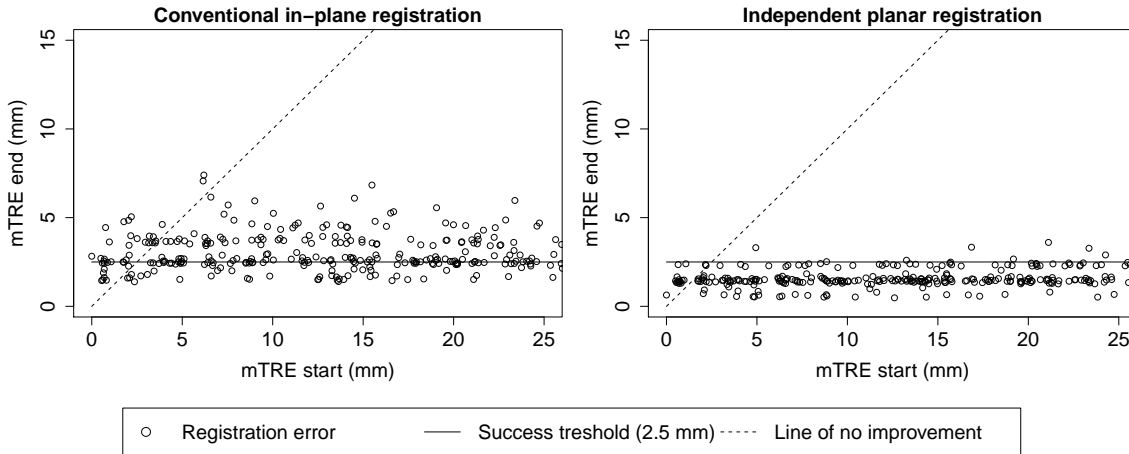


Figure 5.9: Example result for registration on data with probe movement.

Approach	Time	t_x (mm)	t_y (mm)	t_z (mm)
Planar	2:14 min	0.38 (0.11)	0.55 (0.31)	0.66 (0.28)
Inplane	4:57 min	0.25 (0.13)	0.60 (0.25)	0.43 (0.27)
		θ_{yaw} (degree)	θ_{pitch} (degree)	θ_{roll} (degree)
Planar		1.25 (0.73)	0.52 (0.35)	2.84 (2.39)
Inplane		2.67 (1.81)	2.84 (0.93)	4.13 (3.73)

Table 5.4: Summarized results with standard deviation over all users and scenes.

5.4.2 Evaluation of Manuel Registrations

The presented approach was also evaluated within a user study. The users had to manually register a TEE probe model to different pairs of biplane X-ray scenes with the tool which is shown in Figure 4.15, once by using the inplane method and once the presented planar approach. The time was measured until a user was able to achieve a visually satisfying registration which was decided by the user. Each user was shortly trained to establish a common understanding of an accurate registration. The accuracy of the achieved registration for each single parameter using both approaches was measured as well.

A total number of 5 users manually registered 4 pairs of X-ray sequences. The image pairs had a rotational offset ranging from 15 to 60 degrees. The results are presented in Table 5.4. In summary, the registration time with the planar approach was only one half of the time of the inplane approach. Both methods show a similar accuracy for the translational parameters. However, the planar approach shows clear improvements for the rotational parameters.

5.5 Discussion & Conclusion

In general, the planar approach shows about 25% higher accuracy than the compared methods. The accuracy and runtime of the conventional inplane approach is limited by its iterative behavior shown in Figure 5.3a. This effect can be observed especially for small angle differences. The smaller the angle, the more iterations are needed for convergence. For angles smaller than 15 degrees, the errors that are implicitly made for switching between the both images is too large and the algorithm tends to converge to a local minimum. These results are also in line with the findings by [Uner 14], which are determining a 15 degrees difference as minimum for biplane registrations.

Because of the invariant inplane parameters, the planar algorithm avoids additional iterations. Planar and inplane methods have the identical behavior for 90 degrees difference. The invariance of the inplane parameters provides a better starting position on the respective other plane during optimization and increases the probability to find the correct minimum.

The full 3D strategy success rate is mostly lower. A reason is that the 3D position of the object is changed along the axes of the object which are not necessarily aligned with the image axes. In our implementation, the object is aligned to the inplane directions of image A which is obviously not true for image B. Therefore, out-of-plane and inplane parameters are mixed and are not separated during optimization which can cause the optimizer ending up in a local minimum – except for a 90 degree offset, where the full 3D approach improves significantly.

Double-oblique projection angles have an even bigger influence on the accuracy which can be seen in Table 5.2. This is due to the additional instability caused by the extra rotation of the C-arm. This causes the inplane approach to make major errors during the iterations.

The experiments showed that the independent planar approach is a solution for the problem with slight probe movement. Because there is no consistent 3D position, the conventional approaches try to find a compromise between both 2D image positions, respectively decide for one of the two possible positions. Decoupling the translation fixes this issue. Because of the iterative optimization, the inplane approach tends to bounce between both positions which results in the increased runtime.

The novel approach clearly achieves better results for non-perpendicular settings and with its constant runtime facilitates a seamless integration into clinical workflows. The presented approach is specialized on objects that have a “natural” centerline which represents the roll axis. Most technical objects in medical interventions (e.g. catheters, endoscopes) have a distinct centerline, as well as anatomical structures like an aorta, vessels or head. That means that the presented approach can be potentially adopted to a various range of registration problems.

The planar approach shows superior results for the manual performed registration as well. The necessary registration time with the planar technique dropped to 50% compared to the inplane procedure. An improvement in the registration accuracy of the rotational parameters is observed as well. Additionally, all users reported a significant better usability while using the planar approach.

Mesh-based Registration

6.1 Motivation.	65
6.2 Methods	66
6.3 Experiments & Results	70
6.4 Conclusion.	75

During the last decade, lots of work has been made for the improvement of 2D-3D registration quality but even more for the registration runtime performance. The implementation of 2D-3D algorithms for GPGPU architecture and the use of other techniques made a big impact on the runtime which makes those algorithms almost real-time. Nevertheless, the generation of the DRRs is still a bottleneck for classical 2D-3D registration which prevents interactive registration updates for image fusion. Therefore, there is a need to accelerate the generation of DRRs which is the most time-consuming part of the overall process. One possible opportunity for speeding up a 2D-3D registration system is presented in the following chapter. This chapter covers the new technique of exchanging the commonly used DRR generator with a new mesh based renderer which achieves a speed-up of the registration and paves the way to a real-time 2D-3D TEE probe registration. Parts of this chapter have been published in [Kais 13a] and [Kais 13c].

6.1 Motivation

A 2D-3D registration workflow, like described in Chapter 4, is an iterative process. Here, the generation of the DRRs in every iteration is one big performance bottleneck. Usually, the generation of this new artificial images require the most time in the whole process. Lots of work has been done on speeding up the DRR generation with various techniques, for example shear-warp factorization [Wees 99] or wobbed-splatting volume rendering [Birk 05]. The biggest impact was made with the usage of modern graphics cards and the adaption of the algorithms to the GPGPU architecture as shown in [Krug 03] or [Hofm 11].

There are also opportunities to replace the expensive volume ray-casting approach with other methods. One application-oriented example is by using projections of binary coronary models to register coronary angiograms [Turg 05]. [Aoua 08] tried to generate DRRs from homogeneous CAD models while they modeled the attenuation of the X-ray beams in accordance to the distance from entry to exit point. In



Figure 6.1: Exemplary comparison between a ray-casting DRR (upper row) and a DRR based on mesh-rendering (lower row) from the same point of view. The real DRR is shown on the left, horizontal edge images are shown in the middle, vertical edge images on the right.

[Miao 13a], the authors implemented a ray-casting approach to generate realistic-looking DRRs from a mesh. They considered the travel distance of each ray and the object's attenuation.

The approach presented here aims to provide best performance for the specific case of TEE probe registration. It also implements a mesh based DRR generation method, which is similar to the previously named publications, but tries to avoid expensive ray-casting or ray-tracing and uses simple mesh rendering instead.

6.2 Methods

The main principle of the approach is to generate DRR-like images with basic rendering of a triangular mesh. The different attenuation in the X-ray image is simulated with different alpha blending depending on a colormap which was generated with regard to the thickness and density of different object structures. The mesh must be available and must be preprocessed in advance, which applies for the TEE probe. This is different to a general 2D-3D registration method which can use any 3D volumetric data. Examples of a comparison between a conventional and a mesh-rendered DRR are shown in Figure 6.1 and Figure 6.2.

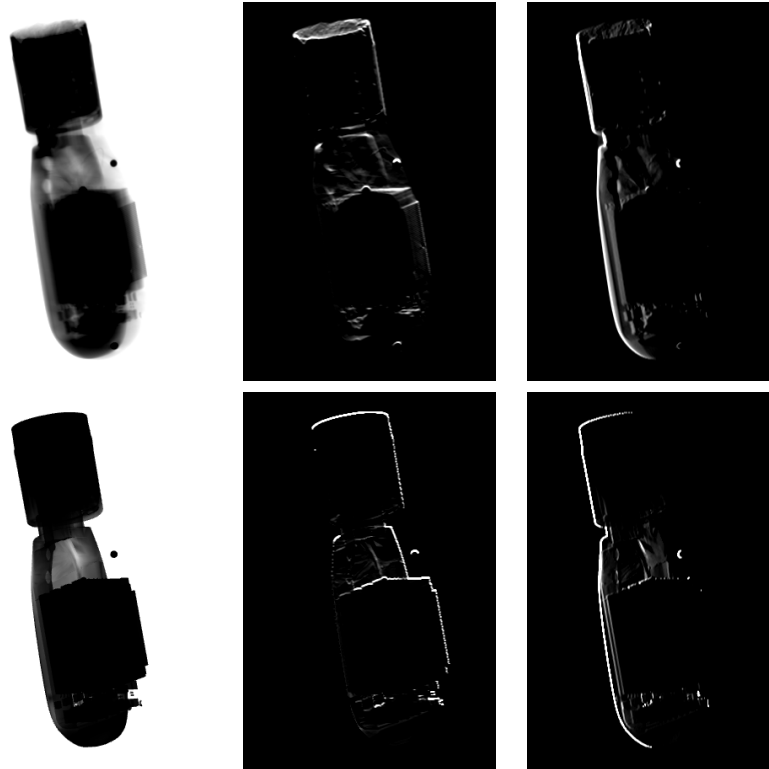


Figure 6.2: Exemplary comparison between a ray-casting DRR and a mesh-rendering based DRR like in Figure 6.1 from another point of view.

6.2.1 3D Mesh Model Generation

The basis of the algorithm is a triangular mesh of the TEE probe which had to be generated from a CT dataset. The 3D volume was acquired and post-processed like described in Section 4.2. In the next step, a triangular mesh was created from the cleaned 3D dataset with a standard isosurface algorithm. The problem here was to choose an isovalue which was a good compromise between including all details from the probe's structure and excluding remaining metal artifacts, especially between small details. Some metal artifacts had higher HU values than real probe structures.

The next step of post-processing was a partly remodeling of the TEE probe with Blender [Blen 14], which had two essential advantages. The first was to rebuild structures that were thresholded by the isosurface algorithm like newly formed holes or tiny structures that were mostly disrupted by metal artifacts. The second advantage was that one could save on the number of triangles, especially for circular structures. This can be done more effectively by remodeling than by mesh decimation. A screenshot of Blender with the remodeled probe is shown in Figure 6.3. The remaining parts of the mesh were simplified with the use of the quadratic edge collapse decimation in MeshLab [Visu]. The smaller the amount of triangles in the mesh, the faster the rendering. The final TEE probe mesh had a total number of about 18.000 faces.

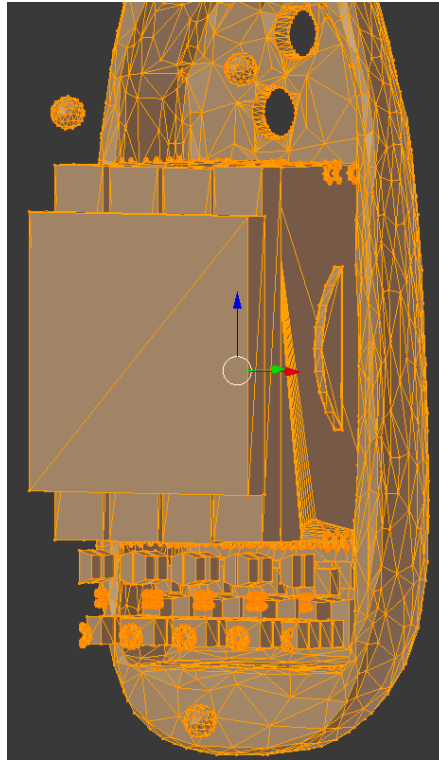


Figure 6.3: Screenshot of the TEE probe mesh opened in Blender.

6.2.2 Mesh-based DRR Rendering

The DRR creation is done by rendering the mesh with a gray color and with additive alpha blending which results in higher gray values where more parts or parts with higher attenuation are overlapping. It is necessary for a realistic rendering to know the approximate attenuation of the single mesh parts. As described in Section 4.3, the attenuation depends on the attenuation coefficient and the thickness of the radiographed material. Most parts of the TEE probe consist of the same material which leads to the assumption that the local thickness is the determining factor for X-ray attenuation. For the triangular mesh, this local thickness is encoded as a colormap of a single mesh vertex.

The thickness is approximated automatically by the Shape Diameter Function (SDF) [Shap08]. Initially designed for the task of mesh partitioning and skeletonization, the SDF can be seen as a function of the neighborhood diameter and, therefore, of the thickness of a mesh at a local vertex. The SDF traces rays from a vertex inside the mesh, like shown in Figure 6.4. The local thickness corresponds to the weighted sum of the ray's distances. Additional parameters of the SDF, like number of rays, angle of the ray tracing cone or outlier removal, must be chosen in respect to the current object. The result of applying the SDF to the generated TEE probe mesh is shown in Figure 6.5. Additional manual coloring of the mesh has been necessary on parts which consist of different materials, for example the ball markers or the Ultrasound array.

The final rendering was obtained with the standard OpenGL rendering pipeline. The color of each mesh vertex was used as alpha value of the painted face color.

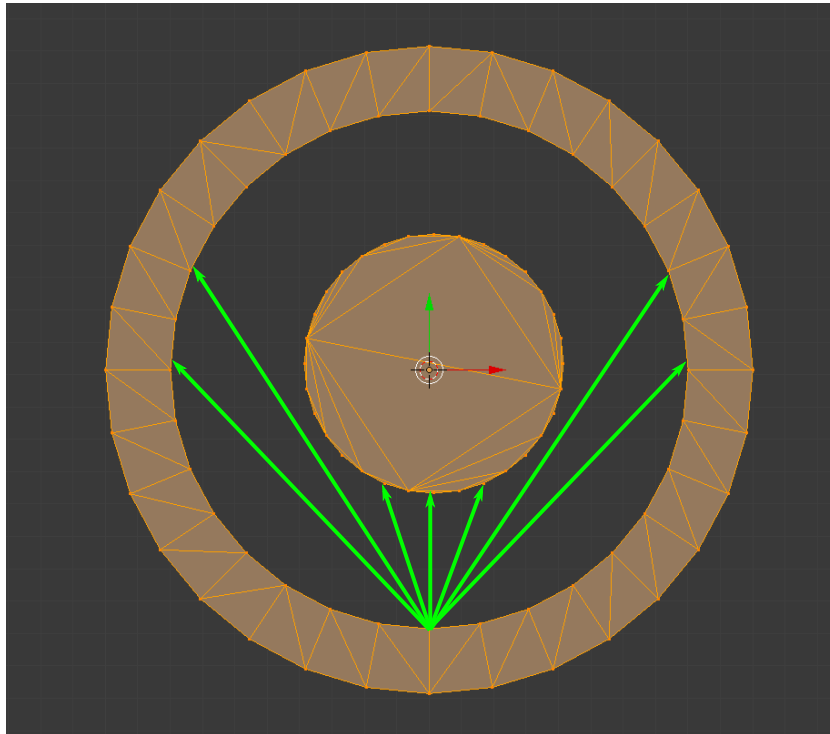


Figure 6.4: Illustration of an application of the Shape Diameter Function. Rays are traced inside the mesh. The weighted sum of the distances represents the local thickness of the mesh.

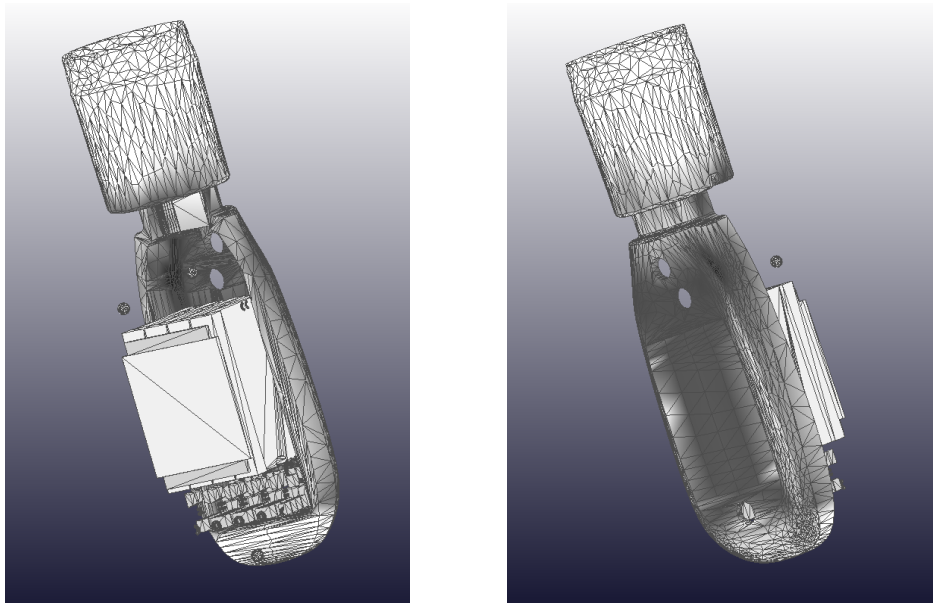


Figure 6.5: Results of the Shape Diameter Function applied to the TEE probe mesh with additional post-processing. Dark parts represent thin structures. Light parts represent structures with high X-ray attenuation.

Because X-ray has a transilluminating effect, there was no need to care about depth buffering. The darkness of the part of the rendered probe is directly influenced by the number of overlaid faces. The whole mesh was drawn with additive alpha blending while the alpha value of a pixel determined the whole color. If a_A is the destination alpha value and a_B the source alpha value, the resulting color C_0 is then given by the blending function:

$$C_0 = \min(a_A + a_B, 1). \quad (6.1)$$

The source alpha is encoded in the vertex color C_V and is given by

$$a_B = 1 - C_V/255. \quad (6.2)$$

It is assumed that the RGBA values of the initial image are $(1, 1, 1, 0)$ with color values normalized to $[0..1]$.

6.2.3 Rendering and Similarity Measure Pipeline

OpenGL was used to render the meshes and CUDA for fast calculation of the image gradients and the evaluation of the gradient correlation similarity measure. The OpenGL interoperability of CUDA was used to provide the rendered meshes from the OpenGL framebuffer directly as input to the following CUDA processing. The CUDA implementation was optimized specifically for the gradient correlation and sum of absolute differences similarity measure by parallelizing the gradient image computation and the following normalized cross correlation. Efficient texture and shared memory lookups and fast GPU reduction algorithms were utilized, like presented in [Harr 07].

6.3 Experiments & Results

The mesh-based approach was evaluated on a set of 29 X-ray sequences acquired during a porcine cadaver experiment to eliminate motion. Fluoroscopic images were acquired as well as acquisition sequences with higher dose. The TEE probe was imaged from a various range of C-arm angles while the probe remained in a fixed position. The C-arm angles were in the range of $\alpha \in [-45, +45]$ and $\gamma \in [0, -15]$ degree. The ground truth position of TEE probe was obtained by a combined manual mono- and biplane registration of each sequence, like described in Section 4.8. The approach was tested on mono- and biplane registration cases while the planar technique from Chapter 5 was employed for the registration algorithm.

The presented mesh-based DRR generation approach was compared to a standard volume-based ray-casting approach. The volume had a size of $160 \times 144 \times 472$ voxels with a voxel resolution of 0.1 mm. The sampling factor of the rays was 1 which means that the step size for each ray was 0.1 mm. The ray-casted DRR image was normalized with a transfer function similar to Figure 4.8. The optimization pipeline was the same for the ray-casting DRR generation, which means the generated DRR and the similarity measure calculation were processed directly on the GPU, as well as described in Section 6.2.3.

A registration was carried out for 50 different starting points for each X-ray sequence. The starting points were uniformly distributed in the range of $t_x, t_z \in$

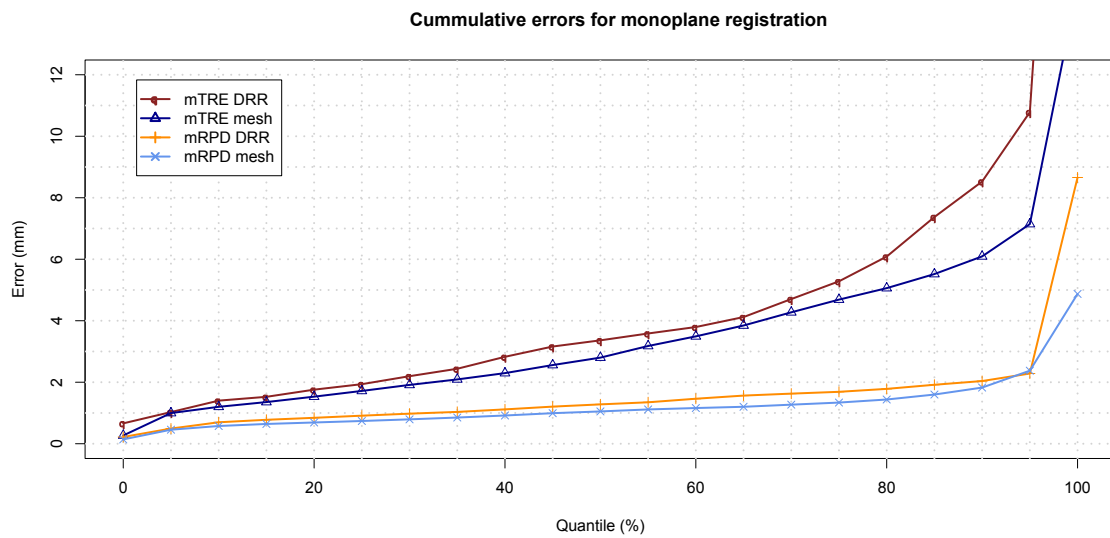


Figure 6.6: Comparison between registration with ray-casting DRRs and mesh-rendered DRRs for the mTRE and the mRPD error metric for monoplane registration.

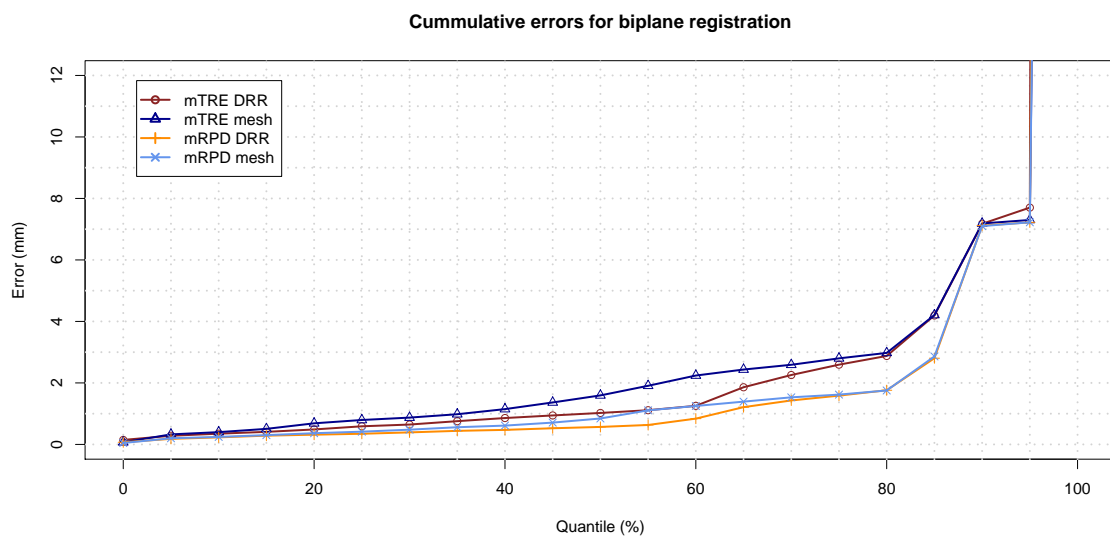


Figure 6.7: Comparison between registration with ray-casting DRRs and mesh-rendered DRRs for the mTRE and the mRPD error metric for biplane registration.

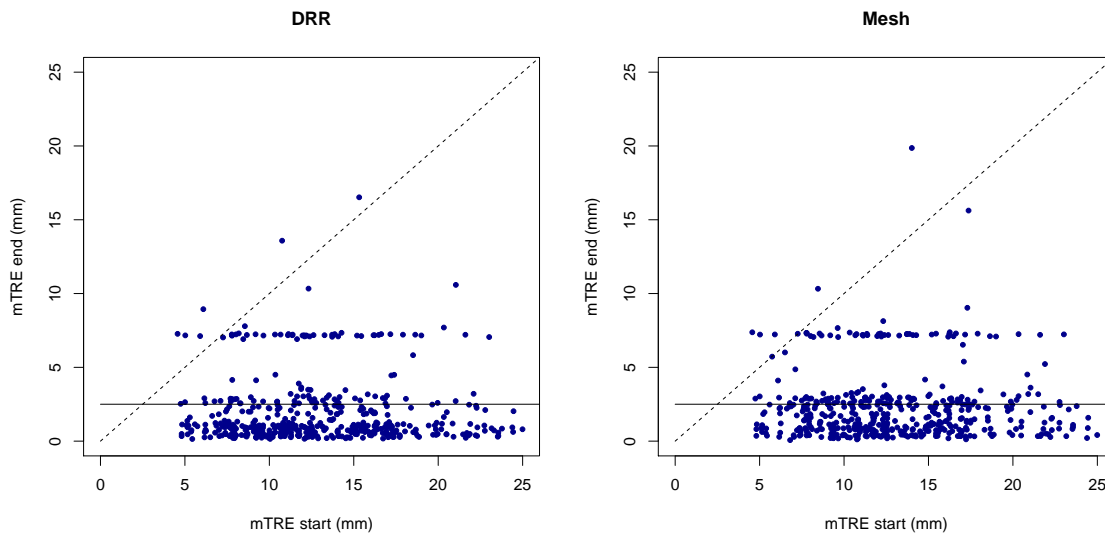


Figure 6.8: Plot of start and end mTRE comparison of all biplane registrations. The solid line is the 2.5 mm mTRE which can be seen as the border of successful or failed registration. The dotted line means the line of no improvement. All initial poses above this line were not improved by the algorithm.

	t_x	t_z	t_{depth}	θ_{yaw}	θ_{pitch}	θ_{roll}
DRR	0.09 (0.07)	0.11 (0.09)	3.44 (3.00)	0.25 (0.21)	1.02 (0.66)	1.38 (0.79)
Mesh	0.12 (0.08)	0.14 (0.08)	2.80 (2.08)	0.24 (0.19)	1.52 (0.81)	0.94 (0.69)

Table 6.1: Mean values of parameter errors of successful monoplane registrations for the mesh and the DRR approach.

$[-3, +3]$ mm, $t_y \in [-15, +15]$ mm, $\theta_{yaw} \in [-4, +4]$ degree and $\theta_{pitch}, \theta_{roll} \in [-8, +8]$ degree for monoplane registrations. For multiplane registrations the intervals were chosen as $[-10, +10]$ mm and $[-10, +10]$ degree. There have been 29 sequences for monoplane and 10 sequence for biplane registrations available for testing. The optimization parameters have not been changed for the two approaches. The optimization strategy and the similarity measure have been the same as described in Chapter 4 with the use of the planar strategy from Chapter 5 for the biplane sequences. The errors were measured in terms of mTRE and mRPD (see Chapter 4.7 for a detailed description).

All experiments were carried out on a workstation (Intel Xeon E5, 12 cores with 3.20 GHz, 32 GB RAM) with an NVIDIA Quadro K5000 (1536 CUDA kernels, 705 MHz, 4 GB GPU RAM, CUDA compute capability 3.0).

The results for the monoplane registrations can be seen in Figure 6.6. A detailed overview of the parameter errors for all six degrees of freedom and the mTRE and mRPD errors metrics can be found in Figure 6.9 and Table 6.1. One can see that both approaches show similar results in registration accuracy as well as for the single parameters. The mesh approach is slightly superior in most of the test cases. The

	t_x	t_z	t_{depth}	θ_{yaw}	θ_{pitch}	θ_{roll}
DRR	0.07 (0.05)	0.07 (0.04)	0.19 (0.19)	0.12 (0.1)	0.39 (0.29)	0.91 (0.82)
Mesh	0.08 (0.15)	0.12 (0.2)	0.17 (0.2)	0.15 (0.21)	0.35 (0.33)	1.25 (0.88)

Table 6.2: Mean values of parameter errors of successful biplane registrations for the mesh and the DRR approach.

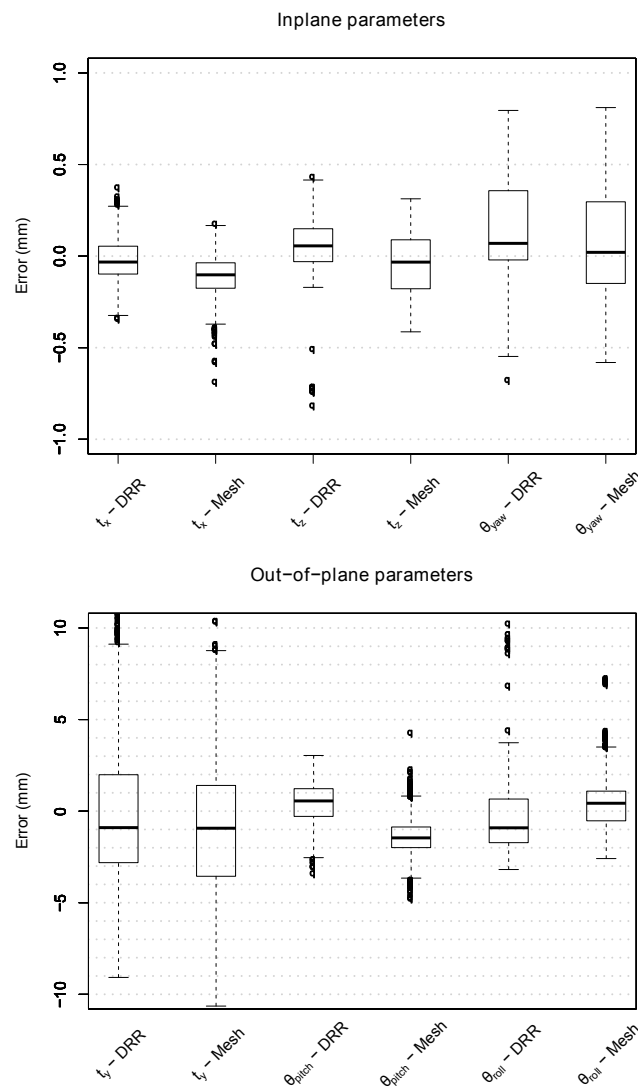


Figure 6.9: Comparison between registration with ray-casting DRRs and mesh-rendered DRRs for all six degrees of freedom.

Resolution	Volume-based		Mesh-based	
	DRR generation	Evaluation	Mesh rendering	Evaluation
1024 ²	21.19	1.14	0.96	0.91
512 ²	10.55	0.60	0.50	0.46
256 ²	2.60	0.27	0.36	0.45
128 ²	0.96	0.26	0.34	0.36

Table 6.3: Comparison of runtimes in milliseconds for the DRR or mesh generation and the evaluation of the similarity measure for different resolutions.

	Volume-based (s)	Mesh-based (s)
Monoplane	1.69 (0.35)	0.48 (0.06)
Biplane	6.06 (2.02)	1.14 (0.4)

Table 6.4: Runtime for volume-based and mesh-based approach for mono-and biplane registrations in seconds.

95%-quantile is 2.28 mm (mean 1.37 mm) for the DRR and 2.38 mm (mean 1.15 mm) for the mesh approach in terms of RPD. In terms of TRE, which shows the 3D error, the 95%-quantile is 10.78 mm (mean 4.32 mm) for the DRR and 7.14 mm (mean 3.36 mm) for the mesh approach. Here, the mesh-based method shows a significant improvement for about 15% of the test cases. The detailed parameter evaluation is plotted without normalization to show the aberration direction of the error. As it can be seen in the boxplots, the parameter errors are centered around 0 but sometimes with a systematical aberration in another direction, especially for parameter θ_{pitch} .

It can be seen in Figure 6.7 and Table 6.2 that the biplane test cases are very similar to the monoplane ones. Both approaches show similar results in terms of mTRE and mRPD. The standard DRR approach is slightly superior compared to the mesh approach within the 50% - 70% quantile for the mTRE. Figure 6.8 shows a plot of start and end mTRE. Each point is a test case from any of the biplane sequences. A higher start-mTRE means that the registration was started with a higher deviation from the ground truth. A lower end-mTRE means a better registration results. One can see that the registration results for both approaches are basically cluster around the same region.

The most significant difference between both approaches is visible in the timing performance. Table 6.3 shows the runtimes of both approaches for different resolutions. The overall registration runtime performance is compared in Figure 6.10 and Table 6.4. The DRR approach still needs on average 1.69 s for monoplane and 6.06 s for the biplane cases, the mesh approach speeds up to 0.48 s, respectively 1.14 s.

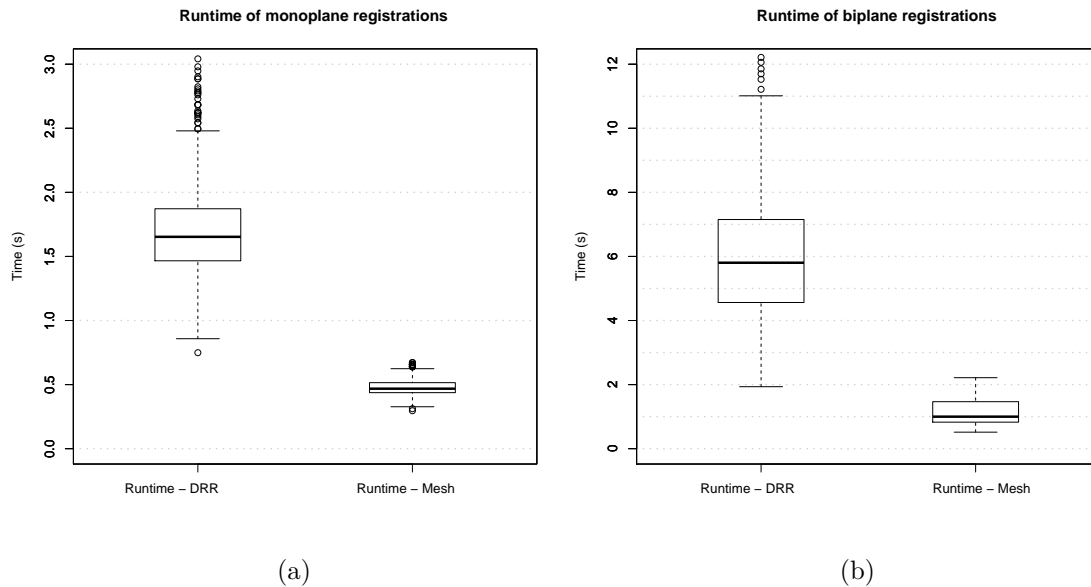


Figure 6.10: Comparison of runtimes per registration of ray-casting and mesh-based DRR generation for monoplane (a) and biplane (b) registrations.

6.4 Conclusion

The presented approach of substituting the ray-casting DRR generation with mesh-based rendering is a simplification of the DRR generation process. This simplification is an estimation and not physically correct. It abstracts the common DRR generation process and tries to reproduce the same image impression with a fast mesh rendering. This works in the examined cases for the TEE probe model. Especially with the combination of a normalized and edge based similarity measure that ignores mostly the absolute gray value and concentrates on distinctive edges caused by prominent structures with large gray value differences. It can be seen in the results that the mesh based approach shows very similar results compared to the DRR approach. No approach shows significant differences in accuracy, neither for the monoplane nor the biplane experiments. That means that the DRR simulation by mesh rendering is a sufficient approximation of the common volume-based ray-casting DRR generation.

However, the timing performance shows an entirely different picture. Although all parameters of the optimization process remained fixed, the timing performance of the mesh approach is significantly better. The basic rendering of the mesh is computationally much faster than the standard ray-casting algorithm. The runtime of the ray-casting is heavily dependent on the target resolution, while the mesh rendering basically stays within the range of 1 ms. This is because the rasterization process is more or less dependent on the number of triangles, which is relatively low compared to, for example, today's computer games. However, the volume ray-casting is heavily dependent on the number of rays that are used to cast the volume.

It is noticeable that the runtime of the similarity measure evaluation shows high differences between both approaches. That can be explained that the OpenGL-CUDA interoperability, which renders directly into CUDA-shared textures, works faster than

copying memory, which is necessary for the ray-casting results, even if it is performed on the GPU.

To summarize, the new mesh approach shows a speed-up of about 3.5 for the monoplane, respectively 5.3 for the biplane registration. With that performance, the presented approach can pave the way to real time 2D-3D registration. It can also be employed to different registration problems, especially for the registration of technical objects that are known in advance, for example endoscopes or different catheters.

Detection-Registration-Pipeline for Probe Pose Estimation

7.1 Motivation	77
7.2 Description of Complete Pipeline	78
7.3 Experiments & Results	78
7.4 Discussion & Conclusion	88

The work for this thesis was planned in the first place to be a part of a more comprehensive pipeline. In this pipeline, different algorithms should cooperate to gain better results in estimating the TEE probe pose, especially in terms of runtime performance. This chapter describes how the whole pipeline is set up, how the different detection and registration algorithms interact and which advantages arise compared to other approaches.

7.1 Motivation

As mentioned in the chapters before, 2D-3D registration needs a good initialization of the six starting parameters to generate reliable and accurate results. The parameter interval for starting parameters that achieve convergence to the correct registration is called the capture range. A larger capture range means that the initialization of the algorithm can be further away from the ground truth position. Some approaches have been published during the last years to extend the usually small capture ranges of 2D-3D registration algorithms. In [Varn 13a, Varn 15], the authors used the Generalized Hough Transform [Ball 81] of reprocessed DRRs of a wide range of parameters to find a good initial position. Another work [Bom 10] showed how to use the projection-slice theorem and phase correlation to provide a good initialization. Unfortunately, All the named approaches show the lack of real-time performance.

In this work, it was chosen to combine the advantages of the detection algorithms from [Moun 12] and [Heim 13, Heim 14], which are introduced in Section 3.2, with the 2D-3D registration techniques presented in the Chapters 4, 5 and 6. In general, one can think about detection-based algorithms as fast and 2D-3D registration as slow. However, detection is not showing the same good accuracy than registration.

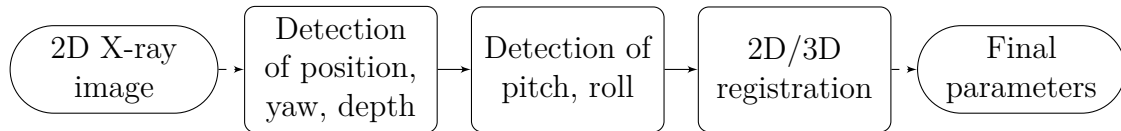


Figure 7.1: Complete detection-registration-pipeline for probe pose estimation.

Therefore, it was chosen to employ the detection algorithms to initialize the 2D-3D registration algorithm inside its capture range.

7.2 Description of Complete Pipeline

The overall pipeline for the detection and registration of the TEE probe consists of three steps, which are shown in Figure 7.1. Firstly, the detection algorithm of [Heim 13] is used to determine all three inplane parameters t_x , t_z and θ_{yaw} and the out-of-plane depth t_y , which is mentioned by the authors as scale of the probe within the 2D image. Then the algorithm from [Moun 12] is taking these results as initialization and is estimating both out-of-plane rotational parameters θ_{pitch} and θ_{roll} . All six spatial parameters are then initialized and are passed into the 2D-3D registration algorithm.

It is necessary to use planar parameters, which are described in Chapter 5, to pass the starting parameters to the 2D-3D registration to ensure that the provided detection coordinates are not distorted by the projection geometry. The detection algorithms are working in the projective 2D space of the image, but the registration is working in a 3D space. Therefore, the same effect as shown in Figure 5.1 and Figure 5.2 would occur when using spatial parameters. A probe position away from the central beam, respectively the center of the image, would have a different image impression, especially in rotations. It is shown in Section 5.2.1 how to transform those planar parameters into spatial parameters to correct the projective aberration. The registration can be started after the conversion from planar into spatial parameters.

Due to the reported accuracy of the detection algorithms, one can tightly limit the search space of the registration. The used boundaries can be seen in Table 7.1. This limitation is necessary to bring the six starting parameters inside the capture range of the registration algorithm. More positive effects of the narrow boundaries are reducing the probability of outliers and reducing registration times.

7.3 Experiments & Results

Two experiments were carried out. Firstly, an experiment to understand the capture range of the 2D-3D registration algorithm. The second experiment was done to evaluate the whole detection-registration-pipeline for TEE probe pose estimation.

7.3.1 Capture Range Estimation

Choosing reasonable boundaries and search intervals is a crucial decision for 2D-3D registration algorithms. If the possible parameter boundaries are chosen to small, it

Parameter	Boundaries
Position t_x, t_z	± 3 mm
Yaw θ_{yaw}	± 3 degree
Depth t_y	± 2 % $\cong \pm 15$ mm
Pitch θ_{pitch}	± 8 degree
Roll θ_{roll}	± 8 degree

Table 7.1: Boundaries for the 2D-3D registration algorithms based on detection accuracy which is related to the errors reported in [Heim 13] and [Moun 12].

is possible that the correct position can not be found. If the boundaries are too large, it can happen that the optimizer searches along the wrong direction and ends up in a local optimum. It is assumed that the search space of the 2D-3D registration can be reduced with better results of the preliminary detection steps, which should result in less outliers and higher accuracy.

An experiment to estimate the capture range of the 2D-3D registration algorithm was carried out, based on 29 different X-ray images. 50 randomly sampled 3D parameter sets for each X-ray image were used to start a monoplane registration and it was measured how many of this registrations were successful. This procedure was executed for three different parameter boundaries. The range for the starting points of the registration were chosen randomly from these increasing intervals. That means, a larger interval will result in starting points with higher aberration from the ground truth position. This will also cause changes in the setup of the registration algorithm. Primarily, the parameter boundaries must be adapted. But it is also necessary to adjust other optimization parameters like the initial step size and how the search space is reduced on the different resolution levels of the optimization strategy (see Section 4.6 for details).

Interval 1 is related to the detection results from Table 7.1 and represents the range of the minimal errors the algorithm should handle. Table 7.2 shows a listing of the other examined intervals. The registration search space is limited by the interval boundaries. This was performed to figure out how good the 2D-3D registration algorithm can handle initial positions with larger errors. The optimizer was configured in a way that it should stop if the delta between the single results of the similarity measure evaluation drops below a certain value. This ensures that the optimization process is never interrupted too early, even on a larger search space.

The results for the registration based on the three intervals can be seen in Figure 7.2. The three graphs are showing the relation between the starting mRPD and the mRPD after registration. The RPD error was chosen here, because it is more meaningful for a monoplane registration than a 3D error estimation (see Section 4.7 for details of the error measures). The solid vertical line shows the capture range, which is defined as the border where 95% of the test cases were still registered successfully. The boundary of a successful registration was set to 3 mm according to the results of [Hous 12], which is indicated by the solid horizontal line. The dotted

Parameter	Interval 1	Interval 2	Interval 3
Position t_x, t_z	± 3 mm	± 6 mm	± 9 mm
Yaw θ_{yaw}	± 3 degree	± 6 degree	± 9 degree
Depth t_y	± 15 mm	± 15 mm	± 30 mm
Pitch θ_{pitch} , Roll θ_{roll}	± 8 degree	± 16 degree	± 32 degree

Table 7.2: All boundaries/parameter intervals for the capture range estimation experiment.

line is the line of no improvement. All results that lie below this line were improved by the registration.

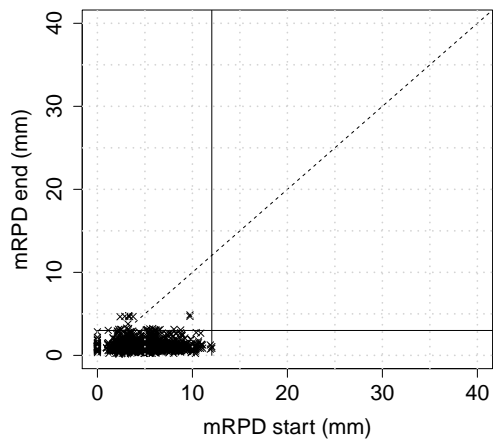
Technically, the capture range for interval 1 can not be determined because less than 95% of the test cases were not registered successfully. The capture range for interval 2 drops to 4.4 mm and 4.5 mm for interval 3. One can also clearly see, that the risk for outliers with an error above 5 mm increases with raising boundaries. The runtime performance of the algorithm was almost constant and not dependent on the intervals.

7.3.2 Marker Target Registration Error

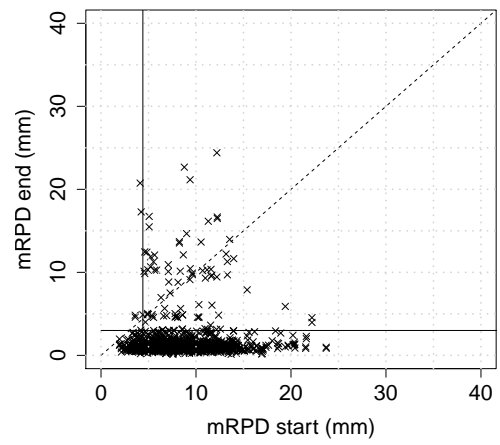
The complete detection-registration-pipeline was evaluated with a phantom experiment where marked points from the Ultrasound image were overlaid onto X-ray images and compared to the manually annotated 2D ground truth position. A phantom was built which is visible in Ultrasound and in X-ray simultaneously. This phantom consists of plastic-coated wires that were spanned into a plastic cylinder in a way that they form four different crossing points (displayed in Figure 7.3a). To view the phantom in Ultrasound, this cylinder was placed and fixed into a water basin together with the TEE probe (see Figure 7.4a). This setup was put inside a C-arm (Artis zee Floor-mounted, Siemens Healthcare, Germany) to display the phantom and the TEE probe in X-ray as well. Figure 7.4b shows the complete setup of the experiment. The TEE probe was fixed inside the basin to eliminate errors from unintentional movement.

In the following, the crossing points of the wires were annotated manually in the 3D Ultrasound image. The marked crossings are displayed in Figure 7.3 with the numbers 8-11 and correlate to the numbers in Figure 7.5. X-ray images of the phantom and the TEE probe were now recorded from different C-arm angulations to simulate different probe positions and rotations. Now the marker points were overlaid onto the X-ray image. According to the general transformation T from Equation 3.1, the probe was detected and registered in each X-ray image to establish the transformation matrix $T_{Model \rightarrow Patient}$. The C-arm projection matrix \mathcal{P} was directly known from the C-arm system. The Ultrasound calibration matrix $C_{US \rightarrow Model}$ was provided by Siemens Healthcare, Ultrasound.

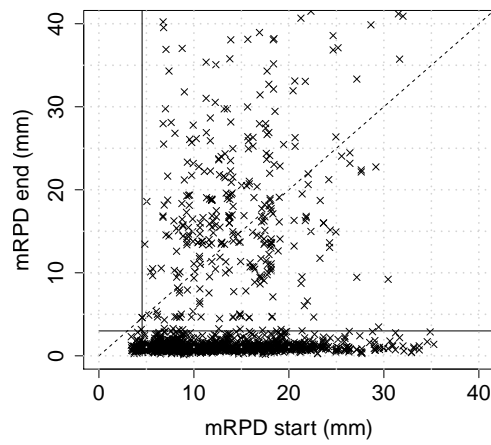
Two experiments were carried out to evaluate the monoplane and the biplane detection/registration accuracy. Firstly, the probe was detected separately in each



(a) Interval 1



(b) Interval 2



(c) Interval 3

Figure 7.2: Results for the capture range experiment.

X-ray image for the monoplane case. The accuracy was measured between the overlaid markers from the Ultrasound volume and the manually annotated ground truth crossing points in the X-ray image, which shows the accuracy of the detection. Secondly, the registration was started with the estimated parameters of the detection algorithms. The accuracy was measured in the same way. The difference between the two accuracy measurements shows if and how much the registration can improve the detection results. Both results are showing the accuracy in the projection image. To evaluate the 3D error as well, the C-arm was rotated by 90 degrees and another X-ray image was recorded without changing $T_{Model \rightarrow Patient}$. Because this new projection direction is perpendicular to the first one, this will especially give an impression about the errors of the out-of-plane parameters of $T_{Model \rightarrow Patient}$ which are mainly responsible for the 3D errors. See Figure 7.5 for an example how the targets were annotated and evaluated. The dotted circles show the manual ground truth annotation, while the solid balls indicate the overlaid markers from the detected, respectively registered and transformed, Ultrasound volume.

The errors were measured in the 2D image only. The final 2D error for each detection/registration is calculated by the mean distance from the marker points to their ground truth position. One can convert the measured pixel differences into millimeters in the 3D space by

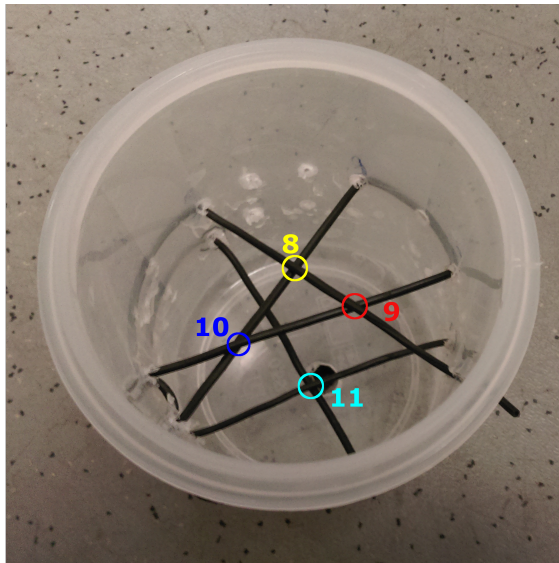
$$\delta_{mm} = \delta_{pixel} \cdot p \cdot \frac{SID}{SISOD} \cdot \frac{sZ_{Xray}}{sZ_{screen}}. \quad (7.1)$$

While δ means the distance between the overlaid marker to its ground truth position and p is the pixel spacing of the X-ray image. sZ_{Xray} and sZ_{screen} are the sizes of the images and provide a normalization in case the native X-ray image and the annotation image have a different resolution. This equation is correct under the assumption that the phantom is positioned in the rotational center of the C-arm, which has been the case for the experiments.

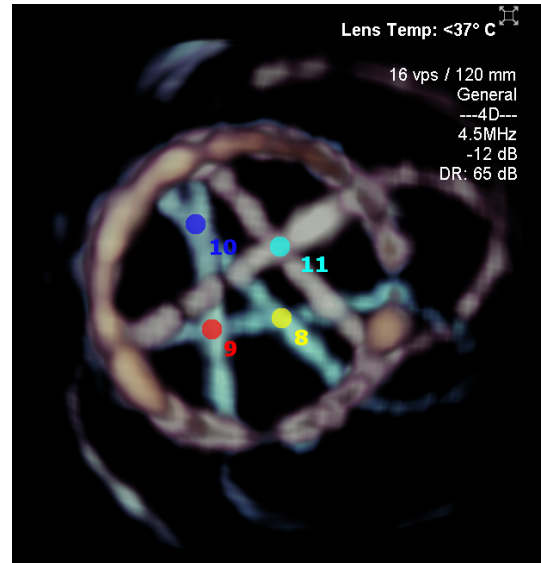
The experiments to evaluate the accuracy for the biplane detection and registration were very similar to the monoplane case. The difference was that the detection and registration algorithms has been initialized with a previous biplane registration result, performed at C-arm angulation $[0, 0]$ and $[-90, 0]$. The now known depth of the probe position was established as a depth constrained for subsequent detections and registrations. The same experiments were then carried out as described for the monoplane registrations.

Over 38 different X-ray images from a C-arm angulation range of $\alpha \in [-60, +90]$ and $\gamma \in [-30, +30]$ were generated and annotated. The monoplane detections and registrations were carried out on 19 different images. According to these images, the corresponding perpendicular X-ray images were acquired to check the out-of-plane accuracy. Table 7.3 gives an overview over the used C-arm angulations. Some examples of the used X-ray images are given in Figure 7.6. The acquisition angles were chosen under the assumption that they provide common views to the TEE probe that are also used during clinical interventions. The possible C-arm movement was limited by the experimental setup, which corresponds to the setup in the clinical field.

The left diagram in Figure 7.7. shows the according results. The graph shows the quantiles of the 2D errors for the four different detection/registration types. The



(a) The multimodal phantom that was used for the experiments.

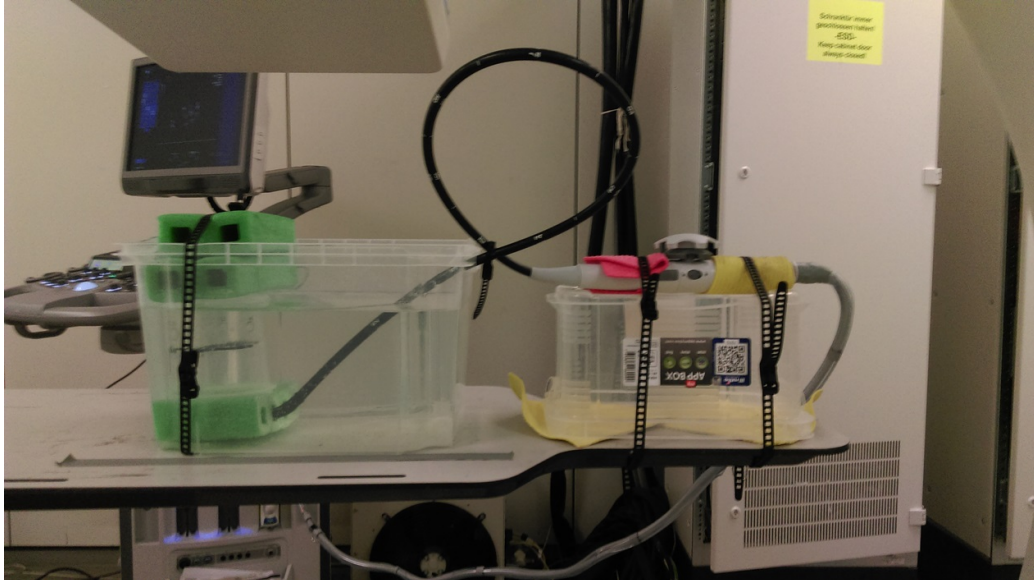


(b) 3D Ultrasound image containing the marked crossings of the wires in the multimodal phantom.

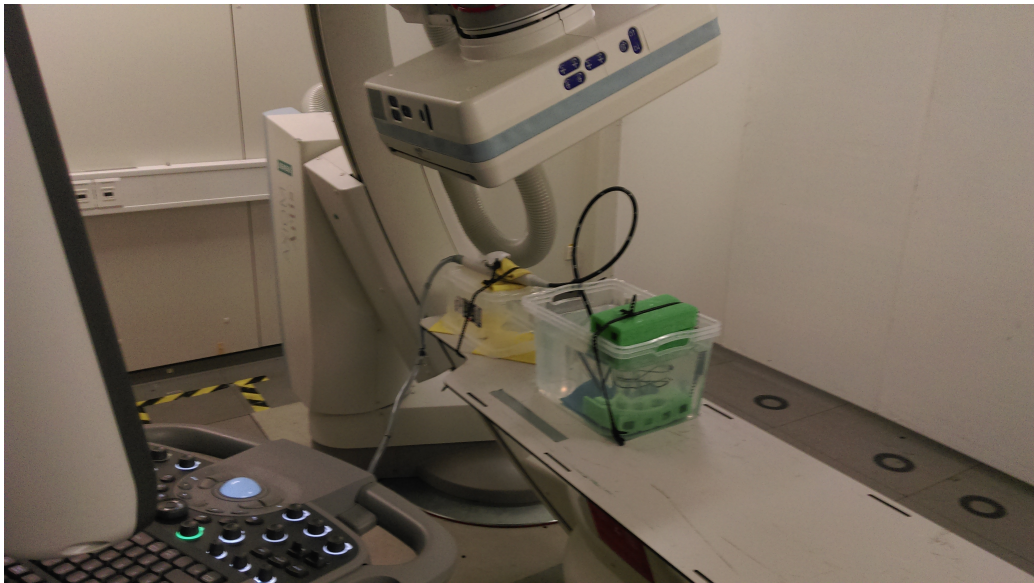
Figure 7.3

$\alpha \backslash \gamma$	-90	-75	-60	-45	-30	-15	0	15	30	45	60	75	90
30							X						O
15	O	O				X	X	X				O	
0	O	O	O	O	O	O	X	X	X	X	X	X	X
-15	O	O	X	X	X	X	X	X	O	O	O	O	
30							X						O

Table 7.3: C-arm angulations (in degrees) of all acquired and annotated X-ray images that were used for evaluation. The 'x' marks angulations which were used for mono-plane registration, the 'o' marks are the perpendicular views to check the out-of-plane detection/registration accuracy.



(a) The phantom inside the water basin. The TEE probe is fixed to the box to suppress any motion.



(b) The phantom placed on the patient table inside a C-arm. The TEE probe is connected to the Ultrasound machine on the left.

Figure 7.4: Setup of the phantom experiment which was used to evaluate the detection-registration pipeline.

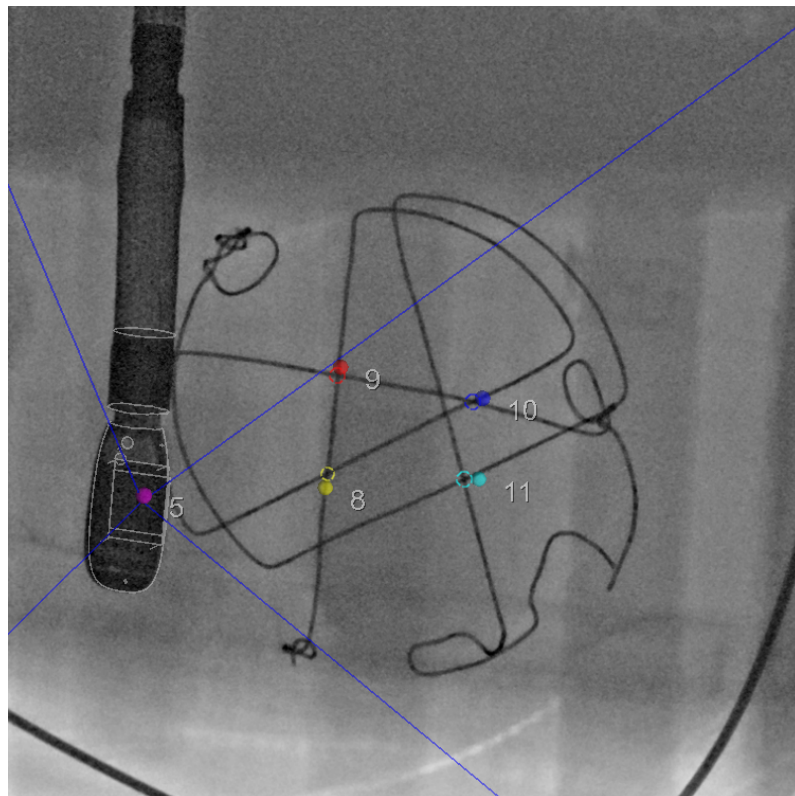


Figure 7.5: Example for overlaid marker points. Solid points are the overlaid markers from Ultrasound, dotted circles are indicating the ground truth positions.

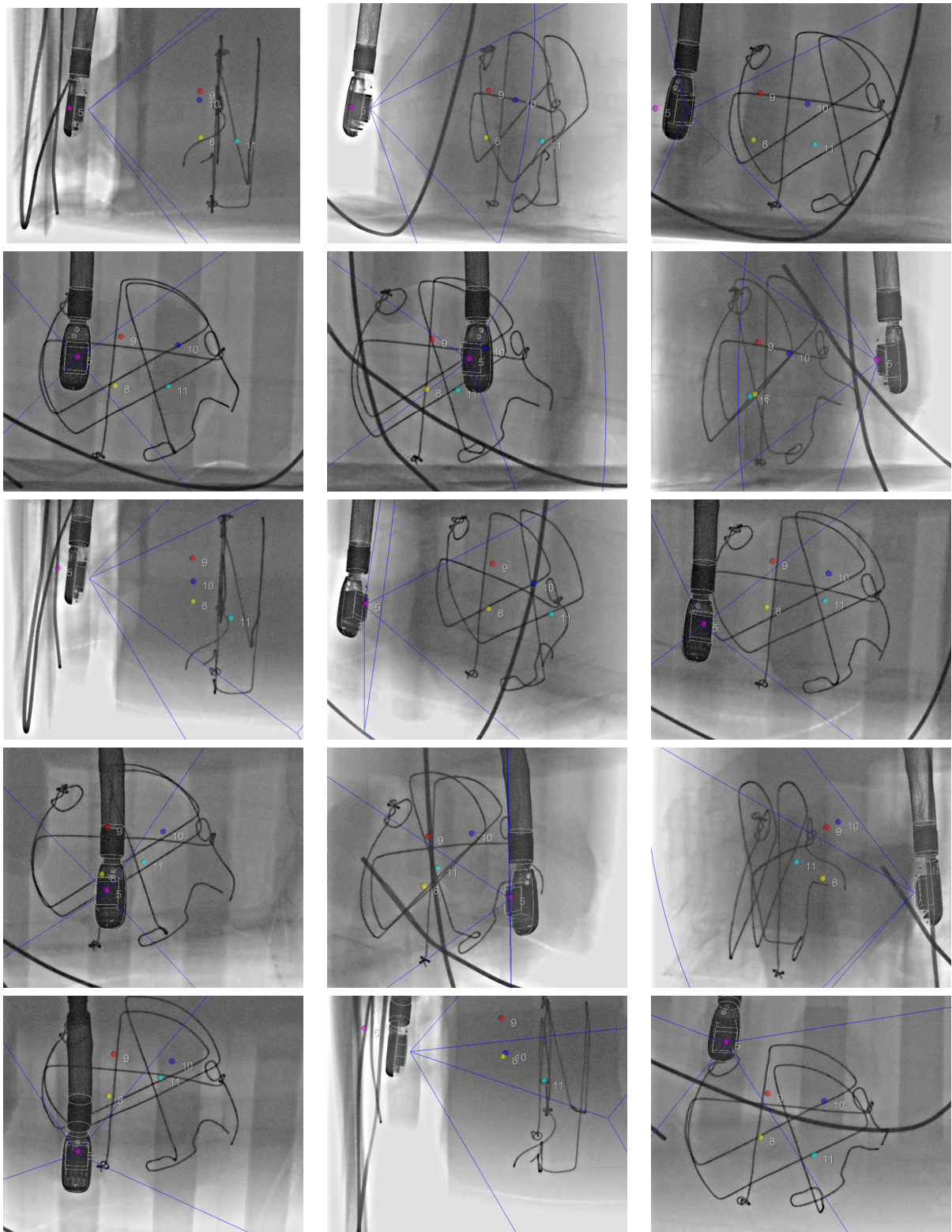


Figure 7.6: Overview over some used X-ray images from different C-arm angles. Please note that the images are cropped to only show the TEE probe and the phantom.

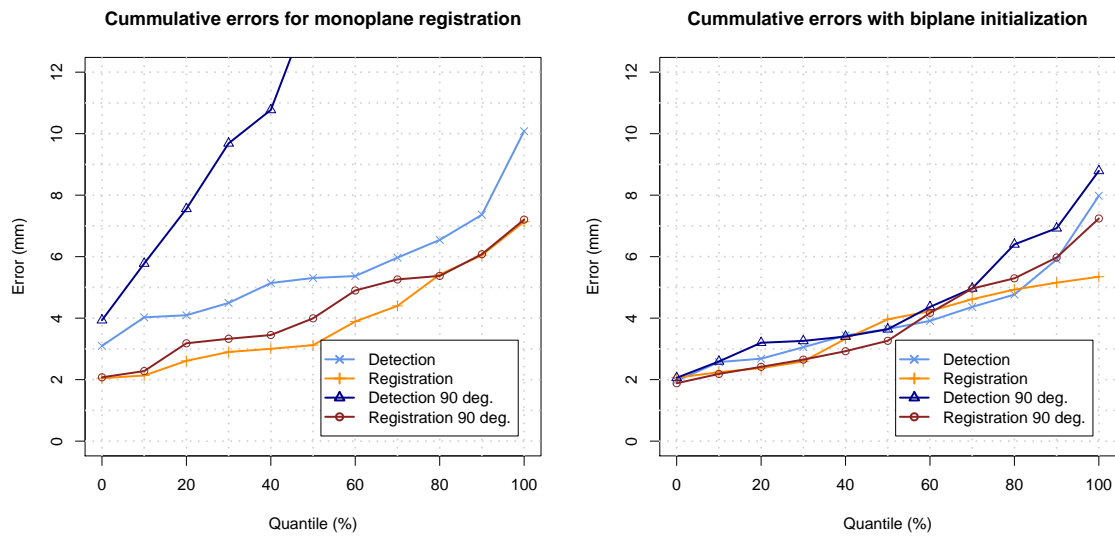


Figure 7.7: Evaluation of the detection and the registration results for monoplane and biplane probe pose estimation.

light blue curve shows the errors of the monoplane detection and the orange curve the monoplane registration which was started with the results of the previous detection. The detection shows a mean error of 5.53 mm while the registration improves this value to 3.86 mm. The dark blue curve shows the results of the detection from the perpendicular C-arm view. The mean error here is around 15.61 mm while the registration remains with an error of 4.25 mm, which is symbolized by the red curve. The results show that the post-registration clearly decreases the error of the detection by around 1.7 mm. The results for the registration improves about 11 mm for the perpendicular, but not re-registered view.

The results for the detections/registrations with an initial biplane initialization are shown in Figure 7.7 in the right graph. The colors of the curves indicate the same experiments as for the monoplane case described above. One can see that the detection accuracy (light blue curves) improves significantly, compared to the cases with no initialization. The mean error here drops to 3.97 mm which is an improvement of 1.67 mm. The greatest improvement of about 11.15 mm is shown for the monoplane detection results of the perpendicular view where the mean error is around 4.46 mm. The results are almost adapting the results from the first view. The registration shows also some improvement by biplane initialization. Around 1.57 mm to 3.97 mm for the first registration view and by 0.38 mm to 3.88 mm for the perpendicular view. An overview over the results is also given in Table 7.4.

All experiments were carried out on a notebook (Core i7, 2.20 GHz, 8 GB RAM) with a Nvidia Quadro 1000M (96 CUDA kernels, 700 MHz, 2 GB GPU RAM, CUDA compute capability 2.1). The runtime performance is shown in Table 7.5. It shows 385 ms/frame for the detection and 1423 ms/frame for the registration part.

The experiments were actually examined with the Ultrasound-fusion prototype which is the topic of the next Chapter 8.

	Monoplane	Biplane
Detection	5.53	3.97
Registration	3.86	3.72
Detection 90 degrees	15.61	4.46
Registration 90 degrees	4.26	3.88

Table 7.4: Mean values for all detection and registration 2D errors in mm.

	Mean time [s]
Detection	0.385
Registration	1.423

Table 7.5: Mean values for the runtime in seconds of the single parts of the algorithm.

7.4 Discussion & Conclusion

7.4.1 Discussion of Capture Range Estimation

The experiments to evaluate the capture range of the 2D-3D registration show that the registration algorithm is able to successfully use the detection results (Interval 1) as initialization. Almost every dataset (98.2%) showed a better registration accuracy than 3 mm. Intervals 2 and 3 showing a much higher rate on outliers. Therefore, the capture range decreases consequentially.

This behavior can be explained by the employed Subplex optimization algorithm (described in Section 4.5), which is a local optimizer. That means, the risk that the algorithm gets stuck in a local optimum is relatively high. An initialization far away from the ground truth position will result in a higher risk of ending up in a local optimum and a failed registration.

An explanation for the increasing numbers of outliers that occur also near to the ground truth position in interval 2 and 3 are the greater initial step sizes. It is necessary to choose greater initial steps to cover a greater search space. Otherwise the optimizer will remain in a very local area and will not evaluate the whole search space and will end up in a local optimum. On the other hand, this greater initial steps bear the risk that the optimizer misses a close ground truth position. One can try to overcome this local behavior with the implementation of a more global optimization approach. This was shown in [Kais14b] or in [Gong08] but with much slower runtime performance.

Nevertheless, the Subplex algorithm is sufficient for the registration in the presented pipeline because the detection algorithms provide parameter estimations which lie inside the boundaries of interval 1.

7.4.2 Discussion of Marker Target Registration Error

The results from Section 7.3.1 show that the detection is a good initialization for the registration. It clearly initializes the registration inside the capture range of the registration algorithm. It still needs to be shown if the registration improves the preliminary results significantly.

In the monoplane case, the registration shows a clear improvement compared to the detection results. This becomes significantly apparent while evaluating the parameters from the perpendicular view. The detection algorithm shows much higher errors for the out-of-plane parameters than the 2D-3D registration, especially for the depth parameter. This behavior is due to the nature of 2D-3D registration algorithms. They can adapt smaller changes in the image in more detail than template matching algorithms that have only a limited capacity of detection candidates. Despite this, the given accuracy is still sufficient for initializing the registration.

The results are slightly different for the experiments with a previous biplane initialization. First of all, the detection results are clearly improving. One can see that the results for the perpendicular view are almost equal to the results from the primary view. These results show the importance of the out-of-plane parameters, especially the depth parameter for the whole pose estimation pipeline. This results show that a clinical prototype probably needs a biplane initialization if high detection/registration accuracy is required.

It is noticeable that the other out-of-plane parameters pitch and roll are not showing such a big influence on the final pose estimation results like the depth. This can be explained that those three parameters are influencing each other. For example, if the depth was estimated incorrect and the probe appears too large in the projection image, this can also be compensated with a small rotation around the pitch. While keeping the depth in an almost correct estimation, this wrong compensation is not possible anymore. The only parameters which still remains out-of-plane is the roll. One would need a top-down view to the probe to overcome this last source of error. This is not possible due to the way how the probe is inserted into the patient. This is one reason that the pose estimation is not showing better results than 3.7 mm in the mean.

While comparing the detection to the 2D-3D registration, one can see that the registration still improves the detection estimation. However, the detection is almost on a similar level of accuracy. The registration algorithm still shows a better handling of outliers which is recognizable in the range above the 80th percentile in Figure 7.7. The accumulated errors for the detection are growing faster than for the registration. That means that outliers from the detection estimation are corrected by the registration.

Finally, a physician who would use the prototype with the described pipeline would have to deal with a target registration error around 4 mm. More error sources have to be taken into account in a final product, for example the calibration error of $C_{US \rightarrow Model}$, which can be different for each imaging mode of the Ultrasound probe (zoom level, field-of-view, frame rate, etc.) and the factor how accurate and reproducible the points could be set in the Ultrasound volume. Those error sources have not been considered in the presented pipeline or have been approximated by constant values. The C-arm projection matrix \mathcal{P} was approximated by an ideal matrix for

each view angle. Compared to the results from Section 6.3 where smaller errors are reported, the errors are most likely arise from the whole pipeline and not exclusively from the detection/registration algorithms.

The evaluation of the runtime performance of the particular parts shows that the detection is capable for real-time processing, even on a low performance laptop. However, the registration requires more time for a proper execution. Because of that reason, the prototype was developed in a way that the 2D-3D registration is used for high accuracy results on the last frame of a fluoro sequence after the physician stopped the live X-ray stream. For live probe pose estimation during fluoroscopic imaging only the detection algorithms are used.

Prototype for Fusion of Interventional Ultrasound and X-ray

8.1 Features of the Clinical Prototype.	92
8.2 Workflow.	93
8.3 Clinical Setup.	95
8.4 Clinical Application.	95
8.5 Conclusion.	97

The previously described work forms the algorithmic framework to set up a prototype for Ultrasound and X-ray fusion for the use in a real clinical environment. The main reason to develop a clinical prototype was to receive valuable feedback from physicians for development. Good feedback is typically provided when a system is used under real circumstances in a hospital. A prototype will also show the clinical benefit of the new system and is commonly the first step for releasing a new medical product. Additional feedback will be provided on the usability and the possible workflow. The heart of this prototype is the automatic detection/registration algorithm which is described in Chapter 7. Based on the ability to estimate the TEE probe position in a 3D space, several prototype features could be developed that can provide useful tools to physicians.

The prototype consists of three parts. The first part is running on the X-ray side which is mainly handling the registration of the TEE probe and overlays on the X-ray image. The second part is located on the Ultrasound machine and provides a user interface for the sonographer. The third part is the connection between both systems to exchange image and overlay information.

The complete prototype was a joined work between multiple people from multiple business units and departments of Siemens Healthcare, namely Angiography and X-ray, Ultrasound and Corporate Technology. The software infrastructure was mainly developed by Corporate Technology. The following chapter will describe the features of the prototype, how it was set up in a clinical environment for animal experiments and how it was used by the physicians.

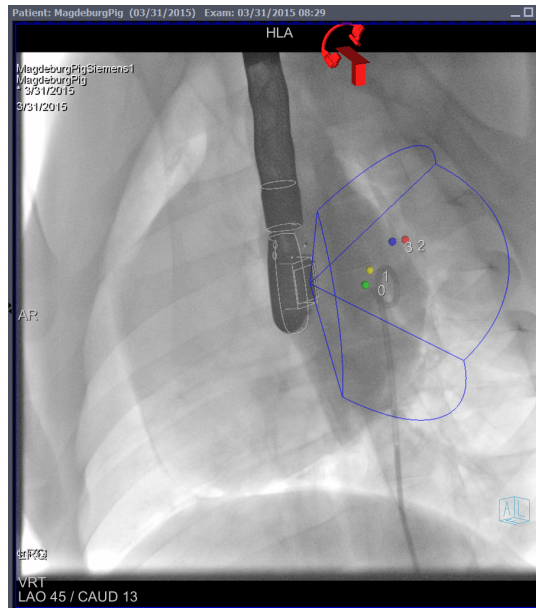


Figure 8.1: Screenshot of the clinical prototype during an animal experiment.

8.1 Features of the Clinical Prototype

The Ultrasound & X-ray fusion prototype is providing several tools to the physicians which can be helpful to improve their workflow in the operating room. The basis for those correctly working tools is an accurate registration of the TEE probe. It would make no sense to use any of the implemented features without a precisely known probe position. The prototype includes the following features.

Display Ultrasound Cone If the TEE probe is successfully registered, the prototype will overlay the borders of the current Ultrasound image – the Ultrasound cone – on the X-ray image. This will provide a better impression on how the Ultrasound is emerging from the TEE probe and how it is orientated relative to the X-ray image and to other instruments navigated by the physician within the patient. This can be very helpful to locate and identify inserted catheters in the Ultrasound image and to control them properly. An example is shown in Figure 8.1. In this image, the Ultrasound machine is currently recording a live 3D volume. The borders of this volume are marked by the blue wireframe that emerges from the TEE probe. The white structures are overlaid from the registered TEE probe model and provide a quick confidence check for the user if the probe was successfully registered.

Marker Placement One of the most powerful features is the possibility for the user of the Ultrasound machine to place markers within a volumetric Ultrasound image. These markers are then sent with the current registration over to the X-ray machine and are overlaid on the X-ray image. Figure 8.3 shows how the sonographer sets the marker points on the Ultrasound machine. Figure 8.2 shows a screenshot of the prototype on the Ultrasound machine. The set points are visible in the Ultrasound cut plane views. If all necessary markers are set and a registration of the TEE probe

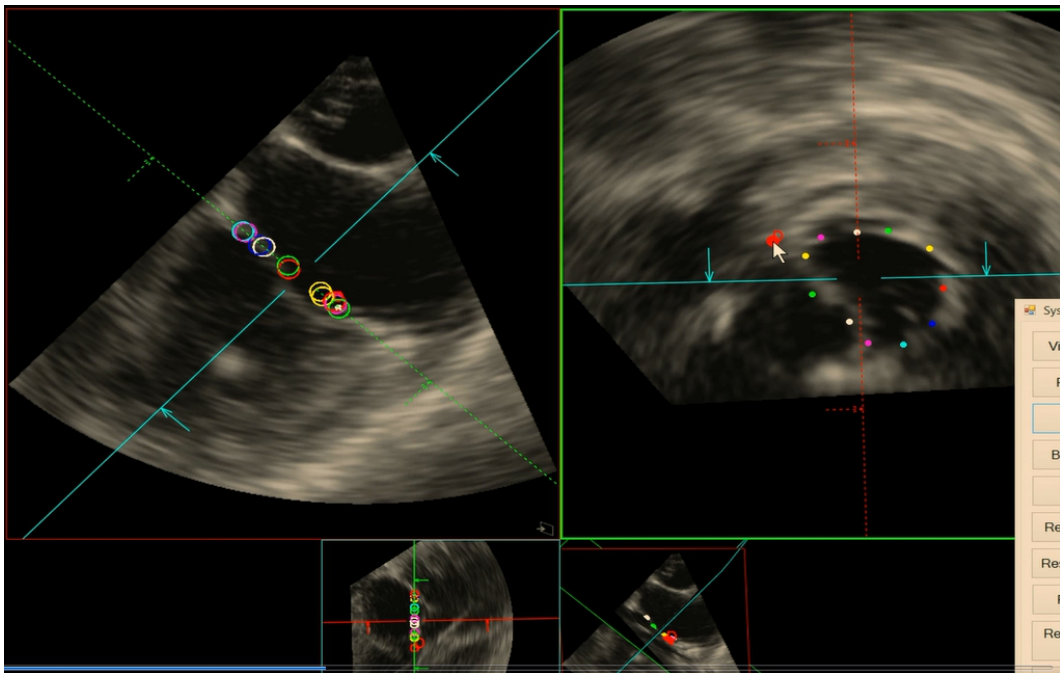


Figure 8.2: Screenshot of the user interface of the prototype on the Ultrasound machine during setting of marker points.

in the X-ray image is established, the markers can then be sent over to the X-ray machine and are overlaid on the fluoroscopic X-ray image. This is shown in Figure 8.4. Once the markers are sent to the X-ray system, they will remain fix in the table coordinate system. That means, even if the probe, the C-arm or the patient table are moved, it will not influence the position of the markers relatively to the table. However, organ or patient motion is not compensated yet.

Valve Overlay Another feature of the prototype is to overlay heart valve models of the mitral and the aortic valve which are directly segmented and modeled from an Ultrasound volume. The detection and modeling of the valves is done by another Ultrasound application which is connected to the fusion prototype. The fundamental techniques that are necessary for the heart valve segmentation are described in [Iona 09, Iona 10, Noac 13]. An example of such an overlay is shown in Figure 8.5.

8.2 Workflow

During the clinical animal studies, the following workflow for using the prototype turned out to be most useful. To establish a good registration of the TEE probe, it is necessary to have a biplane initialization. This leads to the approach that the physician has to rotate the C-arm for at least 30 degrees after recording the first image from the main view angle. A second X-ray image is acquired and a biplane registration is performed. These parameters are then taken as a depth constraint. If the probe is registered properly, the sonographer can set markers in the Ultrasound image and can then send it over to the C-arm system. During this step, it is important that

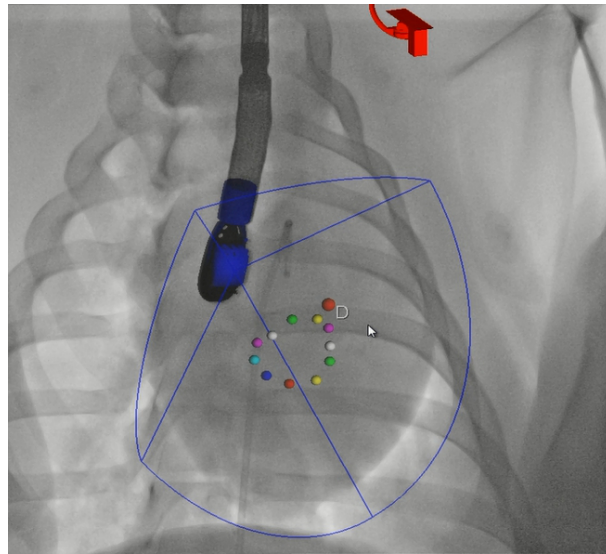
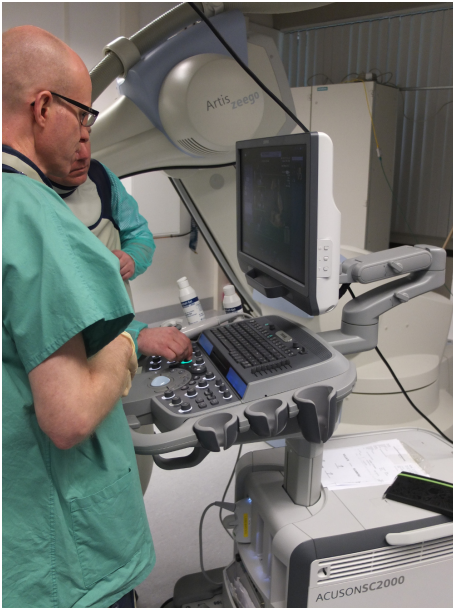


Figure 8.3: Sonographer during setting marker points.

Figure 8.4: The markers from Figure 8.2 are overlaid in the fluoroscopic X-ray image.

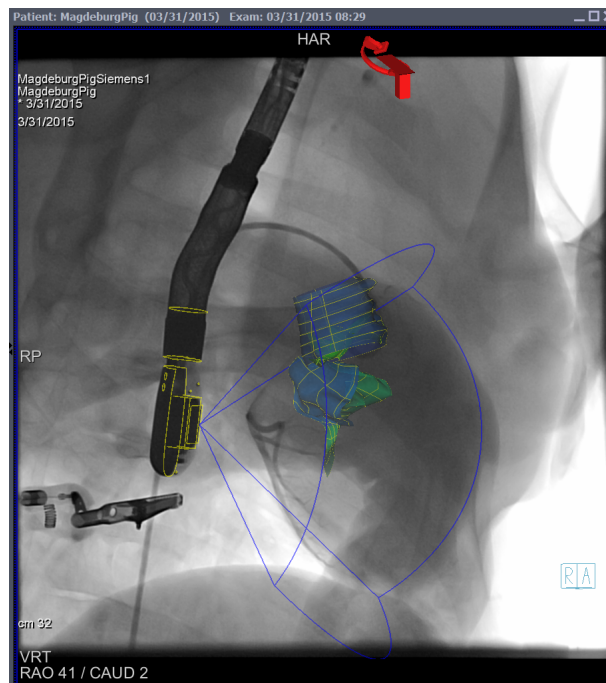


Figure 8.5: The segmented aortic valve (upper) and mitral valve (lower) are overlaid on the X-ray image.

the TEE probe moves as least as possible. Any motion can disturb the established registration and, therefore, the accuracy of the overlaid landmarks.

8.3 Clinical Setup

The prototype was set up in an animal lab (Experimentelle Fabrik, University of Magdeburg) which was equipped with an Artis zeego (Siemens Healthcare, Forchheim, Germany) and an SC 2000 Ultrasound machine with a transesophageal echo probe (Siemens Healthcare, Mountain View, CA, USA). Figure 8.6 is offering an insight into the animal lab. The arrangement of the devices corresponds to a common setup of a clinical hybrid operating room. The pig is positioned on the table and the C-arm's angulation provides a good view on the pig's heart. The Ultrasound machine is positioned at the table head because the TEE probe was placed into the pig's esophagus. One can see the large display on the right which provides all necessary information for the cardiologists who are standing on the left side of the table. The Artis Large Display (Siemens Healthcare, Forchheim, Germany), which is shown in Figure 8.7 in detail, mirrors three different screens. Firstly, the standard live fluoroscopic X-ray image (a), then the Ultrasound fusion prototype with the overlaid Ultrasound cone and the placed markers (b), and finally the screen of the Ultrasound device how it is shown to the sonographer (c). Additional information about the C-arm system is provided as well.

The prototype software for registration and overlay was running on a dedicated laptop which was connected to the Ultrasound machine and the C-arm system. The information from the second prototype software on the Ultrasound machine, for example marker points and the Ultrasound cone geometry, was sent to the laptop over a network interface. The prototype did not have the ability to send real Ultrasound images. The X-ray images from the C-arm system were accessed with a frame grabber which was connected to the X-ray machine. The laptop was additionally connected to the internal C-arm message bus to gather necessary C-arm information like C-arm angle, image size, zoom and other.

8.4 Clinical Application

Two animal experiments have been carried out to test the prototype and its workflow and to obtain clinical feedback. The experimental team was composed of physicians of different medical professions, for example cardiologists, heart surgeons and anesthesiologist and technical staff members from the University Hospital Magdeburg and developers of the prototype. The main challenge was to improve and to evaluate the workflow under real conditions. Secondly, it was important to evaluate the concept and the clinical accuracy of setting the marker points.

A real use case was executed by the implantation of a TAVI (see Section 2.3.1 for more information on the medical background). For this procedure, it is important to adjust the C-arm view angle in a way that the operator has an orthogonal view to the aortic valve annulus. Commonly, this specific angle is determined by a preoperative CT or with C-arm CT during the intervention with the support of a special software



Figure 8.6: Overview of the setup of the lab during an animal experiment.

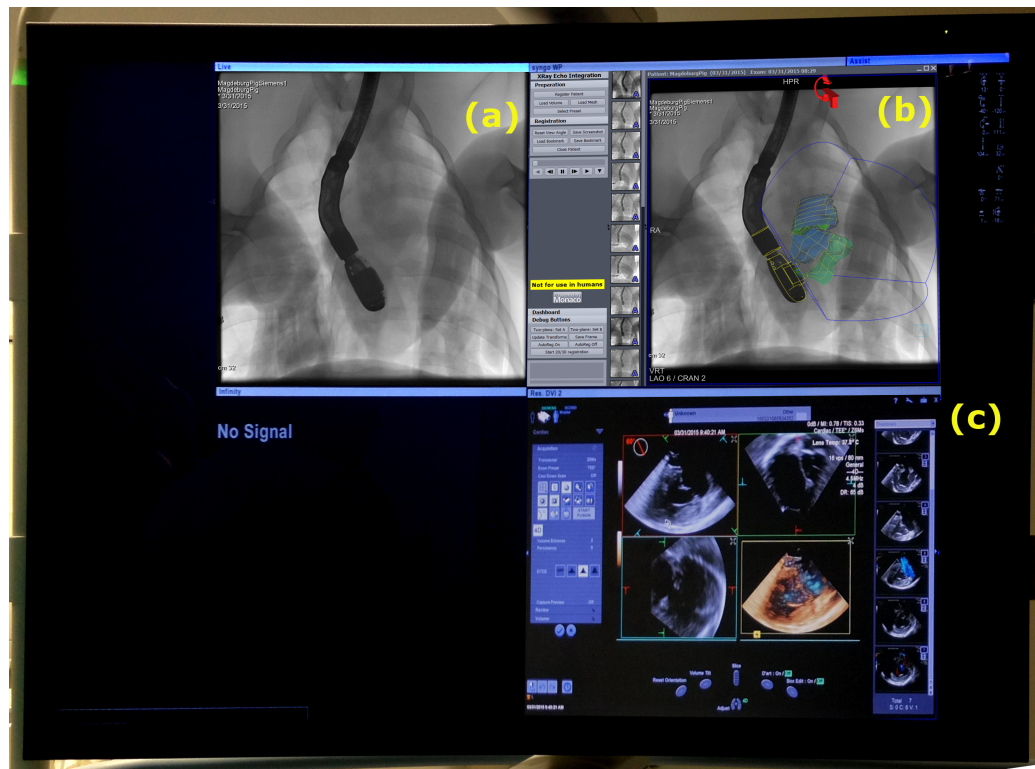


Figure 8.7: Screenshot of the Artis Large Display which shows all image information in parallel during the animal experiment.

[John 10a]. With the help of the new fusion prototype, the physicians tried to avoid an acquisition of a 3D CT while marking the valve's annulus in the live 3D Ultrasound image and overlaying it to the fluoroscopic images. An example can be seen in Figure 8.4. Due to the functionality that the markers are fixed in table coordinates, the physicians were able to rotate the C-arm to the required position. Speaking in terms of the overlaid markers, the ring structure collapsed into a line in an orthogonal view. Furthermore, this highlighted structure served as an orientation where the artificial aortic valve had to be positioned. The used artificial valve (Edwards Sapien, Edwards Lifesciences Corporation, Irvine, CA, USA) should be placed in the middle of the annulus which was highlighted by the marked ring. Figure 8.8 shows the situation right before implantation.

8.5 Conclusion

The feedback after the first animal experiments was very positive and promising. The registration/detection algorithms worked stably and reliably and provided the physicians an useful tool. The implemented functionality worked as expected and was very well accepted.

It turned out that the physicians favored to mark important structures like the aortic valve annulus as target points for the C-arm rotation or for better catheter navigation. The physicians were very optimistic that the Ultrasound fusion software can help them on saving lots of contrast agent, because soft tissue structures can now

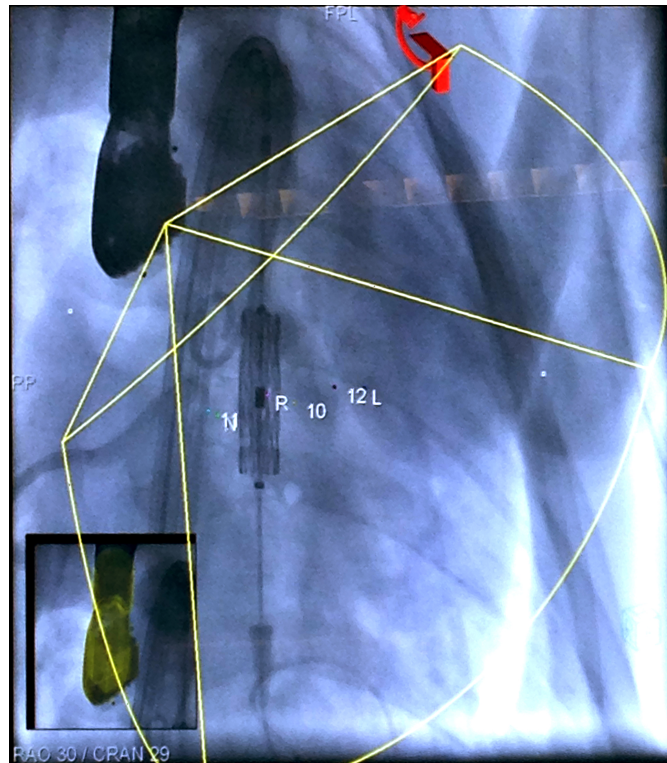


Figure 8.8: Screenshot from a TAVI procedure during an animal experiment.

be made permanently visible through the markers. It can also be possible to get rid of preoperative CT acquisitions just for angulation planing, e.g. for TAVI procedures. This CT can be replaced by the live marking and overlay of the marked annulus.

It was strongly wished by the physicians that the software can provide motion tracking of anatomical landmarks. For example, if a part of the heart is marked in the Ultrasound image, this marker should than be continuously tracked in Ultrasound and shall be updated in the X-ray image according to the heart or patient motion.

Summary and Outlook

9.1 Summary	99
9.2 Outlook	101

9.1 Summary

The introduction of new catheter devices and the improved imaging modalities enabled the development of new innovative minimal invasive heart surgery. More and more conventional heart surgery techniques were adapted to catheter-based minimal invasive interventions during the last years. This trend led to the development of the hybrid operation room, a combination of a catheter laboratory, equipped with a C-arm system for fluoroscopic X-ray, and a common operation room. Many of the modern minimal invasive interventions are carried out under the guidance of X-ray and Transesophageal Echocardiography. This thesis addressed the question if a fusion of both systems can provide more and better accessible information and especially how it can technically be accomplished.

Chapter 2 explains the medical background and the possible benefit of such a fusion system in detail. Especially catheter-based minimal invasive interventions for the treatment of structural heart disease, for example mitral valve repair, aortic valve implantation, atrial septal defect closure or heart appendage closure, need the support of X-ray and TEE guidance. A literature overview about the fusion of X-ray fluoroscopy and Ultrasound is presented in Chapter 3. Different research groups tried to establish an image fusion with different methods and tools, while the basic registration practice is similar. No research group is trying to register the images directly, which is almost impossible because of the absolutely different image impression and information of both modalities. The commonly used indirect method is to estimate the TEE probe pose in the X-ray image with the help of a TEE probe model and to establish an indirect registration via the calibration of Ultrasound to that model. It is also shown which different kind of interventional Ultrasound devices are fused with X-ray.

In this thesis, the registration of the TEE probe is done with a 2D-3D image based registration algorithm, which is a well known technique in medical image processing. Chapter 4 describes the three main parts of a 2D-3D registration pipeline which are 1) the DRR generator, which generates artificial X-ray images from a given model, mostly a volumetric image, from different viewpoints, 2) a similarity measure that

compares the DRRs to a real X-ray image which contains the searched object, and 3) the optimization algorithm, which controls the process of new parameter estimation.

In the following chapters, each part of a 2D-3D registration is analyzed. New approaches are presented, which can also be used for general 2D-3D registration problems and not solely for the task of TEE probe pose estimation. The basic pipeline, which is used in this work, consists of a volume-based ray-casting DRR generator which is optimized for fast parallel GPU processing with CUDA. The same applies for the employed similarity measures. Normalized cross correlation and normalized gradient fields are implemented in CUDA for a fast calculation of the similarity between DRR and original X-ray image. A model of the probe for the DRR generator was generated from a Micro-CT, recorded with an industrial Micro-CT scanner, with additional manual post-processing, for example metal artifact removal. The employed optimization algorithms are Powell-Brent and Subplex. Important for the evaluation of the registration algorithm is an exact ground truth transformation for the used datasets which is hard to achieve on clinical data. The best practice was to establish a ground truth registration by careful manual registration from different C-arm views on a fixed probe with a dedicated tool.

Another issue is that an X-ray image is a 2D projection image. Therefore, it is more difficult to estimate parameters that are out-of-plane, namely depth, pitch and roll, which means they transform the probe into directions which are outside of the image plane. Estimating those parameters is more error-prone than searching for inplane parameters. In a clinical workflow, one will handle this drawback by acquiring another image from a different C-arm angle. The best case is to acquire the second image from a perpendicular view, which means rotating the C-arm by 90 degrees. This can be very hard to achieve in an operation room. A good compromise is to rotate the C-arm with a smaller offset, for example 45 degrees. With the commonly used registration algorithms one will run into problems while registering on both images simultaneously. A movement of the probe in one image will destroy the established registration in the other and vice versa. Chapter 5 introduces the method of planar parameters which avoids such a behavior. While registering on one view in a biplane setup, the out-of-plane parameters are kept invariant while only inplane parameters are changed in a way that they are not disrupting the established inplane result in the other view. This is achieved by restricting the possible movement to a spanned plane between both C-arm views. The usefulness of this method is shown for automatic and for manual 2D-3D registration on multiple views.

One big drawback of 2D-3D methods is the relatively slow runtime performance, which is due to the bottleneck of DRR generation by the common volume ray-casting based generation approaches. Chapter 6 introduces an approach to speed up this time consuming part. The ray-casting DRR generation is substituted by fast rendering of a triangular mesh. An isovalue algorithm was used to generate a triangular mesh from the TEE probe model. The shape diameter function was used to color the mesh with regard to the thickness of the probe. The DRR was then generated by rendering the mesh with alpha blending. Due to the different color, one can achieve an image which is very similar to an X-ray image. Potential differences between volume-based and mesh-rendered DRRs are suppressed by the employed gradient

based similarity measure. The runtime performance is highly improving while the registration accuracy is not changed.

It is shown in Chapter 3 that different methods were developed to estimate a pose of a TEE probe. Chapter 7 presents how to connect two different methods, a detection and a registration approach, to use the advantages of both systems. Commonly, detection algorithms are fast but not as accurate as 2D-3D registration methods. On the other hand, 2D-3D approaches usually have a much slower runtime performance. Another drawback is the small capture range of these methods, which means that they must be initialized closely to the ground truth to achieve a correct result. It is shown in this chapter how to use fast detection methods to provide a good initialization for the following registration algorithm. With this combination, it is possible to quickly initialize the 2D-3D registration inside its capture range. The evaluation of this pipeline was done with a realistic marker target error. Structures in Ultrasound have been marked and were overlaid to the X-ray image according to the established registration. The results show an improved accuracy over exclusive detection and an improved capture range. The mean accuracy is below 4 mm and the runtime tends to be real-time.

Finally, Chapter 8 describes the workflow and the features of the developed prototype for fusion of Ultrasound and X-ray and how it was used in a clinical environment during animal experiments. The physicians gave very promising feedback and were very optimistic that the employed system can improve their clinical workflow and can help them to save on X-ray dose and especially on contrast agent.

9.2 Outlook

The concepts and methods discussed in this thesis led to a clinical prototype which shows very promising results. Currently, the product implementation is in progress by Siemens Healthcare. The presented technical contributions can also improve other 2D-3D registration approaches in general. Remaining and upcoming technical and clinical challenges and topics are discussed in the following.

Hardware Improvements A real-time performance of a 2D-3D registration is still hard to achieve. Usually, it is possible on low framerates. Future hardware improvements, especially for GPU technologies, can help to solve those performance issues and enable these kind of algorithms for realtime applications in general.

New Methods for 2D-3D Registration Even 2D-3D registration is a well known technique and is employed in many clinical systems, recently proposed methods can help to improve registration quality and performance in general. Examples are algorithms which employ a Generalize Hough Transformation (GHT) [Varn 13a]. Another example is registration in combination with regression learning techniques [Chou 13, Gouv 12]. The authors reported higher robustness and a higher performance by slightly lower accuracy for their approaches. In recently published research [Miao 16], the authors used a regression technology based on Convolutional Neural Network (CNN) for 2D-3D registration which could be used for real time registration.

They showed improved registration performance and capture range, also for data of TEE probe registration.

Another subject of research is the automatic verification of registration results [Varn 13b, Varn 15]. It will probably improve clinical acceptance if a system can automatically decide if a registration is successful or not. A physician could be completely released by interacting with the system and could fully concentrate on the clinical workflow.

Image to Image Fusion The most important feature for the physicians is the ability to mark landmarks in Ultrasound and overlay them in live X-ray. This is already implemented in the current prototype. Nevertheless, it could be also useful to overlay real Ultrasound image data on X-ray images. Additional post-processing will be necessary to generate an overlay which is useful and provides an additional benefit. If one would just overlay the Ultrasound volume, one will probably see neither the X-ray nor the Ultrasound image.

Motion Compensation In the current prototype, the placed landmarks are static and are not updated according to organ or patient motion. Therefore, a physician needs to visually interpolate the underlying motion or has to set multiple landmarks. One of the biggest future challenges is to provide a real-time motion compensation which is based on Ultrasound images. Such a system would have the ability to model and display the heart anatomy live on X-ray. If this could be reliably done, this would have a great impact on the clinical workflow. A first promising approach to track the heart's anatomy within 3D data in realtime is shown in [Voig 15].

List of Symbols

α	C-arm rotation around cranial-caudal axis	6
Δr	Size of a voxel	35
δ	Distance between overlaid 2D marker to its ground truth position	82
ϵ	Regularization condition	38
γ	C-arm rotation around left-right-anterior-oblique axis	7
κ	Normalization coefficient	35
λ	Normalization coefficient	35
\mathcal{C}	C-arm rotation matrix	30
\mathcal{I}	Measured intensity at the detector	33
\mathcal{I}_n	Intensity mapped to a pixel	35
\mathcal{I}_T	Emitted intensity from X-ray tube	33
\mathcal{P}	C-arm projection matrix	18
\mathcal{P}'	Projection matrix	30
\mathcal{R}	Registration matrix	28
μ	Attenuation coefficient	33
μ_i	Intensity value of a voxel	35
\bar{I}	Mean value of image pixel values	38
$\phi_{yaw}, \phi_{pitch}, \phi_{roll}$	Planar rotational parameters	54
ψ	Projection error	50
σ	Standard deviation of image pixel values	38
$\theta_{pitch}, \theta_{yaw}, \theta_{roll}$	Rotational parameters	30
A	Object in 3D space	50
a	Alpha value	70
A_T	Object in 3D space transformed by T	50

A_{Proj}	Projection of object A	50
A_{TProj}	Projection of object A_T	50
c, c'	Base vectors	54
C_0	Pixel color	70
c_A, c_B	Projections of the centerline vector c'	56
C_V	Vertex color	70
c_{3D}	Point on the centerline vector	55
$cm_{\mathcal{P}}$	Projected centerline vector	55
$cm_{\mathcal{P}}^y$	Y component of the point $cm_{\mathcal{P}}$	55
D	Set of search directions	40
e	Vector from <i>eye</i> to an object's rotation center	54
<i>eye</i>	Focal point	54
f, f'	Base vectors	54
G_x	Vertical gradient image	37
G_y	Horizontal gradient image	37
I_1	X-ray image	37
I_2	DRR image	37
I_A	Image plane A	56
I_B	Image plane B	56
I_{DRR}	DRR image	28
I_{Xray}	X-ray image	28
L_i	Line between a registered point and its associated ground truth point .	45
m	Magnification factor	30
m_{3D}	Rotation center of an object	54
n_A, n_B	Normal vectors of a plane P_A or P_B	57
n_{ϵ}	Pixel gradient	38
p	Pixel spacing	30
P_{GT}	Set of 3D points at ground truth position	44

p_{GT}	3D point at ground truth position	44
P_{Reg}	Set of 3D points after registration	44
p_{Reg}	3D point after registration	44
px	Pixel	31
S	Set of rigid transformation parameters	28
s, s'	Base vectors	54
sim	Similarity measure function	28
sz	Image size	30
T	Transformation matrix	18
t	Material thickness	33
t_x, t_y, t_z	Translational parameters	30
T_θ	Transformaton matrix covering rotation around one angle	54
$T_{translation}$	Transformation matrix covering translational parameters	54
SID	Source Image Distance	28
SOD	Source Isocenter Distance	28
ASD	Atrial Septal Defect	12
CAUD	Caudal	30
CMA-ES	Covariance Matrix Adaptation - Evolution strategies	40
CRAN	Cranial	30
CT	Computer Tomography	1
CVD	Cardiovascular Disease	5
CVD	Conditional variances of differences	37
DOF	Degrees of freedom	18
DRR	Digitally reconstructed radiograph	18
ED	Entropy of differences	37
EM	Electromagnetic (tracking)	22
fps	frames per second	21
GC	Gradient correlation	37

GD	Gradient differences	37
GHT	Generalize Hough Transformation	101
GPGPU	General Purpose Computation on Graphics Processing Unit	65
GPU	Graphics processing unit	21
ICE	Intra-cardiac Echocardiography	23
IVUS	Intravascular Ultrasound	24
LAAC	Left atrial appendage closure	13
LAO	Left anterior oblique	30
MRI	Magnetic Resonance Imaging	1
NCC	Normalized cross correlation	37
NGF	Normalized gradient fields	37
NMI	Normalized mutual information	37
OR	Operation Room	6
PCA	Principal component analysis	21
PD	Projection Distance	44
PFO	Patent Foramen Ovale	12
PI	Pattern intensity	37
PVL	Paravalvular Leak	13
RAO	Right anterior oblique	30
RPD	Reprojection Distance	44
SAD	Sum of absolute differences	37
SBDX	Scanning-beam digital X-ray	21
SCV	Sum of conditional differences	37
SDF	Shape Diameter Function	68
SHD	Structural Heart Disease	5
SSD	Sum of squared differences	37
TAVI	Transcatheter Aortic Valve Implementation	10
TEE	Transesophageal Echocardiography	1

List of Symbols

TRE	Target Registration Error	43
TTE	Transthoracic Echocardiography	7
VD	Variance of differences	37
WHGD	Weighted histogram of gradient directions	37

List of Figures

2.1	C-arm of type Artis zeego.	7
2.2	Angles of a C-arm system with anatomical terms.	8
2.3	A TEE probe like it is used in a clinical environment.	8
2.4	Schematic visualization of the performance of a transesophageal echocardiography.	9
2.5	Schematic drawing of a TAVI procedure.	11
2.6	Ideal way of the catheter during a MitraClip procedure.	12
2.7	The MitraClip device by Abbott Vascular.	12
2.8	Device closure for Atrial Septa Defect.	12
2.9	Drawing of the Watchman implant residing in the left atrial appendage.	13
2.10	Screenshot of the EchoNavigator software by Philips.	15
3.1	General workflow of Ultrasound to X-ray registration	17
3.2	Literature overview for Ultrasound and X-ray fusion.	19
3.3	Example of an ICE catheter with implemented ball markers at the catheter tip.	24
3.4	Screenshot of the application IVUSmap by Siemens Healthcare.	25
4.1	TEE probe with six degrees of freedom and the C-arm's projection geometry.	28
4.2	General workflow of a 2D-3D registration algorithm.	29
4.3	Schematic drawing of the projection geometry of a C-arm.	31
4.4	Example of different characteristics of inplane and out-of-plane parameters.	32
4.5	Volume rendering of the Mirco-CT of the TEE probe.	33
4.6	Examples for symmetric probe projection images under completely different probe rotations.	34
4.7	One slice of the reconstructed 3D volume with the applied mask for removing metal artifacts.	34
4.8	Different transfer curves and corresponding DRRs.	36
4.9	Example of an image mask.	39
4.10	Basic principle of Powell's method.	41
4.11	All types of simplex movements.	42
4.12	Optimization strategy for TEE probe registration.	43
4.13	Visualization of used error measures.	44
4.14	Positions where errors are measured.	45
4.15	Screenshot of the annotation tool for generating a ground truth registration of TEE probe poses.	46
4.16	Exemplary X-ray images with the TEE probe fixed in a box with 1mm diameter metal ball markers, indicated by the white arrows.	48

4.17	Comparison of the accuracy of overlaid marker points.	48
5.1	Illustration of the rotation angles observer problem while translating an object under projective geometry.	50
5.2	Illustration of the problem of the observed yaw rotation while translating a cylindrical object which is rotated around the pitch.	50
5.3	Inplane and planar approach of registering an object on two reference images.	52
5.4	Definition of planar parameters.	53
5.5	Schema for multiplane transformation.	56
5.6	Examples of a multiplane scene.	59
5.7	Detailed registration runtime performances on a mono-oblique system.	60
5.8	Detailed registration accuracy performances on a mono-oblique system.	61
5.9	Example result for registration on data with probe movement.	62
6.1	Exemplary comparison between a ray-casting DRR and a DRR based on mesh-rendering from the same point of view.	66
6.2	Exemplary comparison between a ray-casting DRR and a DRR based on mesh-rendering from another view.	67
6.3	Screenshot of the TEE probe mesh opened in Blender.	68
6.4	Illustration of the working principle of the Shape Diameter Function.	69
6.5	Result of the Shape Diameter Function applied to the TEE probe mesh with additional manual post-processing.	69
6.6	Comparison between registration with ray-casting DRRs and mesh-rendered DRRs for the mTRE and the mRPD error metric for mono-plane registration.	71
6.7	Comparison between registration with ray-casting DRRs and mesh-rendered DRRs for the mTRE and the mRPD error metric for biplane registration.	71
6.8	Plot of start and end mTRE comparison of all biplane registrations.	72
6.9	Comparison between registration with ray-casting DRRs and mesh-rendered DRRs for all six degrees of freedom.	73
6.10	Comparison of runtimes per registration of ray-casting and mesh-based DRR generation for monoplane and biplane registrations.	75
7.1	Complete detection-registration-pipeline for probe pose estimation.	78
7.2	Results for the capture range experiment.	81
7.3	The multimodal phantom.	83
7.4	Setup of the phantom experiment which was used to evaluate the detection-registration pipeline.	84
7.5	Example for overlaid marker points.	85
7.6	Overview over some used X-ray images from different C-arm angles.	86
7.7	Evaluation of the detection and the registration results for monoplane and biplane probe pose estimation.	87
8.1	Screenshot of the clinical prototype during an animal experiment.	92

8.2	Screenshot of the user interface of the prototype on the Ultrasound machine during setting of marker points.	93
8.3	Sonographer during setting marker points.	94
8.4	The markers from Figure 8.2 are overlaid in the fluoroscopic X-ray image.	94
8.5	The segmented aortic valve and mitral valve are overlaid on the X-ray image.	94
8.6	Overview of the setup of the lab during an animal experiment.	96
8.7	Screenshot of the Artis Large Display which shows all image information in parallel during the animal experiment.	97
8.8	Screenshot from a TAVI procedure during an animal experiment.	98

List of Tables

2.1	Comparison of different properties of the two imaging modalities. . .	6
3.1	Overview over results for the different approaches presented in the literature.	20
5.1	Mean success and runtime results for the mono-oblique setup.	60
5.2	Mean success and runtime results for the double-oblique setup.	60
5.3	Mean success and runtime results for data with probe movement. . .	61
5.4	Summarized results with standard deviation over all users and scenes.	62
6.1	Mean values of parameter errors of successful monoplane registrations for the mesh and the DRR approach.	72
6.2	Mean values of parameter errors of successful biplane registrations for the mesh and the DRR approach.	73
6.3	Comparison of runtimes in milliseconds for the DRR or mesh generation and the evaluation of the similarity measure for different resolutions.	74
6.4	Runtime for volume-based and mesh-based approach for mono-and biplane registrations in seconds.	74
7.1	Boundaries for the 2D-3D registration algorithms based on detection accuracy.	79
7.2	All boundaries/parameter intervals for the capture range estimation experiment.	80
7.3	C-arm angulations of all acquired and annotate X-ray images that were used for evaluation.	83
7.4	Mean values for all detection and registration 2D errors in mm.	88
7.5	Mean values for the runtime in seconds of the single parts of the algorithm.	88

List of Algorithms

4.1	Powell-Brent optimizer.	40
5.1	General biplane registration approach.	52
5.2	General registration approach for decoupled biplane registration.	58

Bibliography

- [Abbo 15] Abbott Vascular. *MitraClip System*. 2015. http://www.abbottvascular.com/content/dam/av/abbottvascular/images/Structural_heart/full.png, last checked: 21 February 2016.
- [Adel 84] E. H. Adelson, C. H. Anderson, J. R. Bergen, P. J. Burt, and J. M. Ogden. “Pyramid methods in image processing”. *RCA engineer*, Vol. 29, No. 6, pp. 33–41, 1984.
- [Aoua 08] S. Aouadi and L. Sarry. “Accurate and precise 2D-3D registration based on X-ray intensity”. *Computer Vision and Image Understanding*, Vol. 110, No. 1, pp. 134 – 151, 2008.
- [Aruj 14] A. Arujuna, R. Housden, Y. Ma, R. Rajani, G. Gao, N. Nijhof, P. Cathier, R. Bullens, G. Gijssbers, V. Parish, S. Kapetanakis, J. Hancock, C. Rinaldi, M. Cooklin, J. Gill, M. Thomas, M. O’neill, R. Razavi, and K. Rhode. “Novel System for Real-Time Integration of 3-D Echocardiography and Fluoroscopy for Image-Guided Cardiac Interventions: Preclinical Validation and Clinical Feasibility Evaluation”. *Translational Engineering in Health and Medicine, IEEE Journal of*, Vol. 2, pp. 1–10, 2014.
- [Ball 81] D. Ballard. “Generalizing the Hough transform to detect arbitrary shapes”. *Pattern Recognition*, Vol. 13, No. 2, pp. 111 – 122, 1981.
- [Barr 04] J. F. Barrett and N. Keat. “Artifacts in CT: Recognition and Avoidance”. *RadioGraphics*, Vol. 24, No. 6, pp. 1679–1691, 2004.
- [Bart 13] K. Bartus, F. T. Han, J. Bednarek, J. Myc, B. Kapelak, J. Sadowski, J. Lelakowski, S. Bartus, S. J. Yakubov, and R. J. Lee. “Percutaneous Left Atrial Appendage Suture Ligation Using the LARIAT Device in Patients With Atrial Fibrillation Initial Clinical Experience”. *Journal of the American College of Cardiology*, Vol. 62, No. 2, pp. 108–118, 2013.
- [Biag 15] P. Biaggi, C. Fernandez-Golfín, R. Hahn, and R. Corti. “Hybrid Imaging During Transcatheter Structural Heart Interventions”. *Current Cardiovascular Imaging Reports*, Vol. 8, No. 9, 2015.
- [Birk 03] W. Birkfellner, J. Wirth, W. Burgstaller, B. Baumann, H. Staedele, B. Hammer, N. C. Gellrich, A. L. Jacob, P. Regazzoni, and P. Messmer. “A faster method for 3D/2D medical image registration – a simulation study”. *Physics in Medicine and Biology*, Vol. 48, No. 16, p. 2665, 2003.
- [Birk 05] W. Birkfellner, R. Seemann, M. Figl, J. Hummel, C. Ede, P. Homolka, X. Yang, P. Niederer, and H. Bergmann. “Fast DRR Generation for 2D/3D Registration”. In: J. Duncan and G. Gerig, Eds., *Medical Image Computing and Computer-Assisted Intervention – MICCAI 2005*, pp. 960–967, Springer Berlin Heidelberg, 2005.
- [Blau 13] Blausen.com staff. *Device Closure for Atrial Septal Defect*. Wikiversity Journal of Medicine, 2013. https://en.wikipedia.org/wiki/File:Blausen_0069_AtrialSeptalDefect_02.png, last checked: 21 February 2016.

- [Blen 14] Blender Online Community. *Blender - a 3D modelling and rendering package*. Blender Foundation, Blender Institute, Amsterdam, 2014.
- [Bom 10] M. J. van der Bom, L. W. Bartels, M. J. Gounis, R. Homan, J. Timmer, M. A. Viergever, and J. P. W. Pluim. “Robust initialization of 2D-3D image registration using the projection-slice theorem and phase correlation”. *Medical Physics*, Vol. 37, No. 4, pp. 1884–1892, 2010.
- [Bose 90] C. Bose and I. Amir. “Design of Fiducials for Accurate Registration Using Machine Vision”. *Pattern Analysis and Machine Intelligence, IEEE Transactions on*, Vol. 12, No. 12, pp. 1196–1200, 1990.
- [Bost 15] Boston Scientific. *WATCHMAN implant*. 2015. <http://news.bostonscientific.com/image/LAA+and+Boston+Scientific+WATCHMAN.png>, last checked: 21 February 2016.
- [Bren 73] R. P. Brent. *Algorithms for minimization without derivatives*. Courier Dover Publications, 1973.
- [Bros 10] A. Brost, R. Liao, N. Strobel, and J. Hornegger. “Respiratory motion compensation by model-based catheter tracking during EP procedures”. *Medical Image Analysis*, Vol. 14, No. 5, pp. 695 – 706, 2010. Special Issue on the 12th International Conference on Medical Image Computing and Computer-Assisted Intervention (MICCAI) 2009.
- [Bros 12] A. Brost, A. Wimmer, R. Liao, F. Bourier, M. Koch, N. Strobel, K. Kurzdin, and J. Hornegger. “Constrained Registration for Motion Compensation in Atrial Fibrillation Ablation Procedures”. *Medical Imaging, IEEE Transactions on*, Vol. 31, No. 4, pp. 870–881, 2012.
- [Buzu 97] T. M. Buzug, J. Weese, C. Fassnacht, and C. Lorenz. “Image registration: Convex weighting functions for histogram-based similarity measures”. In: J. Troccaz, E. Grimson, and R. Mösges, Eds., *CVRMed-MRCAS’97*, pp. 203–212, Springer Berlin Heidelberg, 1997.
- [Caps] Capsis. *Main steps of the simplex algorithm*. <http://capsis.cirad.fr/capsis/documentation/optimisation>, last checked: 27 February 2016.
- [Chou 13] C.-R. Chou, B. Frederick, G. Mageras, S. Chang, and S. Pizer. “2D/3D image registration using regression learning”. *Computer Vision and Image Understanding*, Vol. 117, No. 9, pp. 1095 – 1106, 2013.
- [Cleg 15] S. D. Clegg, S. J. Chen, N. Nijhof, M. S. Kim, E. E. Salcedo, R. A. Quaife, J. C. Messenger, J. Bracken, and J. D. Carroll. “Integrated 3D Echo-X Ray to Optimize Image Guidance for Structural Heart Intervention”. *JACC: Cardiovascular Imaging*, Vol. 8, No. 3, pp. 371–374, 2015.
- [Cohn 97] L. H. Cohn, D. H. Adams, G. S. Couper, D. P. Bichell, D. M. Rosborough, S. P. Sears, and S. F. Aranki. “Minimally invasive cardiac valve surgery improves patient satisfaction while reducing costs of cardiac valve replacement and repair”. *Annals of surgery*, Vol. 226, No. 4, p. 421, 1997.
- [Cox 94] G. S. Cox and G. de Jager. “Automatic registration of temporal image pairs for digital subtraction angiography”. *Proceedings of SPIE Medical Imaging*, Vol. 2167, pp. 188–199, 1994.
- [Dani 95] W. G. Daniel and A. Mügge. “Transesophageal Echocardiography”. *New England Journal of Medicine*, Vol. 332, No. 19, pp. 1268–1280, 1995.

- [Dobb 03] J. T. Dobbins and D. J. Godfrey. “Digital x-ray tomosynthesis: current state of the art and clinical potential”. *Physics in Medicine and Biology*, Vol. 48, No. 19, p. R65, 2003.
- [Du 02] Z.-D. Du, Z. M. Hijazi, C. S. Kleinman, N. H. Silverman, and K. Larntz. “Comparison between transcatheter and surgical closure of secundum atrial septal defect in children and adults: results of a multicenter non-randomized trial”. *Journal of the American College of Cardiology*, Vol. 39, No. 11, pp. 1836–1844, 2002.
- [Faga 14] T. E. Fagan, U. T. Truong, P.-N. Jone, J. Bracken, R. Quaife, A. A. A. Hazeem, E. E. Salcedo, and B. M. Fonseca. “Multimodality 3-Dimensional Image Integration for Congenital Cardiac Catheterization”. *Methodist De-Bakey cardiovascular journal*, Vol. 10, No. 2, p. 68, 2014.
- [Feld 05] T. Feldman, H. S. Wasserman, H. C. Herrmann, W. Gray, P. C. Block, P. Whitlow, F. S. Goar, L. Rodriguez, F. Silvestry, A. Schwartz, *et al.* “Percutaneous Mitral Valve Repair Using the Edge-to-Edge Technique Six-Month Results of the EVEREST Phase I Clinical Trial”. *Journal of the American College of Cardiology*, Vol. 46, No. 11, pp. 2134–2140, 2005.
- [Feld 09] T. Feldman, S. Kar, M. Rinaldi, P. Fail, J. Hermiller, R. Smalling, P. L. Whitlow, W. Gray, R. Low, H. C. Herrmann, S. Lim, E. Foster, and D. Glower. “Percutaneous Mitral Repair With the MitraClip System—Safety and Midterm Durability in the Initial EVEREST (Endovascular Valve Edge-to-Edge REpair Study) Cohort”. *Journal of the American College of Cardiology*, Vol. 54, No. 8, pp. 686–694, 2009.
- [Flan 92] B. P. Flannery, W. H. Press, S. A. Teukolsky, and W. Vetterling. *Numerical recipes in C*. 1992.
- [Flec 15] E. Flécher, T. Langanay, and A. Leguerrier. “An overview of valvular heart disease in the elderly”. *Future Medicine*, 2015.
- [Flet 13] R. Fletcher. *Practical methods of optimization*. John Wiley & Sons, 2013.
- [Fran 98] A. F. Frangi, W. J. Niessen, K. L. Vincken, and M. A. Viergever. “Multiscale vessel enhancement filtering”. In: W. M. Wells, A. Colchester, and S. Delp, Eds., *Medical Image Computing and Computer-Assisted Intervention – MICCAI 1998*, pp. 130–137, Springer Berlin Heidelberg, 1998.
- [Fu 08] D. Fu and G. Kuduvali. “A fast, accurate, and automatic 2D-3D image registration for image-guided cranial radiosurgery”. *Medical Physics*, Vol. 35, No. 5, pp. 2180–2194, 2008.
- [Gafo 15] S. Gafoor, P. Schulz, L. Heuer, P. Matic, J. Franke, S. Bertog, M. Reinartz, L. Vaskelyte, I. Hofmann, and H. Sievert. “Use of EchoNavigator, a Novel Echocardiography-Fluoroscopy Overlay System, for Transseptal Puncture and Left Atrial Appendage Occlusion”. *Journal of Interventional Cardiology*, 2015.
- [Gall 11] J. Gall, A. Yao, N. Razavi, L. Van Gool, and V. Lempitsky. “Hough Forests for Object Detection, Tracking, and Action Recognition”. *Pattern Analysis and Machine Intelligence, IEEE Transactions on*, Vol. 33, No. 11, pp. 2188–2202, Nov 2011.

- [Gall 13] J. Gall and V. Lempitsky. *Decision forests for computer vision and medical image analysis*, Chap. Class-specific hough forests for object detection, pp. 143–157. Springer Science & Business Media, 2013.
- [Gao 10] G. Gao, G. Penney, N. Gogin, P. Cathier, A. Arujuna, M. Wright, D. Caulfield, A. Rinaldi, R. Razavi, and K. Rhode. “Rapid Image Registration of Three-Dimensional Transesophageal Echocardiography and X-ray Fluoroscopy for the Guidance of Cardiac Interventions”. In: N. Navab and P. Jannin, Eds., *Information Processing in Computer-Assisted Interventions*, pp. 124–134, Springer Berlin Heidelberg, 2010.
- [Gao 12] G. Gao, G. Penney, Y. Ma, N. Gogin, P. Cathier, A. Arujuna, G. Morton, D. Caulfield, J. Gill, C. Aldo Rinaldi, *et al.* “Registration of 3D trans-esophageal echocardiography to X-ray fluoroscopy using image-based probe tracking”. *Medical image analysis*, Vol. 16, No. 1, pp. 38–49, 2012.
- [Ghaf 15] S. Ghafurian, I. Hacihaliloglu, D. N. Metaxas, V. Tan, and K. Li. “3D/2D image registration using weighted histogram of gradient directions”. *Proceeding of SPIE Medical Imaging*, Vol. 9415, pp. 94151Z–94151Z–7, 2015.
- [Go 13] A. S. Go, D. Mozaffarian, V. L. Roger, E. J. Benjamin, J. D. Berry, W. B. Borden, D. M. Bravata, S. Dai, E. S. Ford, C. S. Fox, *et al.* “Heart disease and stroke statistics–2013 update: a report from the American Heart Association.”. *Circulation*, Vol. 127, No. 1, p. e6, 2013.
- [Gong 08] R. H. Gong and P. Abolmaesumi. “2D/3D registration with the CMA-ES method”. In: *Proceedings of SPIE Medical Imaging*, pp. 69181M–69181M–9, 2008.
- [Gott 96] L. Gottesfeld Brown and T. Boult. “Registration of planar film radiographs with computed tomography”. In: *Proceedings of the Workshop on Mathematical Methods in Biomedical Image Analysis*, pp. 42–51, Jun 1996.
- [Gouv 12] A. Gouveia, C. Metz, L. Freire, and S. Klein. “3D-2D image registration by nonlinear regression”. In: *9th IEEE International Symposium on Biomedical Imaging (ISBI)*, pp. 1343–1346, May 2012.
- [Habe 06] E. Haber and J. Modersitzki. “Intensity Gradient Based Registration and Fusion of Multi-modal Images”. In: R. Larsen, M. Nielsen, and J. Sporring, Eds., *Medical Image Computing and Computer-Assisted Intervention – MICCAI 2006*, pp. 726–733, Springer Berlin Heidelberg, 2006.
- [Hahn 15] R. Hahn. “Recent advances in echocardiography for valvular heart disease”. *F1000Research*, Vol. 4, 2015.
- [Hans 06] N. Hansen. “The CMA Evolution Strategy: A Comparing Review”. In: J. A. Lozano, P. Larrañaga, I. n. Inza, and E. Bengoetxea, Eds., *Towards a New Evolutionary Computation*, pp. 75–102, Springer Berlin Heidelberg, 2006.
- [Harr 07] M. Harris. “Optimizing parallel reduction in CUDA”. *NVIDIA Developer Technology*, Vol. 2, 2007.
- [Hatt 13] C. R. Hatt, A. K. Jain, V. Parthasarathy, A. Lang, and A. N. Raval. “MRI–3D ultrasound–X-ray image fusion with electromagnetic tracking

- for transcatheter therapeutic injections: In-vitro validation and in-vivo feasibility”. *Computerized Medical Imaging and Graphics*, Vol. 37, No. 2, pp. 162–173, 2013.
- [Hatt 14] C. R. Hatt, M. A. Speidel, and A. N. Raval. “Efficient feature-based 2D/3D registration of transesophageal echocardiography to x-ray fluoroscopy for cardiac interventions”. In: *Proceedings of SPIE Medical Imaging*, pp. 90361J–90361J–10, 2014.
- [Hatt 15a] C. R. Hatt, M. A. Speidel, and A. N. Raval. “Hough Forests for Real-Time, Automatic Device Localization in Fluoroscopic Images: Application to TAVR”. In: N. Navab, J. Hornegger, W. M. Wells, and A. F. Frangi, Eds., *Medical Image Computing and Computer-Assisted Intervention – MICCAI 2015*, pp. 307–314, Springer International Publishing, 2015.
- [Hatt 15b] C. R. Hatt, M. A. Speidel, and A. N. Raval. “Robust 5DOF Transesophageal Echo Probe Tracking at Fluoroscopic Frame Rates”. In: N. Navab, J. Hornegger, W. M. Wells, and A. F. Frangi, Eds., *Medical Image Computing and Computer-Assisted Intervention – MICCAI 2015*, pp. 290–297, Springer International Publishing, 2015.
- [Hatt 15c] C. R. Hatt, M. T. Tomkowiak, D. A. P. Dunkerley, J. M. Slagowski, T. Funk, A. N. Raval, and M. A. Speidel. “Depth-resolved registration of transesophageal echo to x-ray fluoroscopy using an inverse geometry fluoroscopy system”. *Medical Physics*, Vol. 42, No. 12, pp. 7022–7033, 2015.
- [Heim 13] T. Heimann, P. Mountney, M. John, and R. Ionasec. “Learning without Labeling: Domain Adaptation for Ultrasound Transducer Localization”. In: *Medical Image Computing and Computer-Assisted Intervention – MICCAI 2013*, pp. 49–56, Springer, 2013.
- [Heim 14] T. Heimann, P. Mountney, M. John, and R. Ionasec. “Real-time ultrasound transducer localization in fluoroscopy images by transfer learning from synthetic training data”. *Medical image analysis*, Vol. 18, No. 8, pp. 1320–1328, 2014.
- [Hein 06] R. Hein, N. Wunderlich, G. Robertson, N. Wilson, and H. Sievert. “Catheter closure of paravalvular leak”. *EuroIntervention : Journal of EuroPCR in collaboration with the Working Group on Interventional Cardiology of the European Society of Cardiology*, Vol. 2, No. 3, pp. 318–325, November 2006.
- [Hipw 03] J. H. Hipwell, G. P. Penney, R. A. McLaughlin, K. Rhode, P. Summers, T. C. Cox, J. V. Byrne, J. A. Noble, and D. J. Hawkes. “Intensity-based 2-D-3-D registration of cerebral angiograms”. *Medical Imaging, IEEE Transactions on*, Vol. 22, No. 11, pp. 1417–1426, 2003.
- [Hofm 11] H. Hofmann, B. Keck, C. Rohkohl, and J. Hornegger. “Comparing performance of many-core CPUs and GPUs for static and motion compensated reconstruction of C-arm CT data”. *Medical Physics*, Vol. 38, No. 1, pp. 468–473, 2011.
- [Holm 09] D. R. Holmes, V. Y. Reddy, Z. G. Turi, S. K. Doshi, H. Sievert, M. Buchbinder, C. M. Mullin, P. Sick, P. A. Investigators, *et al.* “Percutaneous closure of the left atrial appendage versus warfarin therapy for prevention of stroke in patients with atrial fibrillation: a randomised non-inferiority trial”. *The Lancet*, Vol. 374, No. 9689, pp. 534–542, 2009.

- [Hour 92] M. Hourihan, S. B. Perry, V. S. Mandell, J. F. Keane, J. J. Rome, J. A. Bittl, and J. E. Lock. “Transcatheter umbrella closure of valvular and paravalvular leaks”. *Journal of the American College of Cardiology*, Vol. 20, No. 6, pp. 1371–1377, 1992.
- [Hous 12] R. Housden, A. Arujuna, Y. Ma, N. Nijhof, G. Gijbbers, R. Bullens, M. O’Neill, M. Cooklin, C. Rinaldi, J. Gill, S. Kapetanakis, J. Hancock, M. Thomas, R. Razavi, and K. Rhode. “Evaluation of a Real-Time Hybrid Three-Dimensional Echo and X-Ray Imaging System for Guidance of Cardiac Catheterisation Procedures”. In: N. Ayache, H. Delingette, P. Golland, and K. Mori, Eds., *Medical Image Computing and Computer-Assisted Intervention – MICCAI 2012*, pp. 25–32, Springer Berlin Heidelberg, 2012.
- [Hous 13] R. J. Housden, Y. Ma, A. Arujuna, N. Nijhof, P. Cathier, G. Gijbbers, R. Bullens, J. Gill, C. A. Rinaldi, V. Parish, and K. S. Rhode. “Extended-Field-of-View Three-Dimensional Transesophageal Echocardiography Using Image-Based X-Ray Probe Tracking”. *Ultrasound in Medicine & Biology*, Vol. 39, No. 6, pp. 993 – 1005, 2013.
- [Iona 09] R. Ionasec, I. Voigt, B. Georgescu, Y. Wang, H. Houle, J. Hornegger, N. Navab, and D. Comaniciu. “Personalized Modeling and Assessment of the Aortic-Mitral Coupling from 4D TEE and CT”. In: G.-Z. Yang, D. Hawkes, D. Rueckert, A. Noble, and C. Taylor, Eds., *Medical Image Computing and Computer-Assisted Intervention – MICCAI 2009*, pp. 767–775, Springer Berlin Heidelberg, 2009.
- [Iona 10] R. Ionasec, I. Voigt, B. Georgescu, Y. Wang, H. Houle, F. Vega-Higuera, N. Navab, and D. Comaniciu. “Patient-Specific Modeling and Quantification of the Aortic and Mitral Valves From 4-D Cardiac CT and TEE”. *Medical Imaging, IEEE Transactions on*, Vol. 29, No. 9, pp. 1636–1651, Sept 2010.
- [Jain 09] A. Jain, L. Gutierrez, and D. Stanton. “3D TEE Registration with X-Ray Fluoroscopy for Interventional Cardiac Applications”. In: N. Ayache, H. Delingette, and M. Sermesant, Eds., *Functional Imaging and Modeling of the Heart*, pp. 321–329, Springer Berlin Heidelberg, 2009.
- [John 10a] M. John, R. Liao, Y. Zheng, A. Nöttling, J. Boese, U. Kirschstein, J. Kempfert, and T. Walther. “System to Guide Transcatheter Aortic Valve Implantations Based on Interventional C-Arm CT Imaging”. In: T. Jiang, N. Navab, J. P. Pluim, and M. A. Viergever, Eds., *Medical Image Computing and Computer-Assisted Intervention – MICCAI 2010*, pp. 375–382, Springer Berlin Heidelberg, 2010.
- [John 10b] S. G. Johnson. “The NLOpt nonlinear-optimization package”. Tech. Rep., Massachusetts Institute of Technology, 2010.
- [Jomi 06] J. Jomier, E. Bullitt, M. Horn, C. Pathak, and S. Aylward. “3D/2D Model-to-Image Registration Applied to TIPS Surgery”. In: R. Larsen, M. Nielsen, and J. Sporring, Eds., *Medical Image Computing and Computer-Assisted Intervention – MICCAI 2006*, pp. 662–669, Springer Berlin Heidelberg, 2006.
- [Kais 11] M. Kaiser. *Basic Algorithms for Fusion of X-ray & Ultrasound Images*. Master’s thesis, Friedrich-Schiller-University Jena, 2011.

- [Kais 13a] M. Kaiser, M. John, A. Borsdorf, P. Mountney, R. Ionasec, A. Nötting, P. Kiefer, J. Seeburger, and T. Neumuth. “Significant acceleration of 2D-3D registration-based fusion of Ultrasound and X-ray images by mesh-based DRR rendering”. In: *Proceedings of SPIE Medical Imaging*, pp. 867111–867111–6, Orlando, Florida, USA, February 2013.
- [Kais 13b] M. Kaiser, M. John, A. Borsdorf, A. Nötting, and T. Neumuth. “A Hybrid Optimization Approach for 2D-3D Registrationbased Fusion of Ultrasound and X-Ray”. In: *Biomedical Engineering/Biomedizinische Technik*, De Gruyter, Graz, Austria, September 2013.
- [Kais 13c] M. Kaiser, M. John, T. Neumuth, and G. Rose. “Mesh-based DRR Rendering accelerates 2D/3D Registration for the Fusion of Ultrasound and X-ray Images”. In: J. Thiery, A. G. Beck-Sickinger, and T. Arendt, Eds., *12th Research Festival Leipzig*, p. 122, Leipzig, Germany, December 2013.
- [Kais 14a] M. Kaiser, M. John, T. Heimann, A. Brost, T. Neumuth, and G. Rose. “2D/3D Registration of TEE Probe from Two Non-orthogonal C-arm Directions”. In: P. Golland, C. Barillot, J. Hornegger, and R. Howe, Eds., *Medical Image Computing and Computer-Assisted Intervention – MICCAI 2014*, pp. 283–290, Boston, MA, USA, September 2014.
- [Kais 14b] M. Kaiser, M. John, T. Heimann, T. Neumuth, and G. Rose. “Comparison of Optimizers for 2D/3D Registration for Fusion of Ultrasound and X-Ray”. In: T. M. Deserno, H. Handels, H.-P. Meinzer, and T. Tolxdorff, Eds., *Bildverarbeitung für die Medizin 2014*, pp. 312–317, Springer Berlin Heidelberg, Aachen, Germany, March 2014.
- [Kais 14c] M. Kaiser, M. John, T. Heimann, T. Neumuth, and G. Rose. “Improvement of Manual 2D/3D Registration by Decoupling the Visual Influence of the Six Degrees of Freedom”. In: *IEEE 11th International Symposium on Biomedical Imaging (ISBI)*, pp. 766–769, 2014.
- [Kais 14d] M. Kaiser, M. John, M. Körner, T. Heimann, T. Neumuth, and G. Rose. “Necessity of Calibrated Projection Matrices for the 2D/3D Registration of TEE ultrasound and X-ray”. In: *Image-Guided Interventions – IGIC*, Magdeburg, Germany, April 2014.
- [Kell 10] B. B. Kelly, V. Fuster, *et al.* *Promoting Cardiovascular Health in the Developing World: A Critical Challenge to Achieve Global Health*. National Academies Press, 2010.
- [Kemp 11] J. Kempfert, A. Noetting, M. John, A. Rastan, F. W. Mohr, and T. Walther. “Automatically Segmented DynaCTEnhanced Imaging During Transcatheter Aortic Valve Implantation”. *Journal of the American College of Cardiology*, Vol. 58, No. 25, p. e211, 2011.
- [Kim 14] M. S. Kim, J. Bracken, N. Nijhof, E. E. Salcedo, R. A. Quaipe, J. C. Messenger, and J. D. Carroll. “Integrated 3D Echo-X-Ray Navigation to Predict Optimal Angiographic Deployment Projections for TAVR”. *JACC: Cardiovascular Imaging*, Vol. 7, No. 8, pp. 847–848, 2014.
- [Kraa 05] E. van de Kraats, G. Penney, D. Tomazevic, T. van Walsum, and W. Niessen. “Standardized evaluation methodology for 2-D-3-D registration”. *Medical Imaging, IEEE Transactions on*, Vol. 24, No. 9, pp. 1177–1189, 2005.

- [Kron 15] I. Kronzon, V. Jelnin, C. E. Ruiz, M. Saric, M. R. Williams, A. M. Kasel, A. Shivaraju, A. Colombo, and A. Kastrati. “Optimal Imaging for Guiding TAVR: Transesophageal or Transthoracic Echocardiography, or Just Fluoroscopy?”. *JACC: Cardiovascular Imaging*, Vol. 8, No. 3, pp. 361–370, 2015.
- [Krug 03] J. Kruger and R. Westermann. “Acceleration Techniques for GPU-based Volume Rendering”. In: *Proceedings of the 14th IEEE Visualization 2003 (VIS’03)*, p. 38, IEEE Computer Society, Washington, DC, USA, 2003.
- [Lang 10] P. Lang, P. Seslija, D. Habets, M. Chu, D. Holdsworth, and T. Peters. “Three-Dimensional Ultrasound Probe Pose Estimation from Single-Perspective X-Rays for Image-Guided Interventions”. In: H. Liao, P. Edwards, X. Pan, Y. Fan, and G.-Z. Yang, Eds., *Medical Imaging and Augmented Reality*, pp. 344–352, Springer Berlin Heidelberg, 2010.
- [Lang 11] P. Lang, P. Seslija, D. Bainbridge, G. M. Guiraudon, D. L. Jones, M. W. Chu, D. W. Holdsworth, and T. M. Peters. “Accuracy assessment of fluoroscopy-transesophageal echocardiography registration”. In: *Proceedings of SPIE Medical Imaging*, pp. 79641Y–79641Y–10, 2011.
- [Lang 12] P. Lang, P. Seslija, M. Chu, D. Bainbridge, G. Guiraudon, D. Jones, and T. Peters. “US-Fluoroscopy Registration for Transcatheter Aortic Valve Implantation”. *Biomedical Engineering, IEEE Transactions on*, Vol. 59, No. 5, pp. 1444–1453, 2012.
- [Lemi 94] L. Lemieux, R. Jagoe, D. R. Fish, N. D. Kitchen, and D. G. T. Thomas. “A patient-to-computed-tomography image registration method based on digitally reconstructed radiographs”. *Medical Physics*, Vol. 21, No. 11, pp. 1749–1760, 1994.
- [Leon 10] M. B. Leon, C. R. Smith, M. Mack, D. C. Miller, J. W. Moses, L. G. Svensson, E. M. Tuzcu, J. G. Webb, G. P. Fontana, R. R. Makkar, D. L. Brown, P. C. Block, R. A. Guyton, A. D. Pichard, J. E. Bavaria, H. C. Herrmann, P. S. Douglas, J. L. Petersen, J. J. Akin, W. N. Anderson, D. Wang, and S. Pocock. “Transcatheter Aortic-Valve Implantation for Aortic Stenosis in Patients Who Cannot Undergo Surgery”. *New England Journal of Medicine*, Vol. 363, No. 17, pp. 1597–1607, 2010.
- [Liao 13] R. Liao, L. Zhang, Y. Sun, S. Miao, and C. Chef d’Hotel. “A Review of Recent Advances in Registration Techniques Applied to Minimally Invasive Therapy”. *Multimedia, IEEE Transactions on*, Vol. 15, No. 5, pp. 983–1000, 2013.
- [Lint 10] C. A. Linte, M. Carias, D. S. Cho, D. F. Pace, J. Moore, C. Wedlake, D. Bainbridge, B. Kiaii, and T. M. Peters. “Estimating heart shift and morphological changes during minimally invasive cardiac interventions”. In: *Proceedings of SPIE Medical Imaging*, pp. 762509–762509–11, 2010.
- [Livy 03] H. Livyatan, Z. Yaniv, and L. Joskowicz. “Gradient-based 2-D/3-D rigid registration of fluoroscopic X-ray to CT”. *Medical Imaging, IEEE Transactions on*, Vol. 22, No. 11, pp. 1395–1406, 2003.
- [Lync 06] P. J. Lynch. *Transesophageal echocardiography ultrasound diagram*. 2006. https://en.wikipedia.org/wiki/File:Transesophageal_echocardiography_diagram.svg, last checked: 21 February 2016.

- [Ma 10] Y. Ma, G. P. Penney, D. Bos, P. Frissen, C. A. Rinaldi, R. Razavi, and K. S. Rhode. “Hybrid echo and x-ray image guidance for cardiac catheterization procedures by using a robotic arm: a feasibility study”. *Physics in Medicine and Biology*, Vol. 55, No. 13, p. N371, 2010.
- [Maes 97] F. Maes, A. Collignon, D. Vandermeulen, G. Marchal, and P. Suetens. “Multimodality image registration by maximization of mutual information”. *Medical Imaging, IEEE Transactions on*, Vol. 16, No. 2, pp. 187–198, April 1997.
- [Main 98] J. Maintz and M. A. Viergever. “A survey of medical image registration”. *Medical Image Analysis*, Vol. 2, No. 1, pp. 1 – 36, 1998.
- [Mais 13] F. Maisano, O. Franzen, S. Baldus, U. SchÄ€fer, J. Hausleiter, C. Butter, G. P. Ussia, H. Sievert, G. Richardt, J. D. Widder, T. Moccetti, and W. Schillinger. “Percutaneous Mitral Valve Interventions in the Real World: Early and 1-Year Results From the ACCESS-EU, A Prospective, Multicenter, Nonrandomized Post-Approval Study of the MitraClip Therapy in Europe”. *Journal of the American College of Cardiology*, Vol. 62, No. 12, pp. 1052–1061, 2013.
- [Maki 12] A. Maki and R. Gherardi. “Conditional Variance of Differences: A Robust Similarity Measure for Matching and Registration”. In: G. Gimelfarb, E. Hancock, A. Imiya, A. Kuijper, M. Kudo, S. Omachi, T. Windeatt, and K. Yamada, Eds., *Structural, Syntactic, and Statistical Pattern Recognition*, pp. 657–665, Springer Berlin Heidelberg, 2012.
- [Marg 11] A. Margolis. “A Literature Review of Domain Adaptation with Unlabeled Data”. Tech. Rep., University of Washington, 2011.
- [Mark 12] P. Markelj, D. Tomaževič, B. Likar, and F. Pernuš. “A review of 3D/2D registration methods for image-guided interventions”. *Medical Image Analysis*, Vol. 16, No. 3, pp. 642 – 661, 2012. Computer Assisted Interventions.
- [McCl 13] R. S. McClure, L. V. Athanasopoulos, S. McGurk, M. J. Davidson, G. S. Couper, and L. H. Cohn. “One thousand minimally invasive mitral valve operations: Early outcomes, late outcomes, and echocardiographic follow-up”. *The Journal of Thoracic and Cardiovascular Surgery*, Vol. 145, No. 5, pp. 1199 – 1206, 2013.
- [Miao 13a] S. Miao, T. Huynh, C. Adnet, M. Pfister, and R. Liao. “Intensity-Based 3D-2D Mesh-to-Image Registration Using Mesh-Based Digitally Reconstructed Radiography”. In: H. Liao, C. Linte, K. Masamune, T. Peters, and G. Zheng, Eds., *Augmented Reality Environments for Medical Imaging and Computer-Assisted Interventions*, pp. 86–96, Springer Berlin Heidelberg, 2013.
- [Miao 13b] S. Miao, R. Liao, and M. Pfister. “Toward smart utilization of two X-ray images for 2-D/3-D registration applied to abdominal aortic aneurysm interventions”. *Computers & Electrical Engineering*, Vol. 39, No. 5, pp. 1485 – 1498, 2013.
- [Miao 16] S. Miao, Z. Wang, and R. Liao. “A CNN Regression Approach for Real-time 2D/3D Registration”. *Medical Imaging, IEEE Transactions on*, Vol. PP, No. 99, pp. 1–1, 2016.
- [Mode 03] J. Modersitzki. *Numerical methods for image registration. Numerical Mathematics and Scientific Computation*, Oxford University Press, Oxford, 2003.

- [Moor 10] J. T. Moore, A. D. Wiles, C. Wedlake, D. Bainbridge, B. Kiaii, A. L. Trejos, R. Patel, and T. M. Peters. “Integration of trans-esophageal echocardiography with magnetic tracking technology for cardiac interventions”. In: *Proceedings of SPIE Medical Imaging*, pp. 76252Y–76252Y–10, 2010.
- [Moor 13] J. Moore, M. Chu, B. Kiaii, D. Bainbridge, G. Guiraudon, C. Wedlake, M. Currie, M. Rajchl, R. Patel, and T. Peters. “A Navigation Platform for Guidance of Beating Heart Transapical Mitral Valve Repair”. *Biomedical Engineering, IEEE Transactions on*, Vol. 60, No. 4, pp. 1034–1040, April 2013.
- [Moun 12] P. Mountney, R. Ionasec, M. Kaiser, S. Mamaghani, W. Wu, T. Chen, M. John, J. Boese, and D. Comaniciu. “Ultrasound and Fluoroscopic Images Fusion by Autonomous Ultrasound Probe Detection”. In: N. Ayache, H. Delingette, P. Golland, and K. Mori, Eds., *Medical Image Computing and Computer-Assisted Intervention – MICCAI 2012*, pp. 544–551, Springer Berlin Heidelberg, Nice, France, September 2012.
- [Navi 12] J. Navia and J. Chen. “Method for implanting a cardiovascular valve”. *US Patent 8,105,375*, 2012.
- [Neld 65] J. A. Nelder and R. Mead. “A simplex method for function minimization”. *The computer journal*, Vol. 7, No. 4, pp. 308–313, 1965.
- [Nish 14] R. A. Nishimura, C. M. Otto, R. O. Bonow, B. A. Carabello, J. P. Erwin, III, R. A. Guyton, P. T. O’Gara, C. E. Ruiz, N. J. Skubas, P. Sorajja, T. M. Sundt, III, and J. D. Thomas. “2014 AHA/ACC Guideline for the Management of Patients With Valvular Heart Disease A Report of the American College of Cardiology/American Heart Association Task Force on Practice Guidelines”. *Journal of the American College of Cardiology*, Vol. 63, No. 22, pp. e57–e185, 2014.
- [Nkom 06] V. T. Nkomo, J. M. Gardin, T. N. Skelton, J. S. Gottdiener, C. G. Scott, and M. Enriquez-Sarano. “Burden of valvular heart diseases: a population-based study”. *The Lancet*, Vol. 368, No. 9540, pp. 1005 – 1011, 2006.
- [Noac 13] T. Noack, P. Kiefer, R. Ionasec, I. Voigt, T. Mansi, M. Vollroth, M. Hobbartner, M. Misfeld, F.-W. Mohr, and J. Seeburger. “New concepts for mitral valve imaging”. *Annals of cardiothoracic surgery*, Vol. 2, No. 6, p. 787, 2013.
- [Oppe 75] A. V. Oppenheim and R. Schaffer. *Digital Signal Processing*. Prentice-Hall, 1975.
- [Otak 12] Y. Otake, M. Armand, R. S. Armiger, M. Kutzer, E. Basafa, P. Kazanzides, and R. Taylor. “Intraoperative Image-based Multiview 2D/3D Registration for Image-Guided Orthopaedic Surgery: Incorporation of Fiducial-Based C-Arm Tracking and GPU-Acceleration”. *Medical Imaging, IEEE Transactions on*, Vol. 31, No. 4, pp. 948–962, 2012.
- [Otto 04] C. M. Otto and A. S. Pearlman. *Textbook of clinical echocardiography*. Saunders Philadelphia, PA, 2004.
- [Park 11] J.-W. Park, A. Bethencourt, H. Sievert, G. Santoro, B. Meier, K. Walsh, J. R. Lopez-Minquez, D. Meerkin, M. Valdés, O. Ormerod, and B. Leithäuser. “Left atrial appendage closure with amplatzer cardiac plug in atrial fibrillation: Initial european experience”. *Catheterization and Cardiovascular Interventions*, Vol. 77, No. 5, pp. 700–706, 2011.

- [Penn 00] G. P. Penney. *Registration of tomographic images to X-ray projections for use in image guided interventions*. PhD thesis, University of London, 2000.
- [Penn 98] G. Penney, J. Weese, J. Little, P. Desmedt, D. L. G. Hill, and D. Hawkes. “A comparison of similarity measures for use in 2-D-3-D medical image registration”. *Medical Imaging, IEEE Transactions on*, Vol. 17, No. 4, pp. 586–595, 1998.
- [Phil 14] Philips Healthcare. *EchoNavigator*. 2014.
- [Pick 09] M. Pickering, A. Muhit, J. Scarvell, and P. Smith. “A new multi-modal similarity measure for fast gradient-based 2D-3D image registration”. In: *Engineering in Medicine and Biology Society (EMBC), Annual International Conference of the IEEE*, pp. 5821–5824, 2009.
- [Plui 00] J. Pluim, J. Maintz, and M. Viergever. “Image Registration by Maximization of Combined Mutual Information and Gradient Information”. In: S. Delp, A. DiGoia, and B. Jaramaz, Eds., *Medical Image Computing and Computer-Assisted Intervention – MICCAI 2000*, pp. 452–461, Springer Berlin Heidelberg, 2000.
- [Pras 15] M. Prasad, A. Cassar, K. A. Fetterly, M. Bell, H. Theessen, O. Ecabert, J. F. Bresnahan, and A. Lerman. “Co-registration of angiography and intravascular ultrasound images through image-based device tracking”. *Catheterization and Cardiovascular Interventions*, 2015.
- [Pres 15] G. Preston-Maher, R. Torii, and G. Burriesci. “A Technical Review of Minimally Invasive Mitral Valve Replacements”. *Cardiovascular Engineering and Technology*, Vol. 6, No. 2, pp. 174–184, 2015.
- [Raja 08] P. V. Raja, J. Huang, A. V. Germanwala, P. Gailloud, K. P. Murphy, and R. J. Tamargo. “Microsurgical clipping and endovascular coiling of intracranial aneurysms: a critical review of the literature”. *Neurosurgery*, Vol. 62, No. 6, pp. 1187–1203, 2008.
- [Ralo 14] K. Ralovich, M. John, E. Camus, N. Navab, and T. Heimann. “6DoF Catheter Detection, Application to Intracardiac Echocardiography”. In: P. Golland, N. Hata, C. Barillot, J. Hornegger, and R. Howe, Eds., *Medical Image Computing and Computer-Assisted Intervention – MICCAI 2014*, pp. 635–642, Springer International Publishing, 2014.
- [Rowa 90] T. H. Rowan. *Functional Stability Analysis of Numerical Algorithms*. PhD thesis, University of Texas at Austin, Austin, TX, USA, 1990. UMI Order No. GAX90-31702.
- [Sebe 00] N. Sebe, M. S. Lew, and D. P. Huijismans. “Toward improved ranking metrics”. *Pattern Analysis and Machine Intelligence, IEEE Transactions on*, Vol. 22, No. 10, pp. 1132–1143, 2000.
- [Seck 99] M.-A. Secknus, C. R. Asher, G. M. Scalia, D. M. C. III, and W. J. Stewart. “Intraoperative Transesophageal Echocardiography in Minimally Invasive Cardiac Valve Surgery”. *Journal of the American Society of Echocardiography*, Vol. 12, No. 4, pp. 231 – 236, 1999.
- [Seeb 10] J. Seeburger, M. A. Borger, H. Tschernich, S. Leontjev, D. Holzhey, T. Noack, J. Ender, and F. W. Mohr. “Transapical beating heart mitral valve repair”. *Circulation: Cardiovascular Interventions*, Vol. 3, No. 6, pp. 611–612, 2010.

- [Shap08] L. Shapira, A. Shamir, and D. Cohen-Or. “Consistent mesh partitioning and skeletonisation using the shape diameter function”. *The Visual Computer*, Vol. 24, No. 4, pp. 249–259, 2008.
- [Smit11] C. R. Smith, M. B. Leon, M. J. Mack, D. C. Miller, J. W. Moses, L. G. Svensson, E. M. Tuzcu, J. G. Webb, G. P. Fontana, R. R. Makkar, M. Williams, T. Dewey, S. Kapadia, V. Babaliaros, V. H. Thourani, P. Corso, A. D. Pichard, J. E. Bavaria, H. C. Herrmann, J. J. Akin, W. N. Anderson, D. Wang, and S. J. Pocock. “Transcatheter versus Surgical Aortic-Valve Replacement in High-Risk Patients”. *New England Journal of Medicine*, Vol. 364, No. 23, pp. 2187–2198, 2011.
- [Smol10] G. Smolka and W. Wojakowski. “Paravalvular leak – important complication after implantation of prosthetic valve”. *E-journal of Cardiology Practice*, Vol. 9, 2010.
- [Sobe68] I. Sobel and G. Feldman. “A 3x3 isotropic gradient operator for image processing”. 1968.
- [Sond15] L. Søndergaard, O. De Backer, O. W. Franzen, S. J. Holme, N. Ihlemann, N. G. Vejlstrup, P. B. Hansen, and A. Quadri. “First-in-Human Case of Transfemoral CardiAQ Mitral Valve Implantation”. *Circulation: Cardiovascular Interventions*, Vol. 8, No. 7, p. e002135, 2015.
- [Spei14] M. Speidel, C. Hatt, M. Tomkowiak, T. Funk, and A. Raval. “TU-F-BRF-04: Registration of 3D Transesophageal Echocardiography and X-Ray Fluoroscopy Using An Inverse Geometry X-Ray System”. *Medical Physics*, Vol. 41, No. 6, pp. 471–471, 2014.
- [Stei10] D. H. Steinberg, S. Staubach, J. Franke, and H. Sievert. “Defining structural heart disease in the adult patient: current scope, inherent challenges and future directions”. *European Heart Journal Supplements*, Vol. 12, No. suppl E, pp. E2–E9, 2010.
- [Thev95] P. Thevenaz, U. E. Ruttimann, and M. Unser. “Iterative multi-scale registration without landmarks”. In: *Image Processing, 1995. Proceedings., International Conference on*, pp. 228–231 vol.3, Oct 1995.
- [Turg05] G.-A. Turgeon, G. Lehmann, G. Guiraudon, M. Drangova, D. Holdsworth, and T. Peters. “2D-3D registration of coronary angiograms for cardiac procedure planning and guidance”. *Medical Physics*, Vol. 32, No. 12, pp. 3737–3749, 2005.
- [Uner14] A. Uneri, Y. Otake, A. S. Wang, G. Kleinszig, S. Vogt, A. J. Khanna, and J. H. Siewerdsen. “3D-2D registration for surgical guidance: effect of projection view angles on registration accuracy”. *Physics in Medicine and Biology*, Vol. 59, No. 2, p. 271, 2014.
- [Varn13a] A. Varnavas, T. Carrell, and G. Penney. “Fully automated initialisation of 2D/3D image registration”. In: *Biomedical Imaging (ISBI), 2013 IEEE 10th International Symposium on*, pp. 568–571, 2013.
- [Varn13b] A. Varnavas, T. Carrell, and G. Penney. “Increasing the Automation of a 2D-3D Registration System”. *Medical Imaging, IEEE Transactions on*, Vol. 32, No. 2, pp. 387–399, 2013.
- [Varn15] A. Varnavas, T. Carrell, and G. Penney. “Fully Automated 2D–3D Registration and Verification”. *Medical Image Analysis*, 2015.

- [Viol 97] P. Viola and W. Wells III. “Alignment by Maximization of Mutual Information”. *International Journal of Computer Vision*, Vol. 24, No. 2, pp. 137–154, 1997.
- [Visu] Visual Computing Lab - ISTI - CNR. *MeshLab*.
- [Voigt 15] I. Voigt, M. Scutaru, T. Mansi, B. Georgescu, N. El-Zehiry, H. Houle, and D. Comaniciu. “Robust Live Tracking of Mitral Valve Annulus for Minimally-Invasive Intervention Guidance”. In: N. Navab, J. Hornegger, W. M. Wells, and A. F. Frangi, Eds., *Medical Image Computing and Computer-Assisted Intervention – MICCAI 2015*, pp. 439–446, Springer International Publishing, 2015.
- [VXL] VXL Contributors. *VXL C++ Libraries for Computer Vision Research and Implementation*.
- [Wack 09] M. Wacker and F. Deinzer. “Automatic Robust Medical Image Registration Using a New Democratic Vector Optimization Approach with Multiple Measures”. In: G.-Z. Yang, D. Hawkes, D. Rueckert, A. Noble, and C. Taylor, Eds., *Medical Image Computing and Computer-Assisted Intervention – MICCAI 2009*, pp. 590–597, Springer Berlin Heidelberg, 2009.
- [Walt 07] T. Walther, P. Simon, T. Dewey, G. Wimmer-Greinecker, V. Falk, M. T. Kasimir, M. Doss, M. A. Borger, G. Schuler, D. Glogar, *et al.* “Transapical minimally invasive aortic valve implantation multicenter experience”. *Circulation*, Vol. 116, No. 11 suppl, pp. I-240, 2007.
- [Wang 11] P. Wang, T. Chen, O. Ecabert, S. Prummer, M. Ostermeier, and D. Comaniciu. “Image-Based Device Tracking for the Co-registration of Angiography and Intravascular Ultrasound Images”. In: G. Fichtinger, A. Martel, and T. Peters, Eds., *Medical Image Computing and Computer-Assisted Intervention – MICCAI 2011*, pp. 161–168, Springer Berlin Heidelberg, 2011.
- [Wees 99] J. Weese, R. Goecke, G. P. Penney, P. Desmedt, T. M. Buzug, and H. Schumann. “Fast voxel-based 2D/3D registration algorithm using a volume rendering method based on the shear-warp factorization”. *Proceedings of SPIE Medical Imaging*, Vol. 3661, pp. 802–810, 1999.
- [Wein 08] A. Weinlich, B. Keck, H. Scherl, M. Kowarschik, and J. Hornegger. “Comparison of high-speed ray casting on GPU using CUDA and OpenGL”. In: *Proceedings of the First International Workshop on New Frontiers in High-performance and Hardware-aware Computing*, pp. 25–30, 2008.
- [Wu 11] W. Wu, T. Chen, A. Barbu, P. Wang, N. Strobel, S. Zhou, and D. Comaniciu. “Learning-based hypothesis fusion for robust catheter tracking in 2D X-ray fluoroscopy”. In: *Computer Vision and Pattern Recognition (CVPR), 2011 IEEE Conference on*, pp. 1097–1104, June 2011.
- [Wu 13] X. Wu, J. Housden, Y. Ma, D. Rueckert, and K. S. Rhode. “Real-Time Catheter Extraction from 2D X-Ray Fluoroscopic and 3D Echocardiographic Images for Cardiac Interventions”. In: O. Camara, T. Mansi, M. Pop, K. Rhode, M. Sermesant, and A. Young, Eds., *Statistical Atlases and Computational Models of the Heart. Imaging and Modelling Challenges*, pp. 198–206, Springer Berlin Heidelberg, 2013.

- [Wu 14] X. Wu, J. Housden, Y. Ma, K. Rhode, and D. Rueckert. “A fast catheter segmentation and tracking from echocardiographic sequences based on corresponding X-ray fluoroscopic image segmentation and hierarchical GRAPH modelling”. In: *Biomedical Imaging (ISBI), 2014 IEEE 11th International Symposium on*, pp. 951–954, April 2014.
- [Yadd 06] Yaddah. *Diagram of the human heart*. 2006. https://commons.wikimedia.org/wiki/File:Diagram_of_the_human_heart.svg, last checked: 21 February 2016.
- [Zahn 11] R. Zahn, U. Gerckens, E. Grube, A. Linke, H. Sievert, H. Eggebrecht, R. Hambrecht, S. Sack, K. E. Hauptmann, G. Richardt, H.-R. Figulla, and J. Senges. “Transcatheter aortic valve implantation: first results from a multi-centre real-world registry”. *European Heart Journal*, Vol. 32, No. 2, pp. 198–204, 2011.
- [Zhen 10] Y. Zheng, M. John, R. Liao, J. Boese, U. Kirschstein, B. Georgescu, S. Zhou, J. Kempfert, T. Walther, G. Brockmann, and D. Comaniciu. “Automatic Aorta Segmentation and Valve Landmark Detection in C-Arm CT: Application to Aortic Valve Implantation”. In: T. Jiang, N. Navab, J. Pluim, and M. Viergever, Eds., *Medical Image Computing and Computer-Assisted Intervention – MICCAI 2010*, pp. 476–483, Springer Berlin Heidelberg, 2010.



- MAFO-01** ORTHS, A.: *Multikriterielle, optimale Planung von Verteilungsnetzen im liberalisierten Energiemarkt unter Verwendung von spieltheoretischen Verfahren*, 2003. ISBN 3-929757-57-5.
- MAFO-02** PURMANN, M.: *Optimierung des Betriebsverhaltens von PEM-Brennstoffzellen unter Berücksichtigung von elektrischem und Gesamtwirkungsgrad bei unterschiedlichen Lastanforderungen und Betriebsparametern*, 2004. ISBN 3-929757-63-X.
- MAFO-03** AL-HAMID, M.: *Extraktion von höheren Moden in TEM-Wellenleitern*, 2004. ISBN 3-929757-64-8.
- MAFO-04** HAASE, H., J. NITSCH, and T. STEINMETZ: *Transmission-Line Super Theory – A new Approach to an Effective Calculation of Electromagnetic Interference*, 2004. ISBN 3-929757-67-2.
- MAFO-05** BACHRY, A.: *Power Quality Studies in Distribution Systems Involving Spectral Decomposition*, 2004. ISBN 3-929757-68-0.
- MAFO-06** STYCZYNSKI, Z. A.: *Power Network and Renewables – A Scientific Report*, 2004. ISBN 3-929757-69-9.
- MAFO-07** BLUME, E.: *Numerische Analyse der Kopplung linearer Antennen innerhalb eines Resonators*, 2004. ISBN 3-929757-71-0.
- MAFO-08** HANDSCHIN, E. and Z. A. STYCZYNSKI: *Power System Application of the Modern Battery Storage*, 2004. ISBN 3-929757-75-3.
- MAFO-09** HAASE, H.: *Full-Wave Field Interactions of Nonuniform Transmission Lines*, 2005. ISBN 3-929757-78-8.
- MAFO-10** NITSCH, D.: *Die Wirkung eingekoppelter ultrabreitbandiger elektromagnetischer Impulse auf komplexe elektronische Systeme*, 2005. ISBN 3-929757-79-6.
- MAFO-11** HADZI-KOSTOVA, B.: *Protection Concepts in Distribution Networks with Decentralized Energy Resources*, 2005. ISBN 3-929757-84-2.
- MAFO-12** STEINMETZ, T.: *Ungleichförmige und zufällig geführte Mehrfachleitungen in komplexen technischen Systemen*, 2006. Nummerierung geändert, ISBN 3-929757-98-2.
- MAFO-13** STYCZYNSKI, Z. and J. HAUBROCK: *Influence of Distributed and Renewable Generation on Power System Security – Proceedings of the CRIS Workshop 2006*, 2006. ISBN 3-929757-99-0.
- MAFO-14** HEIDECK, G.: *Ein autonomes Brennstoffzellensystem: Optimierungsansätze*, 2006. ISBN 3-929757-94-X.
- MAFO-15** STYCZYNSKI, Z. und H.-D. MUSIKOWSKI: *Dresdener Kreis Elektroenergieversorgung 7*, 2006. ISBN 3-929757-85-0.
- MAFO-16** GRONWALD, F.: *Antenna Theory in Resonating Systems derived from Fundamental Electromagnetism*, 2007. ISBN 3-929757-93-1.
- MAFO-17** KRAUTHÄUSER, H.G.: *Grundlagen und Anwendungen von Modenverwirbelungskammern*, 2007. ISBN 978-3-929757-43-9.
- MAFO-18** DZIENIS, C.: *Ersatzmodelle nichtlinearer Lasten in elektrischen Verteilungsnetzen*, 2007. ISBN 978-3-929757-07-1.

- MAFO-19** STYCZYNSKI, Z. and J. HAUBROCK: *Renewable and Dispersed Power Generation in Power Systems*, 2007. ISBN 978-3-929757-44-6.
- MAFO-20** HAUBROCK, J.: *Parametrierung elektrischer Äquivalentschaltbilder von PEM-Brennstoffzellen*, 2008. ISBN 978-3-940961-02-0.
- MAFO-21** ANGELOV, A. N.: *Rechnergestütztes Lernen im Bereich der Regenerativen Energien (Ausgewählte Aspekte)*, 2008. ISBN 978-3-940961-03-7.
- MAFO-22** KOMARNICKI, P.: *Anwendung hochgenauer, synchroner Messungen zur Verbesserung des Betriebs von Verteilungsnetzen*, 2008. ISBN 978-3-940961-04-4.
- MAFO-23** ROGGATZ, C.: *Trainingssimulator für die Führung von elektrischen Systemen mit dezentralen Energieeinspeisungen – Trainingsszenarien und Umsetzung*, 2008. ISBN 978-3-940961-05-1.
- MAFO-24** RUDION, K.: *Aggregated Modelling of Wind Farms*, 2008. ISBN 978-3-940961-14-3.
- MAFO-25** GANJAVI, M. R.: *Protection System Coordination Using Expert System*, 2008. ISBN 978-3-940961-15-0.
- MAFO-26** BOFINGER, S.: *Energieversorgungsnetze mit einem hohen Anteil an photovoltaischer Solarenergie: Standortbestimmung, Solarstromprognose, Netzintegration*, 2008. ISBN 978-3-940961-25-9.
- MAFO-27** STYCZYNSKI, Z. and P. KOMARNICKI: *Distributed and Renewable Power Generation*, 2008. ISBN 978-3-940961-26-6.
- MAFO-28** KOCHETOV, S. V.: *Time- and Frequency-Domain Modeling of Passive Interconnection Structures in Field and Circuit Analysis*, 2008. ISBN 978-3-940961-27-3.
- MAFO-29** MAGDOWSKI, M.: *Entwicklung und Validierung eines Werkzeugs zur Berechnung der elektromagnetischen Einkopplung von stochastischen Feldern in Leitungsstrukturen*, 2008. ISBN 978-3-940961-28-0.
- MAFO-30** SONNEMANN, F.: *Elektromagnetische Effekte an elektrischen Zündmitteln (EED) mit angeschlossener Zündkreiselektronik (ZKE) bei impulsförmiger, breitbandiger Bestrahlung*, 2009. ISBN 978-3-940961-32-7.
- MAFO-31** SMIEJA, T.: *Multikriterielle Planung interregionaler Elektrizitätsnetze im liberalisierten Energiemarkt*, 2009. ISBN 978-3-940961-35-8.
- MAFO-32** HEYDE, C. O.: *Dynamic Voltage Security Assessment for On-Line Control Room Application*, 2010. ISBN 978-3-940961-40-2.
- MAFO-33** STYCZYNSKI, Z. A. and N. I. VOROPAI (EDITORS): *Renewable Energy Systems Fundamentals, Technologies, Techniques and Economics*, 2010. ISBN 978-3-940961-42-6.
- MAFO-34** Styczynski, Z. A. и N. I. Voropai (Editors): *Renewable Energy Systems Fundamentals, Technologies, Techniques and Economics (Russian Version)*, 2010. ISBN 978-3-940961-44-0.
- MAFO-35** STYCZYNSKI, Z. A. and A. LINDEMANN (EDITORS): *Integration of Renewable Energies into the Grid / Proceedings of the Power & Energy Student Summit 2010*, 2010. ISBN 978-3-940961-47-1.
- MAFO-36** STYCZYNSKI, Z. A. und H.-D. MUSIKOWSKI (EDITORS): *Dresdener Kreis Energieversorgung 11*, 2010. ISBN 978-3-940961-51-8.
- MAFO-37** GURBIEL, M. A.: *Definition and Testing of a Digital Interface of a Power Substation*, 2011. ISBN 978-3-940961-54-9.
- MAFO-38** LOMBARDI, P.: *Multi Criteria Optimization of an Autonomous Virtual Power Plant*, 2011. ISBN 978-3-940961-55-6.

- MAFO-39** POWALCO, M.: *Beobachtbarkeit eines elektrischen Verteilungsnetzes – Ein Beitrag zum Smart Grid*, 2011. ISBN 978-3-940961-62-4.
- MAFO-40** STYCZYNSKI, Z. A., K. RUDION, and C. NGUYEN-MAU (EDITORIAL BOARD): *Power System Dynamic Security Assessment*, 2011. ISBN 978-3-940961-61-7.
- MAFO-41** KÄBISCH, M.: *Optimale Dimensionierung und Betriebsführung einer brennstoffzellenbasierten Auxiliary Power Unit im Fahrzeug*, 2011. ISBN 978-3-940961-67-9.
- MAFO-42** STYCZYNSKI, Z. A. und N. I. VOROPAI (EDITORS): *Special Issue Grant 220 Russian Federation SSmart Grid for Efficient Energy Power System for the Future”, Proceedings Volume I*, 2012. ISBN 978-3-940961-74-7.
- MAFO-43** STYCZYNSKI, Z. A., P. KOMARNICKI und A. NAUMANN (EDITORS): *Abschlussbericht Harz.ErneuerbareEnergien-mobility*, 2012. ISBN 978-3-940961-71-6.
- MAFO-44** HEUER, M.: *Diagnosetool für stationär betriebene PEM-Brennstoffzellensysteme*, 2012. ISBN 978-3-940961-77-8.
- MAFO-45** STÖTZER, M.: *Demand Side Integration in elektrischen Verteilnetzen – Potenzialanalyse und Bewertung*, 2012. ISBN 978-3-940961-78-5.
- MAFO-46** MAGDOWSKI, M.: *Vergleich der Einkopplung deterministischer und statistischer elektromagnetischer Felder in Leitungen*, 2012. ISBN 978-3-940961-75-4.
- MAFO-47** NAUMANN, A.: *Leitwarte im Smart Grid*, 2012. ISBN 978-3-940961-81-5.
- MAFO-48** RUDION, K.: *Offshore Power System Planning – Selected Aspects*, 2012. ISBN 978-3-940961-82-2.
- MAFO-49** NGUYEN-MAU, C.: *Electric Power System Stability Enhancement by Voltage Source Converter based High Voltage Direct Current Technology*, 2012. ISBN 978-3-940961-84-6.
- MAFO-50** GUO, H.: *Measurement-Based Load Modeling for Smart Grid Planning*, 2012. ISBN 978-3-940961-86-0.
- MAFO-51** STYCZYNSKI, Z. A.: *Proceedings No. 2 in the Scope of Mega Grant Baikal*, 2013. ISBN 978-3-940961-95-2.
- MAFO-52** STYCZYNSKI, Z. A.: *Proceedings No. 3 in the Scope of Mega Grant Baikal*, 2013. ISBN 978-3-940961-98-3.
- MAFO-53** WENGE, C.: *Optimaler Betrieb von mobilen Speichern im Smart Grid. -Mobilitätsleitwarte-*, 2013. ISBN 978-3-944722-01-6.
- MAFO-54** RÖHRIG, C.: *Smart Distribution Planung unter Berücksichtigung von residualen Lasten*, 2014. ISBN 978-3-944722-06-1.
- MAFO-55** MIDDELSTÄDT, F.: *Research of SEM Poles of Complex Wire Structures*, 2014. ISBN 978-3-944722-07-8.
- MAFO-56** STYCZYNSKI, Z. A. (EDITOR): *Power Network and Renewables – A Scientific Report – 15 Years Research*, 2014. ISBN 978-3-944722-08-5.
- MAFO-57** SOLONINA, N. N., V. S. STEPANOV, and K. V. SUSLOV: *Information technology in intelligent power networks*, 2014. ISBN 978-3-944722-13-9.
- MAFO-58** KREBS, R.: *Fundamentals of Power System Protection*, 2014. ISBN 978-3-944722-15-3.
- MAFO-59** MOSKALENKO, N.: *Optimal Dynamic Energy Management System in Smart Homes*, 2014. ISBN 978-3-944722-16-0.
- MAFO-60** HAUER, I.: *Optimale Last- und Erzeugungsanpassung bei kritischen Netzzuständen – Algorithmen und deren Bewertung*, 2014. ISBN 978-3-944722-18-4.

- MAFO-61** RICHTER, M.: *Dresdner Kreis Elektroenergieversorgung 15, Begleitband zum Workshop 2014*, 2014. ISBN 978-3-944722-21-4.
- MAFO-62** STYCZYNSKI, Z. A., A. RICHTER und P. KÜHNE: *Second ELECON Workshop – Begleitband zum Workshop 2014*, 2014. ISBN 978-3-944722-23-8.
- MAFO-63** BERNSTEIN, P.: *Modellgestützte optimale Betriebsführung von PEM-Brennstoffzellen für autonome Anlagen*, 2015. ISBN 978-3-944722-24-5.
- MAFO-64** RABE, S.: *Betrieb einer Zweipunkt-Offshore-HGÜ-Verbindung – Modelluntersuchungen*, 2015. ISBN 978-3-944722-31-3.
- MAFO-65** ARENDARSKI, B.: *Reliability Assessment of Smart Grids*, 2015. ISBN 978-3-944722-32-0.
- MAFO-66** PAN, X.: *Numerisches EMV-Simulationsverfahren zur Berechnung der Störaussendung elektrischer Antriebssysteme in Hybridfahrzeugen*, 2016. ISBN 978-3-944722-34-4.
- MAFO-67** RICHTER, M.: *PMU-basierte Zustandsabschätzung in Smart Distribution*, 2016. ISBN 978-3-944722-43-6.
- MAFO-68** BIELCHEV, I.: *Adaptiver Distanzschutz im Standard IEC 61850*, 2016. ISBN 978-3-944722-45-0.
- MAFO-69** HASSAN, A.: *Modeling of Single and Double-Shielded Cables for EMC Applications*, 2016. ISBN 978-3-944722-41-2.
- MAFO-70** LIU, X.: *Control of Voltage Source Converter Based High Voltage Direct Current Transmission Systems for Grid Code Compliance*, 2016. ISBN 978-3-944722-46-7.
- MAFO-71** KAISER, M.: *Fusion of Interventional Ultrasound & X-ray*, 2016. ISBN 978-3-944722-51-1.
-

